DISSERTATION

IMPROVEMENTS IN GRACE-BASED TERRESTRIAL WATER STORAGE ANOMALIES FOR GROUNDWATER DEPLETION AND ECOHYDROLOGICAL ANALYSES

Submitted by

Muhammad Ukasha

Department of Civil and Environmental Engineering

In partial fulfillment of the requirements

For the Degree of Doctor of Philosophy

Colorado State University

Fort Collins, Colorado

Fall 2022

Doctoral Committee:

Advisor: Jeffrey D. Niemann

Neil S. Grigg
Ryan T. Bailey
Michael J. Ronayne

Copyright by Muhammad Ukasha 2022

All Rights Reserved

ABSTRACT

IMPROVEMENTS IN GRACE-BASED TERRESTRIAL WATER STORAGE ANOMALIES FOR GROUNDWATER DEPLETION AND ECOHYDROLOGICAL ANALYSES

Groundwater is a major source of freshwater globally and an important component of terrestrial ecosystems. In many regions, groundwater is being rapidly depleted, and its effective management requires improved monitoring across large regions. Terrestrial water storage anomalies (TWSA) from the Gravity Recovery And Climate Experiments (GRACE) satellite mission and the GRACE follow-on mission have been extensively used in hydrological studies related to groundwater depletion and ecohydrology at large scales. However, GRACE observations include significant errors, so pre-processing is normally required before the data can be used. In particular, the TWSA are usually filtered to reduce the effects of measurement errors and then rescaled to reduce the unintended impacts of the filtering. In addition, the coarse spatial resolution of TWSA (0.25^{o}), limits its ability to observe small-scale spatial variations. The objectives of the dissertation are to improve the rescaling of GRACE observations for groundwater depletion estimates, develop a spatial downscaling method for GRACE observations, and examine the ecohydrological implications of a large-scale drought using GRACE observations.

The rescaling is typically performed to maximize the Nash-Sutcliffe Efficiency (NSE) between the filtered TWSA and TWSA from large-scale hydrologic models that represent an

incomplete water budget. This study (1) evaluates the use of NSE in the current GRACE rescaling methodology, (2) develops an improved methodology that incorporates a complete regional water budget, and (3) examines the impacts of the rescaling methodology on regional assessments of groundwater depletion. To evaluate the use of NSE as a performance metric, the existing rescaling method is compared to an analytical solution that restores the relative variability between the rescaled filtered and original GRACE TWSA series. The relative variability approach produces more reliable estimates when comparing to TWSA estimates from global positioning systems (GPS) for the study region (the Sacramento and San Joaquin River basins in California). Rescaling with the complete regional water budget results in a larger scale factor than the scale factor from the large-scale hydrologic model outputs, and the new TWSA results are more consistent with those from GPS. The larger scale factor also suggests that regional groundwater depletion is more severe in the study region than previously estimated. This result is important for regional water management organizations to study the impacts of drought and effectiveness of any policy and management decisions.

Due to their coarse resolution, GRACE TWSA does not capture fine scale spatial variations in TWSA, and GRACE TWSA can miss the extreme TWSA values that occur in a region. Several procedures have been previously proposed to downscale coarse TWSA from GRACE. These procedures rely on information for other hydroclimatic variables or the output of hydrological models, and they seek to improve the local estimates of TWSA. However, they may not reproduce the statistical properties of fine resolution TWSA patterns. This dissertation aims to develop a stochastic downscaling method that relies only on TWSA data and reproduces the statistical properties of fine resolution (0.0625^{o}) TWSA patterns. It is hypothesized that TWSA

are scale invariant, which allows the statistical properties of fine scale variations to be inferred from those of coarse scale variations. Three study regions are considered including the Central Amazon in Brazil, the Sindh province in Pakistan, and a region around California, U.S.A. For each region, the relationships between the TWSA moments and the spatial resolution is examined for resolutions between 0.25^o and 4^o. These relationships are used to determine the scaling exponent for each moment. Nonlinear relationships between scaling exponents and the moment orders indicate that multifractality occurs for the three regions. The degree of multifractality differs between the three regions and between wet and dry conditions. Based on these results, a multiplicative random cascade model is developed to downscale the TWSA. The model requires two parameters: the TWSA value at 0.25^o resolution within the region and a parameter that is related to the spatial variance. Large numbers of realizations are produced from the stochastic downscaling method. The multifractal curves of the observed TWSA occur within the scatter of curves obtained from realizations. This suggests that the model approximately reproduces the observed scale invariance in the TWSA. When the model is used to downscale to the ultimate resolution (0.0625^o), it produces much larger maximum TWSA values than the coarse resolution input.

Satellite based vegetation indices are increasingly used to characterize vegetation's response to climate variability and change over large spatial extents. The use of a given index assumes that the index adequately describes the vegetation's response to hydroclimatic forcing. This part of the dissertation aims to compare the temporal behaviors of normalized difference vegetation index (NDVI) and leaf area index (LAI) and their associations with hydroclimatic variables. Observations of monthly precipitation, streamflow, temperature, vapor

pressure deficit, evapotranspiration, and TWSA from GRACE are processed for the combined Sacramento River and San Joaquin River basins in California for 13 water years (October 2002 to September 2015). Estimates of NDVI and LAI are obtained for the same period from MODerate resolution Imaging Spectroradiometer (MODIS). The seasonal cycle of NDVI peaks 2–3 months earlier than LAI. The seasonal variation in NDVI follows the seasonality of TWSA (i.e., water availability) whereas the seasonal cycle of LAI follows the seasonality in mean temperature and vapor pressure deficit (i.e., atmospheric water demand). Cross-correlation analyses of NDVI and LAI with the hydroclimatic variables show that LAI is more strongly correlated with most of the hydroclimatic variables considered.

ACKNOWELDGEMENTS

First of all, thanks to Allah Almighty for giving me the strength, ability, and knowledge to complete this research. Foremost, I would like to express my sincere gratitude to my advisor Dr. Jeffrey D. Niemann for the continuous support, patience, motivation, enthusiasm, immense knowledge, and guidance in my Ph. D research and writing. I will forever be thankful to my former advisor Dr. Jorge A. Ramirez (late). This dissertation would not have been possible without his assistance. I would like to thank the rest of my doctoral committee: Dr. Neil S. Grigg, Dr. Ryan T. Bailey and Dr. Michael Ronayne for their invaluable discussion, insightful comments, and feedback. I would take this opportunity to also acknowledge my sponsor. This work was supported by a grant provided by Bureau of Educational and Cultural Affairs, US Department of State under the umbrella of foreign Fulbright scholarship program. Deep gratitude to all my family members for the continuous encouragement and support. I am always indebted to my parents, wife, and kids for their unparalleled love and countless sacrifices throughout this journey as well as the inspiration to follow my dreams. Last but not least, I express my deepest gratitude to my friends and colleagues at Colorado State University for their friendship.

TABLE OF CONTENTS

Chapter 1 Introduction

1.1 Motivation

Approximately 70% of the Earth's surface is covered by water, but more than 97% of that water is contained in the oceans and other saline water bodies (Figure 1.1). Groundwater makes up a significant fraction (99%) of the readily available freshwater (*Cherry,* 2022). Due to its high abundance and low variability in space and time as compared to surface sources of fresh water, groundwater has been a major source for domestic and agricultural water especially in dry regions (*Rodell et al.,* 2009). Around 50% of the world's population depends completely or partially on groundwater as a primary source for drinking water, and nearly 70% of global food production relies on groundwater (*Cherry,* 2022). Groundwater is pivotal in sustaining ecosystems in semi-arid and arid regions and makes up 50% of the global river flows (*Cherry,* 2022), and groundwater is especially important to sustaining food production and economic security during droughts (e.g., *Kaur et al.,* 2022).

Increasing pressure is being placed on water resources by climate change, population growth, and economic development (*Livingston & Garrido,* 2004; *Famiglietti et al.,* 2011). These pressures along with pollution and mismanagement of surface waters has resulted in overreliance on groundwater (*Rodell et al.,* 2009). *Shah et al.* (2000) and *Konikow and Kendy* (2005) reported total global groundwater withdrawal rates of 750-800 km^3/year. Long-term groundwater abstraction from aquifers at rates much higher than recharge rates results in groundwater depletion (*Gleeson et al., 2010*). *Wada et al.* (2010) indicated a significant increase in the magnitude of groundwater depletion from 126 (+/- 32) km^3/year in 1960 to 283

(+/- 40) km^3/year in 2000. Although economic gains from groundwater use have been dramatic, groundwater resources in some regions have been depleted to the extent that well yields have decreased, pumping costs have risen, water quality has deteriorated, aquatic ecosystems have been damaged, and/or land has irreversibly subsided (*Konikow and Kendy*, 2005).

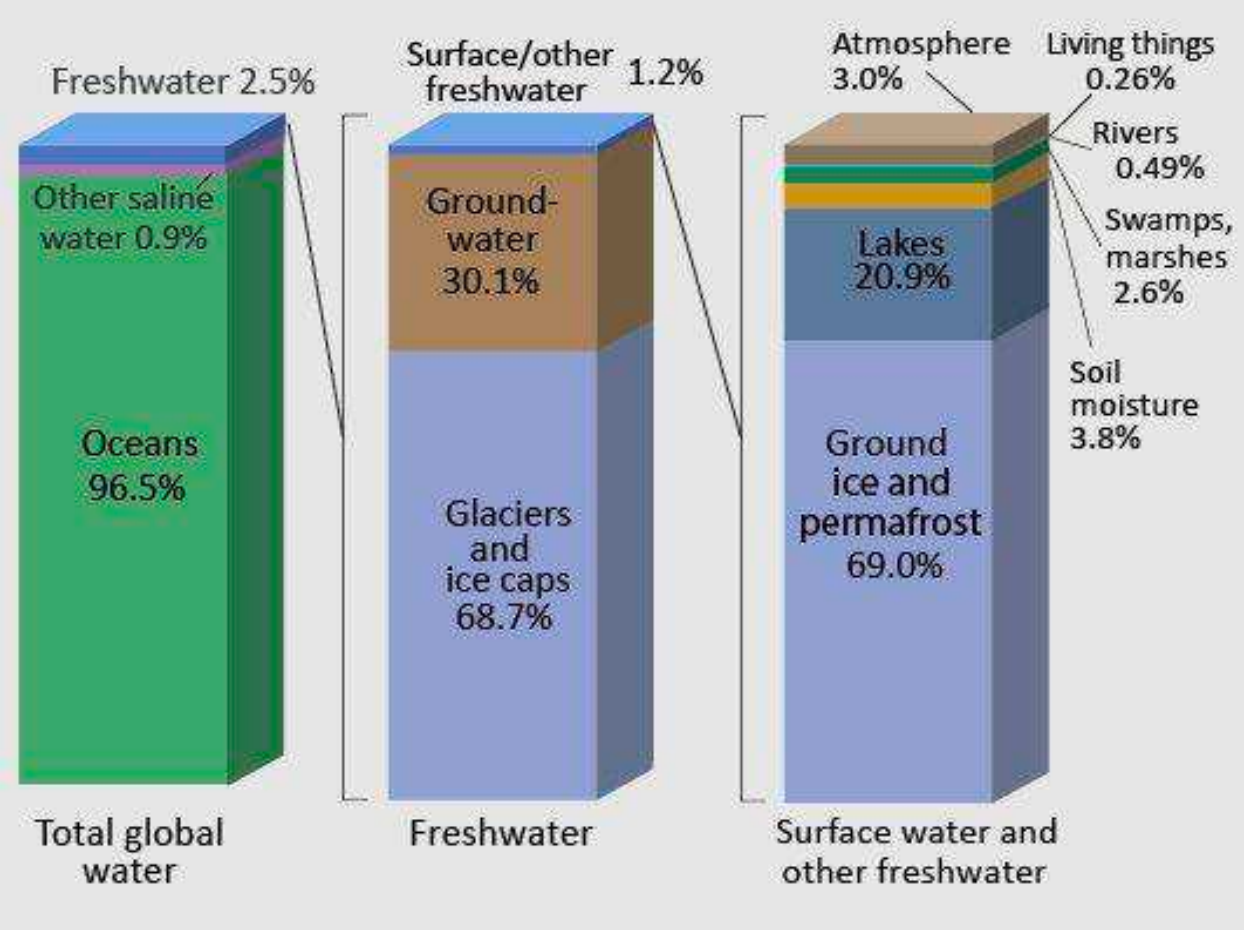

Figure 1.1. Distribution of earth's water (Adapted from Igor Shiklomanov's chapter "World's freshwater resources" in *Peter H. Gleick (editor)*, 1993, Water in Crisis: A Guide to the World's Freshwater Resources)

Given the groundwater's importance, there is an essential need to observe groundwater systems and their interactions with the climatic, hydrologic, ecosystem, and socio-economic processes that influence groundwater dynamics. However, groundwater is often poorly

monitored, which hinders estimation of groundwater depletion rates and sustainable groundwater management. Around the world, water withdrawals from pumping wells are usually unrestricted and unmonitored, which further complicates the problem (*Famiglietti et al.,* 2011). Moreover, groundwater monitoring stations are sparsely located, so spatial interpolation is often required to obtain water table estimates. Simple interpolation can yield unrealistic values due to the spatial variability of aquifer properties and aquifer response. Groundwater models can also be used to study variations in groundwater storage. However, such models require knowledge of the different components of the water balance, which requires hydro-meteorological forcing at high spatial resolutions.

The Gravity Recovery and Climate Experiments (GRACE) and the GRACE follow-on satellite missions provide monthly estimates of terrestrial water storage anomalies (TWSA), which are deviations from the long term mean terrestrial water storage (*Yeh et al.,* 2006; *Brunner et al.,* 2006; *Strassberg et al.,* 2007; *Owor,* 2010; *Castle et al.,* 2014). Terrestrial water storage refers to all the snow, ice, surface water, soil water, rock moisture, water in biomass, and groundwater per unit area of land. The TWSA are estimated by mapping the time variable gravity field (*Tapley et al.,* 2004) at a spatial scale no smaller than 4^{o} (*Rodell et al.,* 2009). The gravitational field is mapped by making accurate measurements of the change in distance between two identical satellites flying at a separation distance of about 220 km at an altitude of 450 km above the Earth's surface (*Scanlon et al.,* 2012). GRACE-observed TWSA can be combined with auxiliary hydrological datasets to provide estimates of groundwater storage anomalies (e.g., *Xiong et al.,* 2022; *Zaitchik et al.,* 2008). Several studies such as *Yeh et al.* (2006), *Rodell et al.* (2009), and *Famiglietti et al.* (2011) have demonstrated the potential of

GRACE data to estimate the groundwater storage changes on a regional scale with sufficient accuracy to benefit water management. *Yeh et al.* (2006) used *in–situ* measurements of soil moisture to extract groundwater storage anomalies from GRACE and used *in-situ* groundwater level data to validate the anomalies for the state of Illinois. Similarly, other studies such as *Rodell et al.* (2007 & 2009) and *Famiglietti et al.* (2011) obtained auxiliary data from hydrological or land surface models to remove contributions from other natural reservoirs of water from GRACE TWSA.

GRACE gravity signals require pre-processing to reduce errors, but the TWSA suffer losses in variability during the pre-processing. TWSA from global hydrologic models are used to recapture the lost variability in GRACE TWSA. This process is known as rescaling of GRACE TWSA (e.g., *Landerer and Swenson,* 2012). The accuracy of the rescaled GRACE TWSA depends upon the rescaling algorithm and TWSA from the hydrologic model (*Chen et al.,* 2017). The global hydrologic models do not simulate groundwater, rock moisture, and surface water storage (*Pun et al.,* 2022), so they do not characterize the complete water budget. Therefore, rescaling GRACE TWSA based on such hydrologic models might result in substantial errors.

The coarse spatial resolution of GRACE limits the applicability of the TWSA to large regions (~ 160,000 km^2). Studies have implemented procedures to downscale GRACE TWSA or derived the groundwater storage anomalies. For example, *Sun* (2013) predicted the groundwater level at the scale of pumping wells using an artificial neural network that combines GRACE TWSA, well observations, and climate data such as precipitation and temperature. Other machine learning algorithms have been recently used to downscale GRACE TWSA (e.g., *Yin et al.,* 2022). However, these methods are data intensive and require

hydroclimatic and water storage information at fine resolutions. Furthermore, these methods focus on estimating local TWSA with little emphasis on reproducing statistical properties of TWSA at the fine resolution, so they may over or underestimate the portion of the region experiencing extreme TWSA values. Thus, there is a need to estimate fine resolution TWSA in a way that reproduces the statistical characteristics while using few data.

1.2 Research objectives

The overarching objective of this dissertation is to improve GRACE TWSA for estimation of groundwater depletion and related ecohydrological responses to hydroclimatic variability. To this end, the dissertation has the following specific goals:

i. Development of an improved GRACE rescaling algorithm that uses the complete budget
ii. Development of a stochastic downscaling model that uses only TWSA information
iii. Application of GRACE TWSA for ecohydrological analysis for climate-water-vegetation interactions.

1.3 Organization of the dissertation

Chapter 2 describes the development, application, and evaluation of an improved algorithm to rescale GRACE TWSA. The chapter also documents the impacts of rescaling on estimates of regional groundwater depletion. Chapter 3 deals with the identification of scale-invariant behavior and stochastic downscaling of GRACE TWSA. Chapter 4 describes the agroecohydrology of a large and diverse region. In particular, it documents the temporal variations of two widely used satellite-based vegetation indices and their interactions with hydroclimatology and TWSA. Finally, Chapter 5 concludes by summarizing the key findings of the dissertation and potential avenues for future research.

Chapter 2 An Improved Rescaling Algorithm for Estimating Groundwater Depletion Rates using the GRACE Satellite

2.1 Introduction

Monitoring and understanding groundwater storage at regional scales (such as aquifers and river basins larger than 10 km^2 in area; *Kimura et al.,* 2009) is an important aspect of integrated water resources management. Groundwater provides domestic and agricultural water to more than 2 billion people globally (*Alley et al.,* 2002; *Nair and Indu*, 2020; *Ouma et al.,* 2015; *Seo and Lee*, 2016) and is particularly important in dry regions (*Wada et al.,* 2010). Groundwater also provides critical ecosystem services such as regulating floods and droughts (*Griebler and Maria*, 2014) and sustaining rivers and wetlands during the dry season (*Miguez-Macho and Fan*, 2012).

Population and economic growth, as well as mismanagement and pollution of surface water resources, has resulted in increased reliance on groundwater (*Rodell et al.,* 2009). However, the long-term abstraction of groundwater at rates much higher than recharge rates is causing groundwater depletion and mining in many regions (*Gleeson et al.,* 2010; *Russo et al.,* 2014). A comprehensive review of groundwater withdrawal and depletion studies by *Bierkens and Wada* (2019) reports a significant increase in global groundwater depletion from 64 (±16) km^3/year in 1960 to 304 km^3/year in 2010. Given the importance of groundwater in meeting water requirements and sustaining ecosystems, it is necessary to monitor regional groundwater storage and its interaction with climatic, hydrologic, ecosystem, and socio-economic processes.

The GRACE (Gravity Recovery And Climate Experiments) satellite remote sensing mission (*Deng et al.,* 2019) provides estimates of monthly terrestrial water storage anomalies (TWSA),

which are the deviations from the long-term mean water storage (*Gao et al.,* 2010; *Yang et al.,* 2018). The TWSA are obtained by mapping the time variable gravity field (*Krogh et al.,* 2010; *Tapley et al.,* 2004) at a spatial scale no smaller than 400 km or approximately 4° (*Rodell et al.,* 2009). The TWSA represent the combined change in the snow water equivalent (SWE), ice, surface water storage, soil moisture storage, rock moisture, and groundwater storage per unit area of land. GRACE-based TWSA estimates have been combined with auxiliary hydrological datasets to provide estimates of groundwater storage variations in the Central Valley of California (e.g., *Famiglietti et al.,* 2011; *Scanlon et al.,* 2012a), Illinois (*Yeh et al.,* 2006), Northwest India (*Rodell et al.,* 2009), and several other regions across the globe (e.g., *Ouma et al.,* 2015; *Seo and Lee*, 2016).

GRACE TWSA are estimated from spherical harmonics or mass concentration blocks (*Save et al.,* 2016). GRACE TWSA based on spherical harmonics have been shown to have less uncertainty than GRACE TWSA estimated from mass concentration blocks (*Ali et al.,* 2022). Before they are available to the general scientific community, the TWSA values based on spherical harmonic coefficients are filtered to minimize measurement errors and noise (*Scanlon et al.,* 2016). However, filtering GRACE observations also results in partial removal of the true geophysical signal and a reduction of the spatial signal (*Pun et al.,* 2022; *Swenson and Wahr* 2011). Therefore, scale factors based on large-scale hydrological models (i.e., having spatial resolution around 1°) are used to rescale the filtered TWSA values and restore some of the lost variability (*Landerer and Swenson* 2012). In particular, the rescaling factor is selected to maximize the Nash-Sutcliffe Efficiency (NSE; *Nash and Sutcliffe* 1970) between the model's rescaled filtered TWSA and original TWSA (*Landerer and Swenson* 2012). Then, the selected

scale factor is applied to the GRACE TWSA. The accuracy of the restored GRACE signal depends on the accuracy of the scale factor (*Chen et al.,* 2017). Large-scale hydrologic models typically simulate soil moisture and snow water. Surface water storage, rock moisture, and groundwater are not represented (*Pun et al.,* 2022), so a complete water budget is not used. Thus, the TWSA signal from the large-scale hydrologic model is likely smaller than the real TWSA signal (*Pun et al.,* 2022; *Yi, Wang, and Sun* 2016). In regions where groundwater is the dominant component of TWSA and/or in areas that are heavily managed, the scale factors based on large-scale hydrologic models might include substantial errors (*Longuevergne et al.,* 2010; *Scanlon et al.,* 2012a). Alternative scaling methods have also been proposed. *Velicogna and Wahr* (2006) and *Famiglietti et al.,* (2011) estimated the scale factor by spatially filtering 1-cm of water depth uniformly placed on their study regions. Scale factor was estimated by taking the ratio of 1 cm to the average of the filtered depths. *Scanlon et al.,* (2012a) rescaled groundwater storage anomalies from GRACE using well observations.

The process of rescaling GRACE observations is meant to restore the variability in the TWSA. *Gupta et al.,* (2009) showed that the process of NSE maximization in general aims to capture the correlation and relative variability (i.e., the ratio of the model and observed standard deviations) with little emphasis on minimizing bias between two time series. Thus, the variability introduced by NSE maximization is controlled by the correlation between the two-time series. Unless the filtered and original time series have a perfect correlation, the scale factor based on maximization of NSE can underestimate the variability.

The objectives of this study are to (1) evaluate the use of NSE in the current GRACE rescaling methodology, (2) test a new rescaling methodology that incorporates a complete

regional water budget, and (3) examine the impacts of the rescaling methodology on a regional assessment of groundwater depletion. For objective 1, an analytical solution of NSE maximization is formulated and the results of that approach are compared to a method that reproduces the full variability during the GRACE rescaling. For objective 2, the complete water budget is included by selecting the scale factor so that the GRACE TWSA have the same variance as TWSA estimated from regional precipitation, evapotranspiration, and streamflow data. The results from both experiments (i.e., objectives 1 and 2) are evaluated by comparing to TWSA from Global Positioning Systems (GPS) for the combined Sacramento and San Joaquin River basins in California. Finally, for objective 3, new groundwater depletion estimates are derived from GRACE for the study region using the new rescaling method along with surface water storage observations and soil moisture and SWE from global hydrologic models. The resulting estimates are compared to prior estimates of groundwater depletion for the study region.

2.2 Materials and Methods

2.2.1 Methods

Evaluation of use of NSE in the current rescaling method

Landerer and Swenson (2012) estimated the scale factor using a TWSA time series derived from the Noah land surface model within the Global Land Data Assimilation System (GLDAS-Noah; *Rodell et al.,* 2004). GLDAS-Noah TWSA time series does not represent complete budget because it does not explicitly model surface water, groundwater, and rock moisture. The method does not use GRACE TWSA, and implicitly assumes that the GLDAS-Noah-based scale factors also apply to GRACE. First, they filtered the GLDAS-Noah TWSA using the filter from the

GRACE processing. This filtering produces a time series with a non-zero mean. Then, they selected the scale factor k to minimize the sum of the squared errors E_{SSE}, which is calculated:

$$E_{SSE} = \sum_{i=1}^{n} \left(S_{O,GLDAS,i} - kS_{F,GLDAS,i} \right)^2 \quad (2.1)$$

where $S_{O,GLDAS}$ is the original unfiltered GLDAS-Noah TWSA time series, $S_{F,GLDAS}$ is the filtered GLDAS-Noah TWSA time series, i is the month, and *n* is the number of months considered. This minimization is equivalent to the maximization of NSE E_{NSE}, which can be calculated as (*Nash & Sutcliffe,* 1970):

$$E_{NSE} = 1 - \frac{\sum_{i=1}^{n} \left(S_{O,GLDAS,i} - kS_{F,GLDAS,i} \right)^2}{\sum_{i=1}^{n} \left(S_{O,GLDAS,i} - \mu_{S_{O,GLDAS}} \right)^2} \quad (2.2)$$

where $\mu_{S_{O,GLDAS}}$ is the mean of the original unfiltered GLDAS-Noah TWSA time series, which is zero. The filtered GRACE TWSA are then rescaled by multiplying the scale factors from Equation 2.2 with the filtered GRACE TWSA time series.

NSE can also be written in terms of the bias, error in standard deviation, and correlation with the original unfiltered TWSA time series (*Gupta et al.,* 2009). Specifically:

$$E_{NSE} = 2\alpha r - \alpha^2 - \beta^2 \quad (2.3)$$

where r is the Pearson correlation coefficient between the two-time series. The variable α is the relative variability, which is the ratio of the standard deviations of the two-time series $(\sigma_{kS_{F,GLDAS}} / \sigma_{S_{O,GLDAS}})$. The variable $\sigma_{kS_{F,GLDAS}}$ is the standard deviation of the rescaled filtered

GLDAS-NAOH TWSA time-series, and $\sigma_{S_{O,GLDAS}}$ is the standard deviation of the original unfiltered GRACE-Noah TWSA time series. The variable β is the normalized bias, which is the difference in the means of two time series divided by the standard deviation of original unfiltered TWSA time series $((\mu_{kS_{F,GLDAS}} - \mu_{S_{O,GLDAS}}) / \sigma_{S_{O,GLDAS}})$. The variable $\mu_{kS_{F,GLDAS}}$ is the mean of rescaled filtered GLDAS-Noah TWSA time-series, which is typically nonzero. The ideal values for the Pearson correlation coefficient and relative variability are both one, whereas the ideal value for the normalized bias is zero (*Gupta et al.,* 2009). *Landerer and Swenson* (2012) rescaled the filtered GRACE TWSA $(S_{F,GRACE})$ by multiplying it with the GLDAS-Noah-based scale factor obtained from maximization of NSE. Because the mean of the filtered GRACE TWSA is not typically zero, the mean of the rescaled filtered GRACE TWSA increases to scale factor times the mean of the filtered GRACE TWSA. That magnification of the mean may introduce bias.

The maximization of NSE is aims to make the first term is as large as possible while keeping the other two terms as small as possible. It can be shown that the correlation between the two-time series does not change with rescaling. Therefore, the maximization of the first term depends on maximizing α. However, any increase in α is penalized due to the associated increase in the magnitude of the negative second term. By taking the first derivate of NSE (Equation 2.3) with respect to the α, *Gupta et al.* (2009) showed that the maximization of NSE occurs when $\alpha = r$. This result indicates that the variability of the rescaled time series is a function of the correlation between filtered and unfiltered time series.

An analytical solution for scale factor k can be obtained as follows. By definition:

$$\alpha = \frac{\sigma_{kS_{F,GLDAS}}}{\sigma_{S_{O,GLDAS}}} \tag{2.4}$$

The variable $\sigma_{kS_{F,GLDAS}}$ can be written as:

$$\sigma_{kS_{F,GLDAS}} = \left(\frac{1}{n-1} \sum_{i=1}^{n} \left(kS_{F,GLDAS,i} - \mu_{kS_{F,GLDAS}} \right)^2 \right)^{0.5} \quad (2.5)$$

If the mean is removed from the filtered TWSA time series, $\mu_{kS_{F,GLDAS}}$ becomes zero, and Equation 2.5 can be simplified as:

$$\sigma_{kS_{F,GLDAS}} = \left(\frac{k^2}{n-1} \sum_{i=1}^{n} (S_{F,GLDAS,i})^2 \right)^{0.5} \quad (2.6)$$

$$\sigma_{kS_{F,GLDAS}} = k\sigma_{S_{F,GLDAS}} \quad (2.7)$$

Using $\sigma_{kS_{F,GLDAS}}$ from Equation 2.7 in the expression $\alpha = r$ where $\alpha = \sigma_{kS_{F,GLDAS}} / \sigma_{S_{O,GLDAS}}$:

$$k = \frac{\sigma_{S_{O,GLDAS}}}{\sigma_{S_{F,GLDAS}}} r \quad (2.8)$$

Equation 2.8 indicates that the scale factor can be obtained analytically and is a function of standard deviations of filtered and original unfiltered TWSA time series if the means have been removed. Equation 2.8 also indicates that the scale factor is limited by the correlation between the filtered and original unfiltered time series. If the filtered and original unfiltered standard deviations are same, then one intuitively expects that no rescaling would be needed. However, the scale factor would equal the correlation, which reduces the variability of the rescaled TWSA time series relative to the original unfiltered time series. This potential issue can be addressed by determining scale factor using the condition $\alpha = 1$. Following the derivation in Equations 2.4 to 2.8, this condition produces the following scale factor:

$$k = \frac{\sigma_{S_{O,GLDAS}}}{\sigma_{S_{F,GLDAS}}} \quad (2.9)$$

To evaluate the use of NSE in rescaling the GRACE TWSA, we also perform the rescaling based on keeping $\alpha = 1$. We denote the scale factors from $\alpha = r$ and $\alpha = 1$ as $k_{\alpha=r,GLDAS}$ and $k_{\alpha=1,GLDAS}$, respectively.

GRACE rescaling based on complete water budget (CWB)

To evaluate the use of the Noah TWSA estimates in GRACE rescaling, we also implement a rescaling method based on a complete regional water balance. In particular, regional precipitation (P), evapotranspiration (E), and exiting streamflow (Q) datasets are used to estimate the changes in water storage (ΔS_{CWB}) :

$$\Delta S_{CWB,i} = P_i - E_i - Q_i \tag{2.10}$$

Equation 2.10 assumes that there is no net groundwater flow across the boundary of the study region. The change in water storage is similarly calculated from the rescaled filtered GRACE data (ΔS_{GRACE}):

$$\Delta S_{GRACE,i} = \frac{kS_{F,GRACE,i+1} - kS_{F,GRACE,i-1}}{2\Delta t} \tag{2.11}$$

where $S_{F,GRACE}$ is the filtered GRACE TWSA. The scale factor k is then analytically estimated using the $\alpha = r$ and $\alpha = 1$ conditions. In those conditions, ΔS from the filtered GRACE TWSA times series (ΔS_{GRACE}) is treated as the filtered time series (i.e., it determines the denominator in Equations 2.8 and 2.9), and ΔS from the CWB (ΔS_{CWB}) is treated as the unfiltered time series (i.e., it determines the numerator in Equations 2.8 and 2.9). The scale factors for the two conditions are denoted $k_{\alpha=r,CWB}$ and $k_{\alpha=1,CWB}$.

Groundwater estimates

GRACE provides estimates of the combined anomalies in the storage of water above, at, and below the ground surface. Groundwater storage anomalies can be estimated using datasets for the anomalies in the other stores of water within the region. Specifically, the groundwater storage anomalies can be estimated as (e.g., *Famiglietti et al.,* 2011; *Scanlon et al.,* 2012a):

$$S_{GW,i} = S_{GRACE,i} - S_{SM,i} - S_{SWE,i} - S_{SWS,i} \quad (2.12)$$

where S_{GW} is the groundwater storage anomaly, S_{GRACE} is rescaled filtered GRACE TWSA (obtained from one of the four cases described above), S_{SM} is the soil moisture anomaly, S_{SWE} is the SWE anomaly, and S_{SWS} is the surface water storage anomaly. In the mountainous regions, rock moisture may be one of the components of the overall water storage. However, because rock moisture data are unavailable, rock moisture is not included (like other studies of groundwater using GRACE such as *Famiglietti et al.,* 2011; *Scanlon et al.,* 2012a).

2.2.2 Study region

The study region is the combined the Sacramento and San Joaquin River basin in California, which includes the Central Valley (Figure 2.1). The Central valley has an area of about 52,000 km^2 while the combined basins have an area of about 153,000 km^2, which is comparable to the GRACE footprint. Almost 85% of the precipitation within the study region occurs in the mountains surrounding the Central Valley. Precipitation primarily falls as snow in the Sierra Nevada mountains making snowpack one of the major water reservoirs in the region (*Scanlon et al.,* 2012b). Spring snowmelt from these mountains provides major portion of water for the surface water reservoirs in the region (*Li et al.,* 2017). The Central Valley is one of the most productive agricultural regions in the world (*Escriva-Bou et al.,* 2020). Because the climate of

the region is Mediterranean to semiarid, the agriculture is sustained by irrigation from surface water and the underlying Central Valley aquifer (*Bertoldi* 1989; *Faunt et al.,* 2009). The Central Valley accounts for 1/6th of the U.S.A.'s irrigated land (*Famiglietti et al.,* 2011). Human activities have depleted the underlying aquifer since mid-1940s (*Konikow* 2015; *Russo et al.,* 2014), and significant reduction in groundwater in the southern San Joaquin valley has occurred since 1984 (*Argus et al.,* 2017). Groundwater consumption within the Central Valley accounts for 60% of the changes in the annual terrestrial water storage of the region (*Ghasemizade et al.,* 2019).

Both *Famiglietti et al.* (2011) and *Scanlon et al.* (2012a) assumed that changes in the groundwater storage within the study region are primarily due to the Central Valley. They also showed that estimated changes in groundwater storage from GRACE resemble observed and modelled changes in groundwater storage in the Central Valley. Therefore, we also assume that the groundwater storage changes derived from GRACE TWSA over the combined river basins predominantly represent the groundwater changes in the Central Valley.

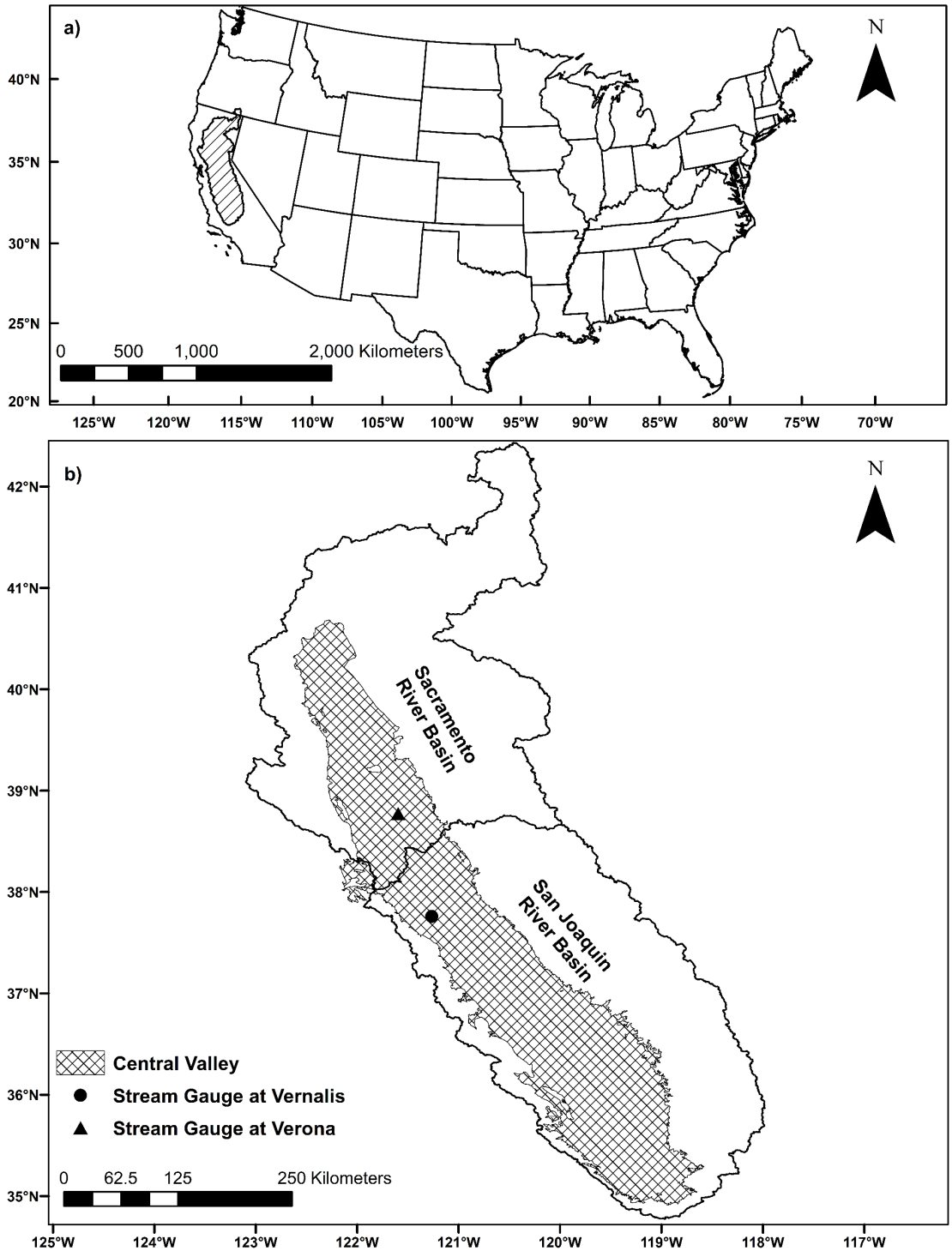

Figure 2.1. a) Location of study region within the U.S.A. and b) Central Valley location within the Sacramento and San Joaquin River basins, California.

2.2.3 Datasets

The rescaling of GRACE TWSA and corresponding groundwater depletion analysis are performed for January 2006-December 2010. The start of the study period is selected to match the availability of the GPS data, and the length of the study period is selected to avoid periods with missing GRACE data.

Terrestrial water storage

Basin-averaged (basin level) TWSA were obtained from the University of Colorado's GRACE data portal (http://geoid.colorado.edu/grace/). Basin-averaged TWSA are generated by the Center for Space Research at the University of Texas at Austin, GeoForschungsZentrum Potsdam, and the Jet Propulsion Laboratory. Basin-averaged GRACE TWSA for the Sacramento and San Joaquin River basins, which have been pre-processed to correct for post-glacial rebound (*A et al.,* 2013), filtered to remove North-South stripping (*Swenson and Wahr* 2006), and smoothed using a 300-km wide gaussian filter (*Swenson and Wahr* 2002) were downloaded. *Sakuma et al.* (2014) showed that taking the arithmetic average of TWSA processed by different data centres reduces the noise in the gravity field solutions. Therefore, the mean of the TWSA from the above-mentioned datasets was computed and utilized in this study. Then basin-averaged TWSA were averaged using weights based on the size of each basin to compute the average TWSA for the study area. In addition to GRACE TWSA, the GLDAS-Noah original unfiltered and filtered TWSA were downloaded from the University of Colorado's GRACE data portal.

TWSA from GPS were also obtained by inverting the vertical land surface displacement of 1019 GPS sites within the study region. The Earth's crust deforms elastically under the application and removal of loads. During the wet season, the crust subsidies because water,

snow, and ice are present on its surface, and it rebounds during the dry season when those loads are removed (*Amos et al.,* 2014). In a region with aquifers, the Earth's response also includes porous deformations when water enters or leaves the aquifers (*Argus et al.,* 2014; *Fu et al.,* 2015). The GPS sites located within the study region capture both the elastic and porous response of the Earth's surface in vertical land motion measurements. We obtained GPS-based total water storage estimates from sideshow.jpl.nasa.gov (*Argus et al.,* 2017). The GPS storage data were spatially averaged over the region and converted into anomalies by subtracting the mean for the study period.

Precipitation, evapotranspiration, and streamflow

The PRISM (Parameter-elevation Relationships on Independent Slopes Model) climate group at Oregon State University (http://www.prism.oregonstate.edu/) provides monthly gridded precipitation estimates from 1971 to the present at a spatial resolution of 4 km x 4 km for entire conterminous U.S.A. (*Daly et al.,* 2008). The gridded precipitation is estimated using more than 13,000 surface stations and a model that not only applies distance weighting but also includes the effects of topographic attributes such as elevation, aspect, and coastal proximity (*Jeong et al.,* 2020). PRISM's long-term average patterns agree with other gridded precipitation datasets across broad climate gradients (*Henn et al.,* 2018). PRISM is also consistent with United States Climate Reference Network estimates within all seasons and regions (*Buban et al.,* 2020). *Daly et al.* (2008) showed that the mean absolute error of PRISM ranges from 5 mm to 13 mm within a year for the western U.S.A. The monthly PRISM precipitation values were averaged over the study region and converted into anomalies by subtracting the mean for the study period. See Figure A1 (Appendix A) for a map of mean

monthly precipitation.

The evapotranspiration data product (MOD16) from the Moderate Resolution Imaging Spectroradiometer (MODIS) was used. MOD16 is computed by the Numerical Terradynamic Simulation Group at University of Montana (*Mu et al.,* 2011) using the Penman-Monteith equation and land cover type, leaf area index, and albedo from MODIS. This evapotranspiration product is the sum of evaporation from wet canopy surfaces, transpiration by the vegetation, and evaporation from the soil surface. The evapotranspiration estimates have a mean absolute error of 0.33 mm/day when compared to the observations from eddy flux towers (*Mu et al.,* 2011). Monthly evapotranspiration estimates from MOD16 (0.05^{o} grids) were extracted, averaged for the study region, and converted to anomalies by subtracting the mean for the study period. See Figure A2 for a map of mean monthly evapotranspiration.

The study area is drained by the Sacramento and San Joaquin River basins. Streamflow data for two gauges located at Verona (USGS gauge 11425500) and Vernalis (USGS gauge 11303500) on Sacramento and San Joaquin Rivers, respectively, were obtained from the National Water Information System of the United States Geological Survey (USGS) (http://waterdata.usgs.gov/nwis/). Figure 2.1 shows that these stream gauges are located upstream of the outlet of their respective river basin; however, these are the most downstream gauges that provide continuous observations of the flows in the Sacramento and San Joaquin rivers for the study period. Because the two selected streamflow gauges do not represent the complete river basins, the exiting streamflow estimates from these gauges may be underestimated or overestimated. The total streamflow was computed as the sum of the streamflow measured at two the gauges. This total was converted into equivalent water

thickness by dividing it by total area of the region and then into anomalies by subtracting mean streamflow for the study period.

Soil moisture, SWE, and surface water

Soil moisture and SWE anomalies are required to estimate groundwater depletion. Given that the GRACE is a global hydrologic tool, soil moisture and SWE are estimated from global datasets. The complete soil moisture profile and SWE are largely unmonitored in most areas (*Famiglietti et al.,* 2011), so numerous studies have used modelled soil moisture and SWE from the GLDAS framework (e.g., *Feng et al.,* 2013; *Hu et al.,* 2019; *Rodell et al.,* 2007). In this study, we used the modelled monthly estimates of soil moisture and SWE available from the Catchment Land Surface Model (CLSM; 1^{o}), Noah (0.25^{o} and 1^{o}), and Variable Infiltration Capacity model (VIC; 1^{o}) from GLDAS (*Rodell et al.,* 2004). Noah models soil moisture in four layers up to a 2 m depth. VIC models soil moisture in three layers where, for the study region, the surface layer is 0.30 m thick, second layer is 2.50 m thick, and third layer is 0.25 m thick. CLSM models the soil moisture as a profile including surface and root zone regions. Monthly soil moisture and SWE grids were averaged for the study area and converted to anomalies by subtracting the mean for the study period.

Monthly surface water storage data for the study region were collected from the California Data Exchange Center. Reservoir storages for 48 lakes/reservoirs were available as volumes of water stored, which were converted to an equivalent water thickness by summing up all the storage volumes for a particular month and dividing by the area of the study region. Anomalies of surface water storage were then calculated by subtracting the mean for the study period.

2.3 Results

2.3.1 Scaling of GRACE TWSA

The scale factors obtained by maximizing NSE (i.e., $k_{\alpha=r,GLDAS}$) and optimizing relative variability (i.e., $k_{\alpha=1,GLDAS}$) between the filtered and original unfiltered GLDAS TWSA are 1.91 and 1.97, respectively, for the study region and period. Given that the correlation between filtered and original unfiltered GLDAS TWSA is very high (r = 0.97), two scale factors do not differ much from each other. Table 2.1 shows the Pearson correlation, relative variability, bias, and NSE values when both the rescaling factors are applied to the GRACE data and the resulting TWSA are compared with the GPS TWSA. The relative variability values indicate that the two rescaled GRACE TWSA have slightly more than 50% of variability in the GPS TWSA. Both rescaled GRACE TWSA have similar NSE values because the two scale factors $k_{\alpha=r,GLDAS}$ and $k_{\alpha=1,GLDAS}$ are similar.

Table 2.1. Pearson correlation (r), relative variability (α), bias (β), and NSE between GRACE TWSA that are rescaled using GLDAS and GPS TWSA time series.

Scale Factor	Correlation (r)	Relative Variability (α)	Bias (β)	NSE
$k_{\alpha=r,GLDAS}$	0.93	0.54	0.00	0.71
$k_{\alpha=1,GLDAS}$	0.93	0.56	0.00	0.72

Figure 2.2 compares the two rescaled GRACE TWSA to the GPS TWSA. Figure 2.2a & b shows that the scatter plots of the two rescaled GRACE TWSA are not well aligned with the 1:1 line because they underestimate the TWSA variability. Both the rescaled TWSA tend to overestimate the GPS TWSA in dry months (i.e., for negative anomalies) and underestimate the GPS TWSA in wet months (i.e., for positive anomalies). Figure 2.2c compares the time series of the two GRACE TWSA with GPS TWSA. Both rescaled GRACE TWSA follow the variations in the

GPS TWSA well (and have a high correlation as shown in Table 2.1). The rescaled GRACE TWSA show a decreasing trend during the study period, but the trend has a smaller magnitude than the GPS TWSA. Neither GRACE TWSA captures the full decreases in the GPS TWSA during phases when the GPS TWSA decreases.

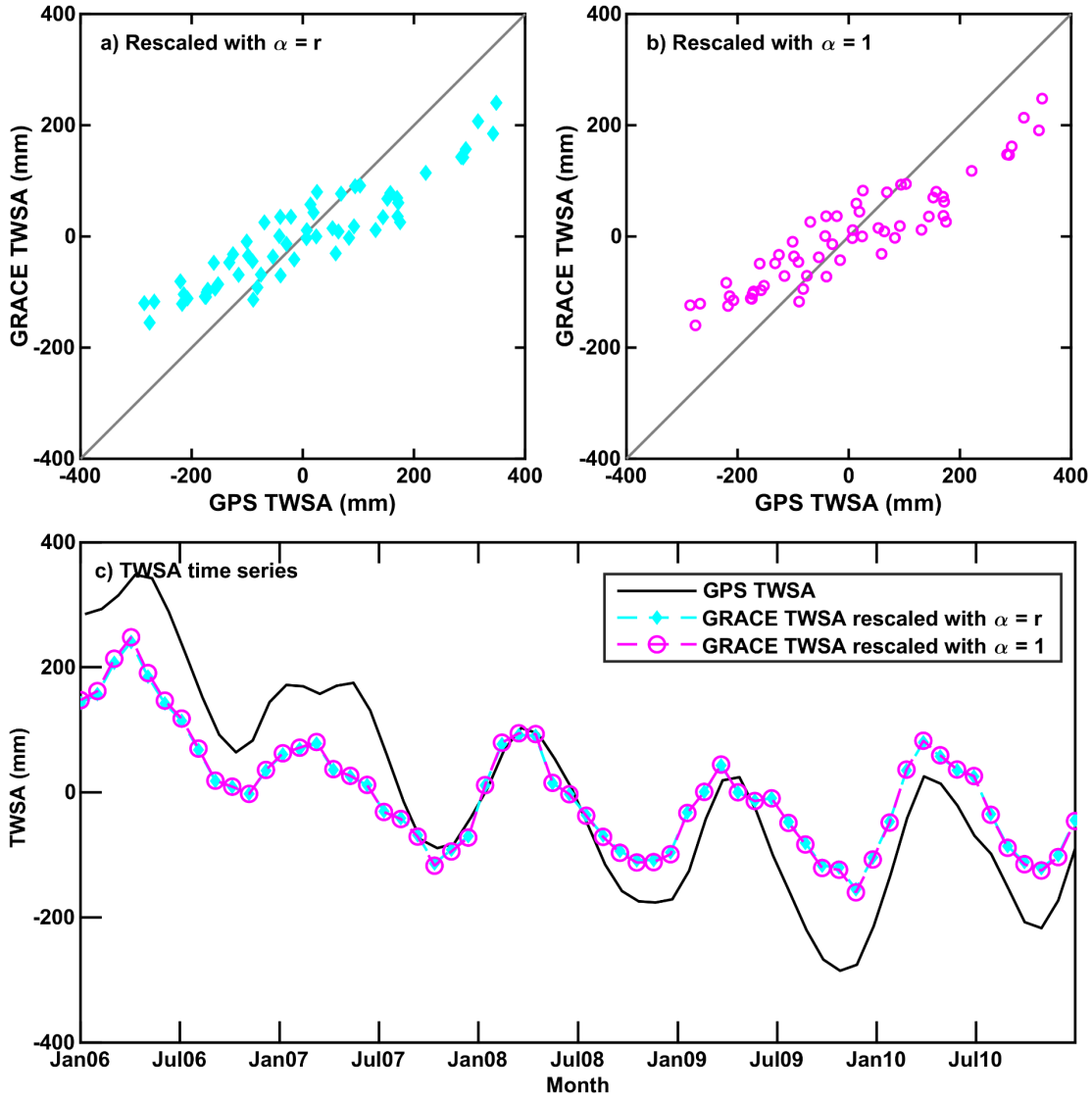

Figure 2.2. Comparison of GLDAS-based rescaling of GRACE TWSA with GPS TWSA. a) scatter plot of GRACE TWSA rescaled with $\alpha = r$ and GPS TWSA; b) scatter plot of GRACE TWSA rescaled with $\alpha = 1$ and GPS TWSA; and c) time series of GRACE and GPS TWSA

The scale factors obtained by maximizing NSE (i.e., $k_{\alpha=r,CWB}$) and optimizing relative variability (i.e., $k_{\alpha=1,CWB}$) between ΔS_{CWB} and ΔS_{GRACE} are 2.75 and 3.18, respectively. Table 2.2 shows the Pearson correlation, relative variability, and NSE values when the rescaling factors are applied to the GRACE data and the resulting TWSA are compared with the GPS TWSA. The relative variability of the GRACE TWSA rescaled with $k_{\alpha=1,CWB}$ is substantially higher than the one

rescaled with $k_{\alpha=r,CWB}$ and closer to the ideal value of one. Larger differences are observed between the cases in Table 2.1 than Table 2.2 because the correlation between the two ΔS times series is lower (r = 0.85) than the correlation between the filtered and original unfiltered GLDAS times series (r = 0.97). Once again, enforcing $\alpha = 1$ produces a slightly higher NSE than enforcing $\alpha = r$. Figure 2.3 compares the two CWB-rescaled GRACE TWSA to the GPS TWSA. Figure 2.3a & b shows that the $\alpha = 1$ case aligns better with the 1:1 line than the $\alpha = r$ case. However, Figure 2.3c shows that the difference between the two cases remains small.

Table 2.2. Pearson correlation (r), relative variability (α), bias (β), and NSE between GRACE TWSA that are rescaled using the CWB and GPS TWSA time series.

Scale Factor	Correlation (r)	Relative Variability (α)	Bias (β)	NSE
$k_{\alpha=r,CWB}$	0.93	0.78	0.00	0.84
$k_{\alpha=1,CWB}$	0.93	0.91	0.00	0.86

The effect of using the CWB instead of GLDAS for scaling can be seen by comparing Table 2.2 to Table 2.1. The relative variability and NSE are all substantially improved when the CWB approach is used. Similarly, comparing Figure 2.3 to Figure 2.2 shows that using the CWB approach better reproduces the range of variation and overall trend in the GPS data. Overall, optimizing the relative variability ($\alpha = 1$) and using the CWB approach together produce a substantial improvement in the NSE for the study region. While the rescaling factor from the pre-existing method ($k_{\alpha=r,GLDAS}$) produces an NSE of 0.71, the rescaling factor from the two proposed modifications ($k_{\alpha=1,CWB}$) produces an NSE of 0.86.

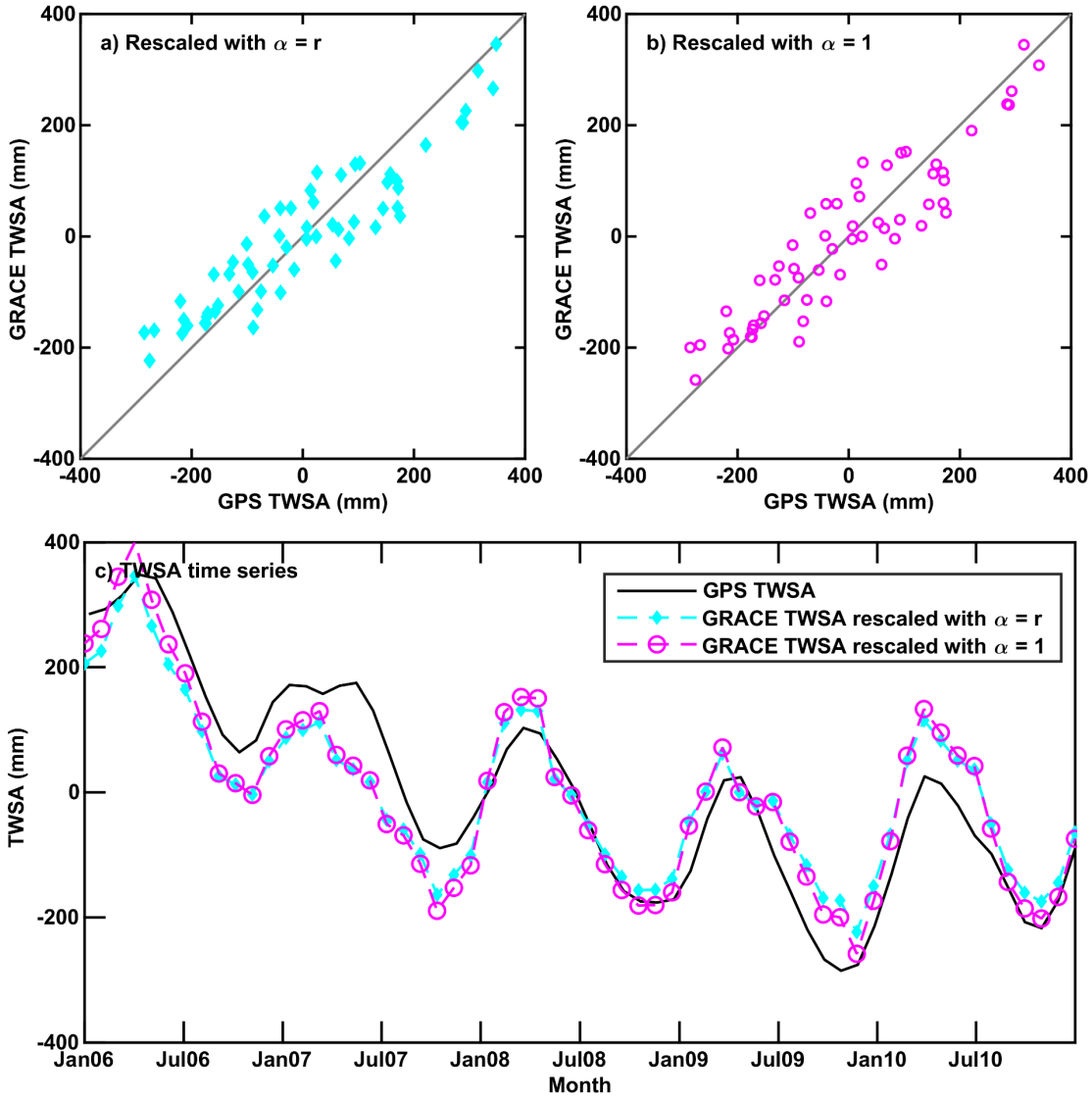

Figure 2.3. Comparison of CWB-based rescaling of GRACE TWSA with GPS TWSA. a) scatter plot of GRACE TWSA rescaled with $\alpha = r$ and GPS TWSA; b) scatter plot of GRACE TWSA rescaled with $\alpha = 1$ and GPS TWSA; and c) time series of GRACE and GPS TWSA

2.3.2 Groundwater depletion estimates

Figure 2.4 compares the time series of the groundwater storage anomalies (GWSA) estimated from GRACE TWSA rescaled with $k_{\alpha=r,GLDAS}$ (the pre-existing method) and $k_{\alpha=1,CWB}$ (the two proposed modifications). As discussed earlier, separate GWSA were calculated using soil moisture and SWE anomalies from four global hydrology models. For simplicity, the results in Figure 2.4 show the minimum, average, and maximum GWSA from the four models at each

time. The average GWSA from both rescaling methods show decreasing trends. However, the trend from the GRACE TWSA rescaled with $\alpha = 1$ and CWB is more pronounced and suggests more depletion than the trend from the GRACE TWSA rescaled with $\alpha = r$ and GLDAS. In particular, the GWSA time series from $k_{\alpha=1,CWB}$ shows a decline commencing in 2006 whereas the GWSA time series from $k_{\alpha=r,GLDAS}$ shows a decline commencing in 2009. Figure 2.4 shows that the seasonal cycles of GWSA from $k_{\alpha=r,GLDAS}$ and $k_{\alpha=1,CWB}$ are different. Precipitation is typically largest in December to February, and it mainly occurs as snowfall in the Sierra Nevada mountains (*Ukasha et al.,* 2022). Snowmelt occurs in late spring and early summer, and the associated elevated streamflow recharges the aquifer of the Central Valley aquifer (*Gilbert and Maxwell* 2018). Thus, the GWSA are expected to increase in late spring and early summer. Irrigation in the region peaks from June to August (*Yang et al.,* 2017), so the GWSA are expected to decrease in this period. For the $k_{\alpha=r,GLDAS}$ case, seasonal depletion occurs around September. For the $k_{\alpha=1,CWB}$ case, seasonal depletion typically begins around July.

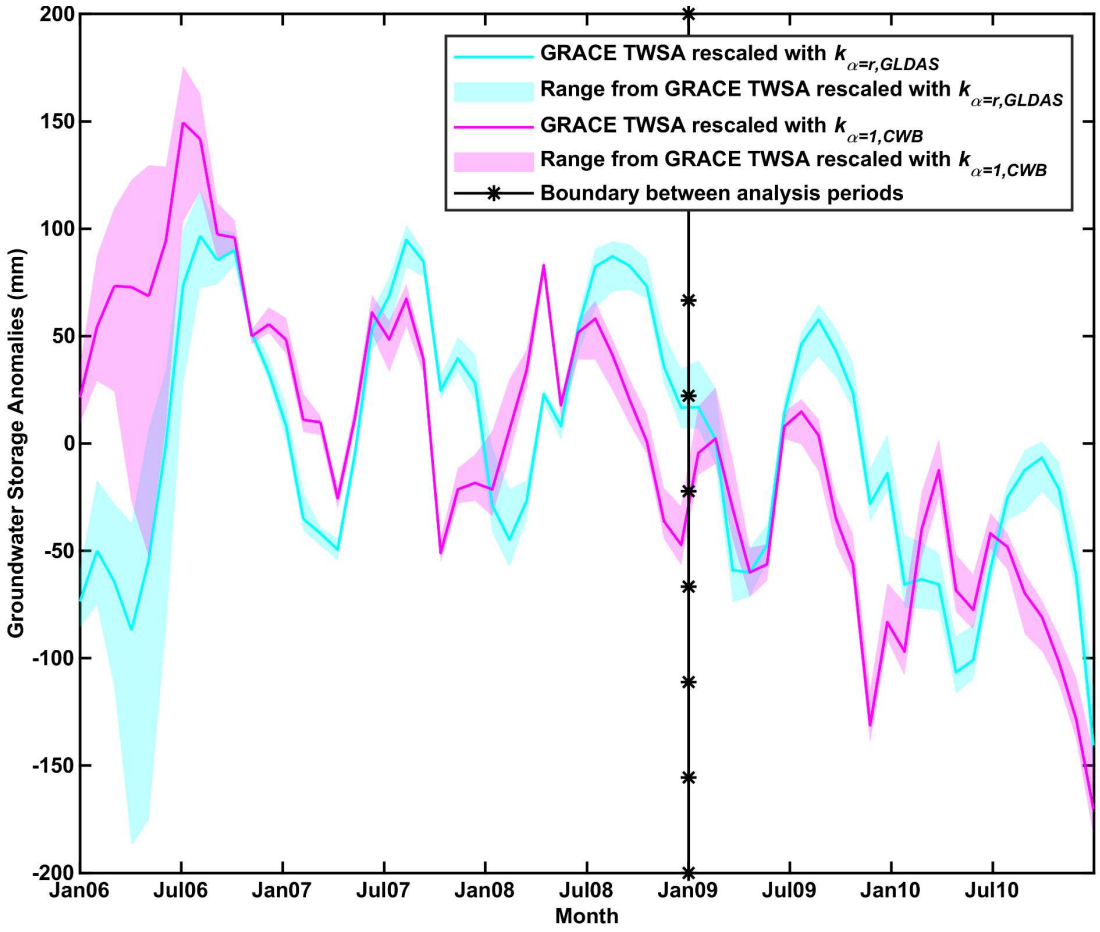

Figure 2.4. Time series of groundwater storage anomalies from GRACE TWSA rescaled with $k_{\alpha=r,GLDAS}$ and $k_{\alpha=1,CWB}$

Table 2.3 examines the change in groundwater storage based on GRACE TWSA rescaled with $k_{\alpha=r,GLDAS}$ and $k_{\alpha=1,CWB}$ for two different time periods. For 2006-2008, the average GWSA from $k_{\alpha=r,GLDAS}$ and $k_{\alpha=1,CWB}$ show contrasting trends. The average GWSA from $k_{\alpha=r,GLDAS}$ (i.e., pre-existing methodology) shows a positive trend and therefore results in an accumulation of groundwater by the end of 2008. In fact, the GWSA estimates from $k_{\alpha=r,GLDAS}$ show a positive trend for all models considered (the minimum trend is 12.2 mm/yr). Among models, VIC-based GWSA show the least accumulation and CLSM-based GWSA show most accumulation. In

contrast, the average GWSA from $k_{\alpha=1,CWB}$ (i.e., the two proposed modifications) shows a negative trend and overall reduction in groundwater storage during this period. Moreover, the GWSA from $k_{\alpha=1,CWB}$ show a decreasing trend irrespective of the model used. The VIC-based GWSA shows the most depletion and CLSM-based GWSA shows the least depletion. The Noah-based and VIC-based GWSA are similar while the CLSM-based GWSA estimates differ substantially from the others.

For 2009-2010, the GWSA based on GRACE TWSA rescaled with $k_{\alpha=r,GLDAS}$ and $k_{\alpha=1,CWB}$ both show negative trends and thus net groundwater depletion. However, the GWSA from $k_{\alpha=1,CWB}$ shows substantially more depletion than the GWSA from $k_{\alpha=r,GLDAS}$. For a given rescaling method, the quantitative estimates of groundwater depletion exhibit notable difference depending on the model used, suggesting that the SWE and soil moisture estimates include considerable uncertainty.

Table 2.3. Average rate of increase (mm/yr) and total increase (km^3) in groundwater storage from GRACE TWSA rescaled with $k_{\alpha=r,GLDAS}$ and $k_{\alpha=1,CWB}$ during the study period. For each case, values are minimum (left), average (middle), and maximum (right). Negative values indicate depletion.

	Rates of Change (mm/yr)		**Total Volume (km^3)**	
	$k_{\alpha=r,GLDAS}$	$k_{\alpha=1,CWB}$	$k_{\alpha=r,GLDAS}$	$k_{\alpha=1,CWB}$
Jan. 2006 – Dec. 2008	12.2, 24.2, 47.8	-42.3, -30.3, -6.5	5.6, 11.1, 22.0	-19.4, -13.9, -3.0
Jan. 2009 – Dec. 2010	-43.9, -39.4, -35.9	-58.4, -53.8, -50.4	-13.4, -12.1, -10.9	-17.8, -16.5, -15.4

2.4 Discussion

The derivation presented earlier shows that maximizing NSE produces a scale factor that depends on the standard deviations of the filtered and original unfiltered TWSA time series and the correlation between the two time series. Because the result of the maximization can be determined analytically (Equation 2.8), numerical optimization is not needed to determine the scale factor. In addition, the relative variability between the rescaled filtered TWSA and original unfiltered TWSA time series equals the correlation between these time series (i.e., $\alpha = r$). Therefore, the variability of the rescaled TWSA time series is always less than the variability in original unfiltered TWSA time series. This tendency might be disadvantageous because the purpose of rescaling is to restore the variation that is lost due to filtering.

An alternative method was proposed where the scale factor is selected so that standard deviation of the rescaled filtered TWSA matches the standard deviation of the original unfiltered TWSA (i.e., $\alpha = 1$). This approach always produces a higher scale factor than Maximizing NSE unless the filtered and original unfiltered TWSA are perfectly correlated (in which case the two approaches are identical). The difference between the two methods is greater when the filtered and original unfiltered TWSA have lower correlation. This alternative method for determining the scale factor (i.e., enforcing $\alpha = 1$) can also be implemented without using numerical optimization and can be applied to any region of interest. When the proposed method was applied to the study region, the resulting TWSA were slightly more similar than the $\alpha = r$ case to the independent TWSA estimates from GPS. Future research should compare these methods for other study regions where independent estimates of TWSA are available because it is not clear whether the $\alpha = 1$ approach will typically outperform the

$\alpha = r$ case. This study also considered a period in which the GRACE data were complete. The effects of missing data on the results should also be considered.

The scale factor from the CWB method was also larger than the scale factor from the GLDAS method. The two scale factors are expected to diverge more when the stores of water that the GLDAS models neglect are more important. Thus, larger differences are expected in regions with major aquifers, which are often the regions where GRACE data are used most. The CWB method is expected to produce a larger scale factor than the GLDAS method whenever the variation of the total water storage is larger than the variation in the storage represented in GLDAS. Thus, the CWB approach will produce larger scale factors in regions where the seasonal variations of SWE, soil moisture, and groundwater are aligned. The CWB method is expected to outperform the GLDAS method because the target that is used to determine the scale factor (ΔS_{CWB}) is more closely related to the GRACE data to which the scale factor is applied. However, testing in other regions is needed. The CWB method also requires precipitation, evapotranspiration, and streamflow data, so it cannot be applied where such data are unavailable. Its performance will be worse where these data are less accurate.

The results show that capturing the range of relative variability can have significant impacts on the groundwater storage anomalies. Larger scale factors are expected to increase trends in the TWSA. Rescaling the GRACE data with $\alpha = 1$ and the CWB method for the study region better captured the variability in the GPS TWSA and resulted in more substantial estimates of groundwater depletion. The estimated groundwater volume changes resemble those in previous studies by *Famiglietti et al.* (2011) and *Scanlon et al.* (2012a). Public sector water management organizations such as California Department of Water Resources could use

groundwater depletion information to assess the impact of droughts on regional groundwater resources and estimate the water productivity of the region based on the crop yield. This could also indicate the effectiveness of any policy or management decision implemented for regional water management.

Studies have shown that a portion of streamflow originates from groundwater stored in the fractured bedrock of Sierra Nevada mountains (e.g., *Ciruzzi and Lo*wry, 2017; S*omers and McKenzie,* 2020; *Uriostegui et al.,* 2016). Thus, the estimates of groundwater depletion may include changes in the rock moisture within the region. Groundwater depletion estimated from rescaled GRACE TWSA should be evaluated in regions where rock moisture is either known to be insignificant or has been accurately estimated.

2.5 Conclusions

This study focused on GRACE TWSA rescaling, which is used to overcome the loss of variance that occurs when GRACE TWSA are filtered to reduce errors. First, it compared the use of NSE as an objective function to an alternative method that restores the variance of the original unfiltered TWSA time series. Second, it compared rescaling based on GLDAS to rescaling based on a CWB inferred from regional precipitation, evapotranspiration, and streamflow data. Third, it examined the impacts of the rescaling method on estimates of groundwater repletion. Based on results for the combined Sacramento and San Joaquin River basins in California, USA, the following conclusions can be drawn.

1. If the scale factor is selected by maximizing NSE, the relative variability between the rescaled filtered TWSA time series and the original unfiltered TWSA time series always matches the correlation between the two time series (i.e., $\alpha = r$). Thus, the rescaled

filtered TWSA always have less variation than the original unfiltered TWSA unless the two time series are perfectly correlated.

2. If the scale factor is selected so that the rescaled filtered TWSA have the same variance as the original unfiltered TWSA (i.e., $\alpha = 1$), the resulting TWSA are slightly more similar to independent estimates of TWSA from GPS for the study region. This improvement occurs irrespective of whether the rescaling is performed using the GLDAS or CWB method. Larger differences between the $\alpha = r$ and $\alpha = 1$ methods are expected to occur for cases where the correlation between the two time series is lower.
3. Rescaling with CWB instead of GLDAS results in a substantially larger scale factor for the study region and the resulting TWSA show substantially better agreement with the independent TWSA from GPS. The larger scale factor is expected because the CWB includes variations in water stores that are not included in GLDAS (especially groundwater). Larger differences between the CWB and GLDAS methods are expected to occur for regions where groundwater is an important component of the TWSA and where the variations in soil moisture, SWE, and groundwater storage are aligned.
4. When the scale factor is estimated using $\alpha = 1$ and CWB (rather than the pre-existing method using $\alpha = r$ and GLDAS), the resulting estimates of groundwater depletion in the Central Valley are larger and began earlier. In particular, depletion appears to have occurred between 2006 and 2008, which is not observed using the pre-existing approach. This change in behaviour occurs irrespective of whether the soil moisture and SWE are estimated using VIC, CLSM, or Noah in GLDAS.

Chapter 3 Scale-invariant behavior and stochastic downscaling of terrestrial water storage anomalies

3.1 Introduction

Gravity Recovery and Climate Experiments (GRACE) and its follow on mission (GRACE-FO) is the observation tool which provides an integrated picture of water storage, however, at coarse temporal (monthly) and spatial (4^o) resolutions (*Kornfeld et al.,* 2019; *Tapley et al.,* 2004 a,b). GRACE and GRACE-FO observations are satellite based and are available as TWS anomalies (TWSA; i.e., deviations from long-term mean TWS) since 2002. These TWSA have significantly contributed to enhancing the understanding of hydrological cycle and its interactions with climate, ecosystems, and socio-economic processes at regional to global scales (e.g., Syed *et al.*, 2008; *Ahi et al.,* 2021; *Fatolazadeh et al.,* 2021; *Hasan et al.,* 2021; *Liu et al.,* 2021; *Tangdamrongsub et al.,* 2021a,b; *Zhu et al.,* 2021). In combination with auxiliary information on significant water storage components, GRACE and GRACE-FO observations have been used to estimate groundwater storage changes in large aquifers located in different eco-hydroclimatic zones (e.g., *Bi and Rodell,* 2021; *Guo et al.,* 2022; *Mohamad et al.,* 2020; *Richey et al.*, 2015a,b; *Sharifi et al.,* 2022; *Xanke et al.,* 2022). Near real time monitoring and prediction of hydrological extremes *i.e.,* floods and droughts has seen significant improvements due to incorporation of TWSA observations (see *Cui et al.,* 2021; *Latinovic et al.,* 2021; *Mo et al.,* 2022; *Nigatu et al.,* 2021; *Reager et al.*, 2014; *Tangdamrongsub et al.,* 2021b; *Thomas et al.*, 2014; *Zhong et al.,* 2022). *Girotto et al.* (2016); *Houborg et al.* (2012); *Kumar et al.* (2016); *Li et al.* (2012); *Zaitchik et al.* (2008) and some others demonstrated enhanced modeling skills of land surface models after assimilating GRACE TWSA. Furthermore, this dataset has been used in parameter estimation and

calibration of hydrological and groundwater models (e.g., *Qiao et al.*, 2013; *Sun et al.*, 2010, 2012). Potential of GRACE observations in ecohydrological analysis has been demonstrated by numerous studies including *A et al.* (2015); *Maeda et al.* (2015); *Ukasha et al.* (2022); and *Yang et al.* (2014).

The coarse spatial resolution of GRACE and GRACE-FO observations limits its applicability at smaller scales. To enhance understanding of spatial patterns in hydroclimatic variability, groundwater storage and other related processes, TWSA observations at much finer resolutions compared to GRACE resolution are required. Therefore, numerous statistical methods (e.g., regression equations) and physically based dynamic procedures have been developed to perform deterministic spatial downscaling of GRACE and GRACE-FO TWSA. For example, sub-basin scale groundwater storage anomalies for California's Central Valley aquifer were obtained using linear relationship between GRACE TWSA based aquifer scale groundwater storage and spline of groundwater storage obtained from the California Central Valley Groundwater-Surface Water Simulation Model (*Kuss et al.*, 2012). A study by *Ning et al.* (2014) used satellite-based estimates of precipitation (P) and evapotranspiration (ET), and runoff (Q) from Global Land Data Assimilation System to construct a nonlinear regression model relating water budget (P-ET-Q) with 1^{o} gridded GRACE TWSA. Ultimately, they used the model to downscale TWSA to 0.25^{o} and evaluated it against groundwater well levels located in Yunnan province, China. *Gemitzi et al.* (2021) downscaled 1^{o} GRACE-FO TWSA for Thrace and Thessaly regions by first regressing it against 1^{o} precipitation obtained from upscaling of 0.1^{o} Global Precipitation Mission product and then using 0.1^{o} precipitation in the regression equation to estimate 0.1^{o} TWSA. They found that the regression equation for GRACE-FO TWSA is also

applicable to GRACE TWSA for their study regions. Artifical Neural Network (ANN) scheme was employed by *Yirdaw and Snelgrove* (2011) and *Sun* (2013) to estimate groundwater level changes in a well for Assiniboine Delta aquifer in Canada and multiple sites in the U.S.A, respectively using observations on groundwater level from wells, and precipitation. ANN's were found to be successful in estimating point-scale groundwater changes, however, it requires significant amount of training data to accurately map the relationship between large-scale and small-scale processes. Physically based disaggregation has been done by assimilating GRACE TWSAs into land surface models (see *Girotto et al.*, 2016; *Houborg et al.*, 2012; *Kumar et al.*, 2016; *Li et al.*, 2012; *Zaitchik et al.*, 2008). However, these models usually do not explicitly model groundwater and surface water storages i.e., complete TWSA is not modeled and therefore, may have inaccurate spatial variation of TWSA. Furthermore, given the different forcing and non-unique model structures, modeled TWSA are highly uncertain. More recently, machine learning algorithms have been used to downscale TWSA using modeled and observed hydroclimatic variables (e.g., *Chen et al.,* 2021; *Seyoum et al.,* 2019; *Yin et al.,* 2022). These procedures require high resolution information on different hydro-climatological variables and/or water storage components, which is obtained as *in-situ* (not globally available) or remote sensing observations, model estimates or their combination. More importantly these downscaling methods focused on estimating local TWSA without considering the conservation of statistical properties of TWSA at fine resolutions. Therefore, the fine resolution TWSA from deterministic models may miss the extreme TWSA values that may occur within a large region.

Extreme TWSA values that may occur at finer resolutions in a region is important for estimating the probability of small scale droughts and floods, and how these extreme events

relate to other characteristics of the region. Estimating the probabilities at fine resolutions is also relevant to firms that insures crops and infrastructure to assess the various risks and inform policy decisions regarding premium. Therefore, the objective of this study is to capture the extreme TWSA values at fine resolutions by reproducing the statistical properties of coarse resolution TWSA. To accomplish this we hypothesized that spatial patterns of GRACE and GRACE-FO TWSA are scale-invariant. And consequently, fine resolution TWSA that preserves the statistical properties can be estimated using multiplicative random cascade models (MRCM). Analysis of scale-invariance of hydroclimatic variables such as precipitation, soil moisture and snow field depths have shown that these quantities exhibit the property of statistical scale-invariance (e.g., *Deems et al.*, 2006; *Ji et al.*, 2016; *Kuchment and Gelfan*, 2001; *Molnar and Burlando*, 2005; *Neuhauser et al.,* 2019; *Pons et al.,* 2022; *Veneziano et al.,* 1996; *Verrier et al.,* 2022). The scale invariance analysis is a statistical procedure that identifies the scaling structure by upscaling fine resolution hydroclimatic variable to successive coarser resolutions. MRCM are stochastic models that reproduce the statistical properties of the hydroclimatic variables that are scale-invariant across different scales (see *Hosseini et al.*, 2013; *Kang and Ramirez*, 2010; *Mascaro et al.*, 2010; *Molnar and Burlando*, 2005; *Pons et al.,* 2022; *Rupp et al.*, 2012; *Verrier et al.,* 2022), more specifically from coarser to higher resolutions i.e., downscaling of the hydroclimatic variables. The parameters of the MRCMs are determined by the model itself and from the scaling structure of the hydroclimatic variable. In this study we used the gridded 0.25^{o} monthly GRACE, GRACE-FO and global positioning system (GPS)-based TWSA for three regions across the globe having different climatic, geological, and physiographic characteristics. These characteristics exert controls on terrestrial water storage variations and

therefore, characterizes the spatial patterns, statistical properties and scaling structure of TWSA. For each region, we started with testing for the presence of log-log linear relationship between moments of TWSA and different resolutions (0.25^o to 4^o) at which those moments are computed to infer scale-invariance of TWSA. Then type of scale-invariance was ascertained that parameterized the lognormal MRCM. And finally, MRCM was applied to estimate the fine resolution (0.0625^o) TWSA that approximately reproduced the statistical properties of coarse resolution (0.25^o to 4^o) TWSA.

3.2 Data and Methods

3.2.1 Study Regions

The study was conducted for i) Amazon river basin in Brazil, ii) Sindh province in Pakistan, and iii) around California, U.S.A (see Figure 3.1). Three regions selected for analysis and downscaling represents different climatic, geologic, and physiographic characteristics. Region selected within Amazon basin for this study is located within the Amazon floodplains (*Paiva et al.,* 2013) characterized by flat topography. The region is seasonally flooded (*Paiva et al.,* 2013) that results in high recharge (>100 mm/year) to shallow (i.e., local) and deep (uniform and large sedimentary) groundwater aquifers in the region (*Hoekstra et al.,* 2010). Given its seasonally flooded nature, surface remains somewhat saturated throughout the year, and thus, river and flood waters partially dominates the terrestrial water storage variations in the region (*Pokhrel et al.,* 2013). Sindh province in Pakistan is the most downstream riparian area of the Indus River. The province has a flat topography and is characterized by low recharge (<20 mm/year) deep aquifer (*Hoekstra et al.,* 2010). The region is primarily waterlogged and is poorly drained (*Lytton et al.,* 2021). The region selected around California comprises of highly productive

Central Valley and to the east of the Central Valley the snow-clad mountain ranges of Sierra-Nevada. Western US is under drought for two decades, where Southern California has been severely impacted (*Herrmann et al.,* 2016). The selected region is characterized by low recharge aquifers (*Hoekstra et al.,* 2010) and topographic variation ranging from a flat valley to high mountains. Western US is under drought for two decades, where Southern California has been severely impacted (*Herrmann et al.,* 2016). In response to the drought, the groundwater usage significantly increased within the valley. This resulted in long-term depletion of groundwater within the Central Valley that has been shown by decreasing trends in surface mass anomalies captured by GRACE (*Alam et al.,* 2021).

Given that the procedure to investigate the scale-invariant behavior required the study region to have a square boundary, within each of the above-mentioned regions we selected an area of having 4^{o} degree extent in north-south and east-west direction. This equates having sixteen 0.25^{o} pixels each in north-south and east-west directions (or 256 pixels).

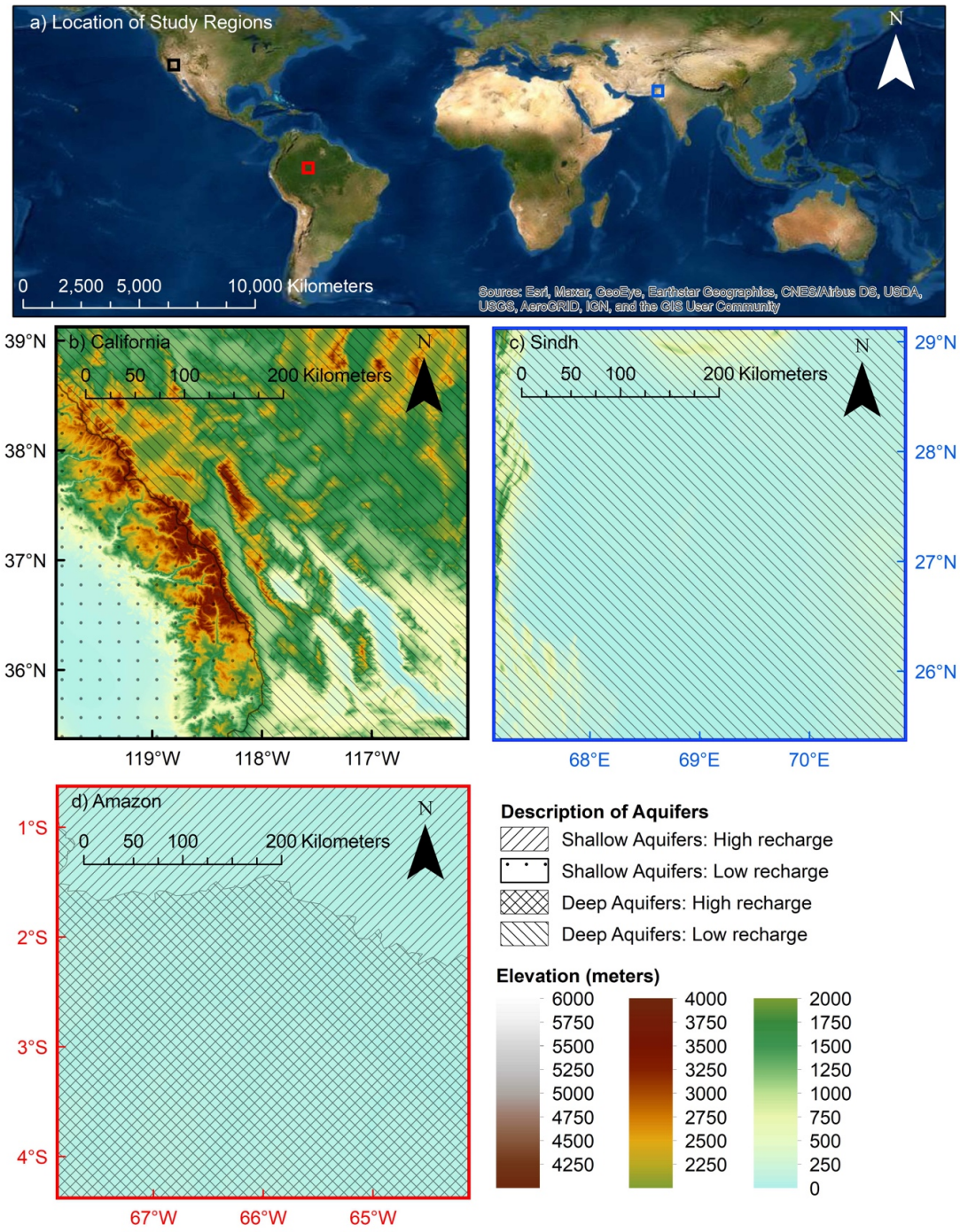

Figure 3.1. a) Location of study regions in the world; b) topographic and hydrogeologic characteristics of study region in California; c) topographic and hydrogeologic characteristics of Sindh; d) topographic and hydrogeologic characteristics of study region in Amazon. Hydrogeologic characteristics adopted from Hoekstra et al. (2010).

3.2.2 Datasets

In this study we used the gridded 0.25^{o} monthly GRACE and GRACE-Follow On mass concentration (MASCON) solutions of TWSA (*Save et al.,* 2016) from April 2002 to December 2021 (few months are missing in the available dataset and therefore TWSA of 204 months is available and was used for analysis). This dataset is produced by the Center of Space Research, University of Texas at Austin and unlike traditional TWSA product based on spherical harmonics, MASCON product does not require any post-processing to correct for leakage, measurement and spatial correlation errors. In addition to GRACE TWSA, for California region, we also collected Global Positioning System (GPS) based TWSA from January 2006 to December 2021 (total of 187 months). GPS measures vertical displacement of the earth surface in response to elastic loading and unloading (surface water, snow, and soil moisture), and porous response to depletion and recharge of underlying groundwater aquifer (*Argus et al.,* 2014).

3.2.3 Methods

3.2.3.1 Transformation of TWSA

Given that the water storage data from GRACE and GPS are anomalies, therefore, moments for moment orders other than 1 and even numbers cannot be estimated. The cascade generators also take the form of nonnegative numbers, therefore, TWSA dataset needed to be transformed to have only nonnegative numbers. To this end, we transformed the TWSA data for a particular month by adding in it 1.1 times the absolute of minimum TWSA for that month. This resulted in minimum value of transformed TWSA always greater than zero. Even after the transformation, zero does not mean complete absence of water and thus not comparable between months for the same region.

3.2.3.2 Scale-invariance of TWSA

This section defines scale-invariance and the procedure to test the hypothesis that whether or not TWSA is scale-invariant. Scale-invariant behavior of hydroclimatic variables such as precipitation, and soil moisture is defined by (e.g., see *Kang and Ramirez,* 2010; *Mascaro et al.,* 2010):

$$S(\lambda L) \overset{dist}{=} \lambda^{-\tau} S(L) \qquad 3.1$$

where S is transformed TWSA, L is the resolution of variable S, λ is the scale ratio, and τ is the scaling exponent. The equation implies that the probability distribution of S at resolution λL is same as of at resolution L times the factor which is the function of scale ratio λ and scaling exponent τ. Equation 3.1 can be re-written in the form of moment order (q):

$$\ln\langle S_{\lambda L}^{q}\rangle = -\tau(q)\ln(\lambda) + \ln\langle S_{L}^{q}\rangle \qquad 3.2$$

Where $\langle S_{\lambda L}^{q}\rangle$ and $\langle S_{L}^{q}\rangle$ are the ordinary moments (i.e., moments about zero) of order q for the variable S at resolutions λL and L, respectively. Equation 3.2 shows that the scale-invariant behavior of the variable S is characterized by the log-log linear relationship between scale ratio λ and statistical moment of order q, having slope τ. The scale exponent τ may vary with the moment order q, and characterize the scale-invariant behavior of the variable S. If the relationship of τ and q is linear, then the variable S has simple scaling (or monofractal) behavior. A non-linear relationship indicates that variable S exhibits multiscaling (or multifractal) behavior (*Schertzer & Lovejoy*, 1987).

Figure 3.2 illustrates the procedure adopted to estimate TWSA at successive coarser resolutions for each month. The 0.25° TWSA was upscaled step by step to the coarse resolution

of 4°. Upscaling was performed by combining and arithmetically averaging 2 number of pixels in each north-south and east-west directions. At each resolution, moments of orders q = 0, 0.5, 1.0, 1.5, 2.0, 2.5, 3.0, 3.5, and 4.0 were estimated.

$$\langle S_R^q \rangle = \frac{\sum_{i=1}^{N_R} (S_i)^q}{N_R} \qquad 3.3$$

where R is the resolution, $\langle S_R^q \rangle$ is the q^{th} moment of TWSA at resolution R, i is the pixel, and N_R is the total number of TWSA pixels at resolution R. At the resolution R, ensemble moment for moment order q; $\langle S_R^q \rangle$ was estimated by taking power q of the TWSA value of each pixel, summing them up and dividing by the total number of pixels (N_R) at that resolution.

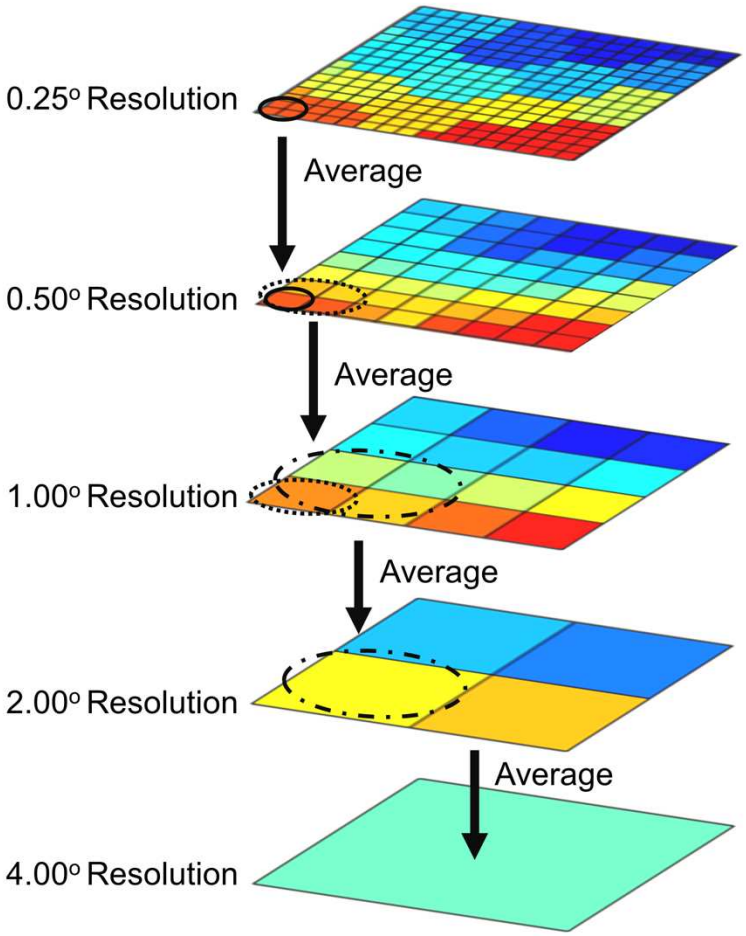

Figure 3.2. Upscaling of TWSA from 0.25° to 4°

Presence of log-log linear relationship of moments estimated from Equation 3.3 with TWSA resolutions at which these moments were calculated was tested (Figure 3.3a). R^2 and corresponding *p* value of log-log linear relationship for each moment order q of a particular month was estimated to establish whether relationship of moments and TWSA resolutions is log-log linear therefore, TWSA is scale-invariant. The negative of the slope of the log-log linear relationship at moment order q is the scaling exponent τ for that q. The τ-q relationship (e.g., Figure 3.3b) obtained from the analysis determines whether TWSA is monofractal or multifractal and forms the basis of stochastic downscaling of TWSA for a particular month.

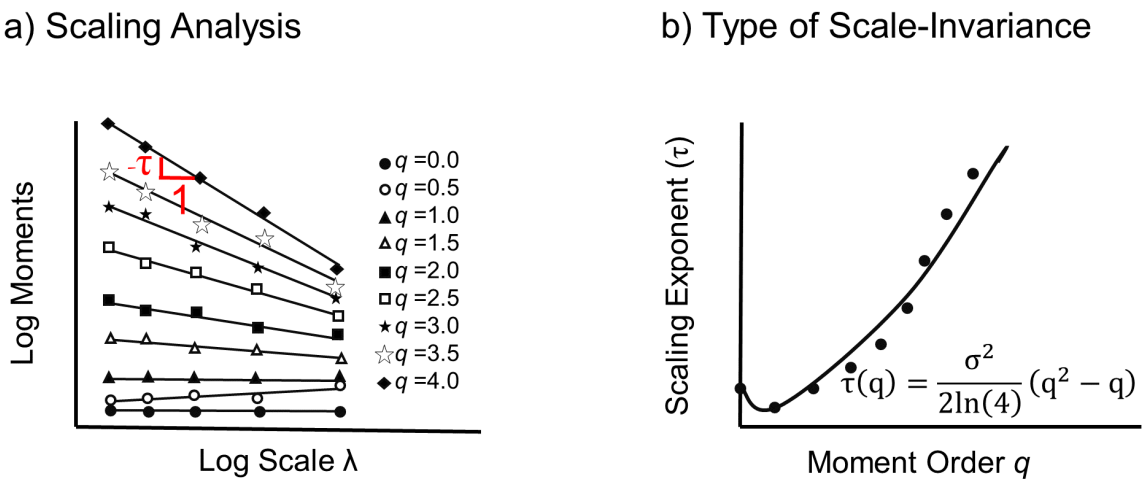

Figure 1.3. Schematics of Scale invariance analysis of TWSA

3.2.3.3 Stochastic downscaling of TWSA using MRCM

Number of MRCMs has been widely used to downscale scale-invariant hydroclimatic variables (e.g., *Deidda,* 2000; *Kang and Ramirez,* 2010; *Mascaro et al.,* 2010, 2019; *Posadas et al.,* 2015). For two dimensional datasets like GRACE, MRCM preserves the scale-invariant behavior while distributing the mass on successive regular subdivisions. Therefore, a pixel of length scale l_j is distributed into 4 subpixels at each disaggregration level (termed as cascade level). Therefore, at n^{th} disaggregation level there are total of 4^n subpixels each with a scaling ratio of $\lambda_n = l_n/l_0 = 4^{-n/2}$; where l_n and l_0 are length scales at n^{th} cascade level and original large-scale field respectively. The schematics of MRCM application to downscale TWSA is shown in Figure 3.4. From hereafter j^{th} subpixel at n^{th} cascade level will be denoted as Δ_n^j, where j is 1 to 4^n.

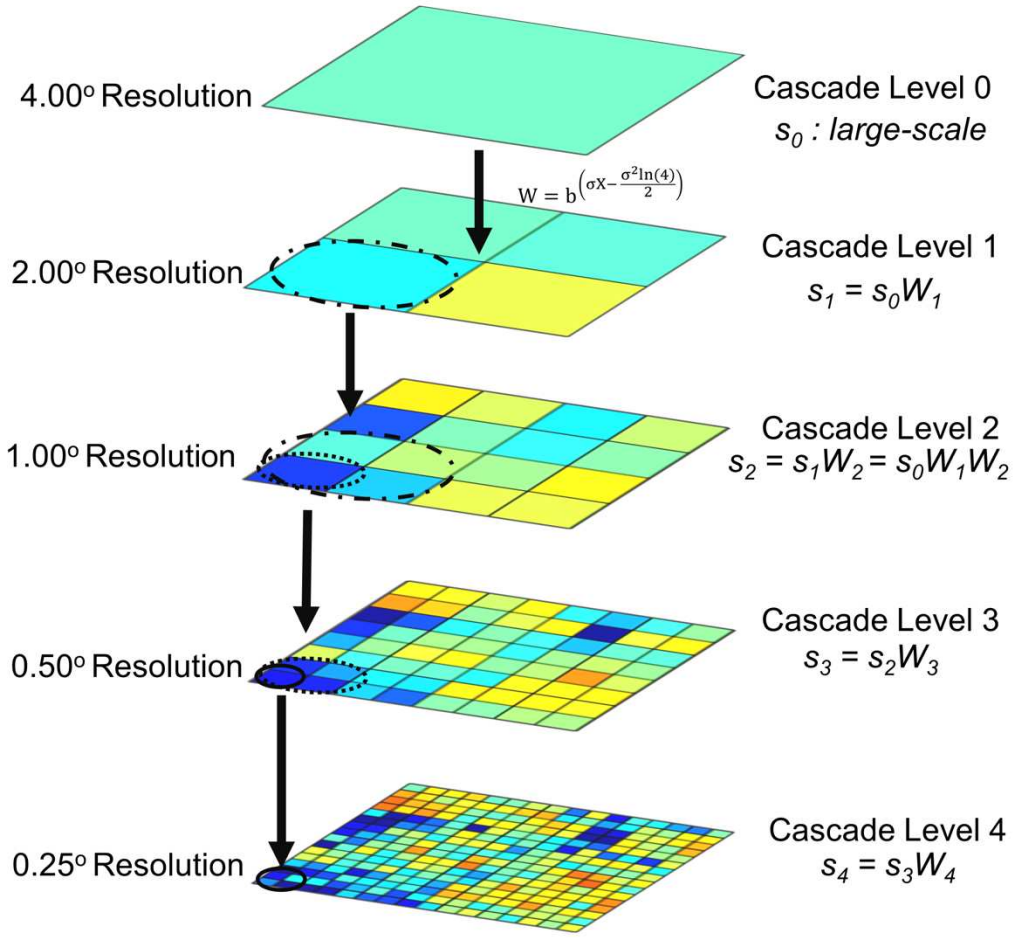

Figure 3.4. Schematics of stochastic downscaling of TWSA

Let us take $s_0 = s(\Delta_0)[L]$ be the initial single TWSA pixel at largest scale level (i.e., cascade level 0). Upon applying MRCM for disaggregation of s_0 at level 1, there will be 4 pixels with downscaled value of pixel $s(\Delta_0^j)$; where $j = 1,\ldots,4$; estimated as $s_1 = s_0 W_1(j)$, where W_s are independent and identically distributed random variables termed as cascade generators. At 2nd cascade level, each pixel from 1st level is downscaled in a similar way i.e., $s(\Delta_2^j) = s_1 W_2(j) = s_0 W_1(j) W_2(j)$. From this MRCM can be generalized as follows:

$$s(\Delta_n^j) = s_0 \prod_{k=1}^{n} W_k(j)\,; \qquad j = 1,\ldots\ldots,4^n \tag{3.4}$$

where $s(\Delta_n^j)$ is the downscaled TWSA of j^{th} pixel at n^{th} cascade level, and k is the cascade level. Equation 4 shows that TWSA for the pixel j at the n^{th} cascade level (i.e., $s(\Delta_n^j)$) is a cumulative product of large-scale s (i.e., s_0) and so-called cascade generators (W_s) for cascade levels 1 to n. In order to conserve the mass in equation 4 the distribution of W needs to be non-negative with $\langle W \rangle = 1$. This ensures that average TWSA of 4^n pixels at the n^{th} cascade equals to the initial large-scale single pixel s_0. Log of the q^{th} ensemble moment of the random cascade of equation 3.4 is as follows (e.g., *Over and Gupta,* 1996):

$$\log_4\langle s_n(q)\rangle = d(\log_4\langle W^q\rangle - (q-1))\log_4{\lambda_n}^{-1} + q\log_4({s_0}{l_0}^d) \qquad 3.5$$

where $\langle s_n(q)\rangle$ is the q^{th} ensemble moment of downscaled TWSA. Equation 5 shows that there is a linear relationship between the log of $\langle s_n(q)\rangle$ and the log of the inverse of the scaling ratio λ_n. Therefore, the MRCM satisfies the condition of statistical scale invariance as described in the equation 3.1. The so-called τ function is slope of the linear relationship of equation 5 and have a mathematical form:

$$\tau(q) = d(\log_4\langle W^q\rangle - (q-1)) \qquad 3.6$$

The parameters of the cascade generator W are based on the $\tau - q$ relationship developed following Equation 3.2 and the theoretical functional form describing the relationship. The theoretical functional form of the relationship is determined by the random cascade generator that reproduces statistical properties of TWSA field. To this end, number of random cascade generators have been used to stochastically downscale hydroclimatic variables including widely accepted and used i) lognormal, ii) beta-lognormal, and iii) log-Poisson cascade generators (e.g., see *Deidda,* 2000; *Gupta and Waymire*, 1993; *Over and Gupta,* 1996). Among

these, lognormal is the simplest and is characterized by one parameter as opposed to other two cascade generators where each of them is characterized by two parameters. Beta-lognormal cascade generator is more suited to model highly intermittent random fields such as precipitation which necessarily contains non-rainy or dry (i.e., zero value) areas (*Over and Gupta,* 1996). However, zeros in transformed TWSA fields does not mean zero storage areas i.e., no area is fully dry (or out of water). Log-Poisson cascade generator is suited to model intermittent precipitation and soil moisture fields (*Deidda,* 2000; *Mascaro et al.,* 2010; 2019). For stochastic downscaling of TWSA using MRCM, lognormal cascade generator owing to its simple and parsimonious structure, and ability to model heterogeneous and intermittent fields, emerges as a suitable choice. Lognormal cascade generator takes the following mathematical form:

$$\mathrm{W} = 4^{\sigma \mathrm{X}} \tag{3.7}$$

where σ is the standard deviation corresponding to the variance of $\ln(\mathrm{W})$ and is the measure of the non-linearity of scaling exponents and degree of multifractality (*Bacry et al.,* 2013). And X is the randomly generated number sampled from standard normal distribution with zero mean and standard deviation of unity. Under the condition $\langle \mathrm{W} \rangle = 1$ the lognormal cascade generator takes the form (*Gupta and Waymire*, 1993)

$$\mathrm{W} = 4^{\sigma \mathrm{X} - \frac{\sigma^2 \ln(4)}{2}} \tag{3.8}$$

And the $\tau - \mathrm{q}$ relationship for the lognormal generator cascade of equation 8 is (e.g., *Tchiguirinskaia et al.,* 2000):

$$\tau(q) = \frac{\sigma^2}{2\ln(4)}(q^2 - q) \quad 3.9$$

Equation 3.8 shows that the stochastic modeling of TWSA using a lognormal MRCM requires σ^2 which is estimated by minimizing the sum of squared errors between Equation 3.9 and empirical $\tau - q$ relationship.

The downscaling of the large-scale (4°) transformed TWSA was carried out for each month of the study period. For each month parameter σ^2 was estimated by computing empirical moments for $q = 0, 0.5, 1, 1.5, 2, 2.5, 3, 3.5, \text{and } 4$ at scales 0.25° to 4° (see Figure 3.2 and Equation 3.3), empirical scaling exponents for each q were derived as the negative of the slope of log-log scale and empirical moments, and then fitting a least-square regression to empirical scaling exponents and q to $\tau - q$ relationship for lognormal cascade generator (Equation 3.9) to estimate σ^2. Using its estimated σ^2, the large-scale transformed TWSA for a particular month was downscaled at the resolution of 0.0625° using the lognormal MRCM (Figure 3.4, and Equation 3.8). One thousand realizations for each month were carried to perform stochastic downscaling of large-scale transformed TWSA. In order to compare with GRACE, GRACE-FO and GPS TWSA, each realization of fine resolution transformed TWSA was back-transformed by subtracting the same numbers which were added during the process of transformation.

3.3 Results

Table 3.1 shows mean (i.e., large-scale), minimum and maximum GRACE, GRACE-FO and GPS TWSA and transformed TWSA, standard deviation of TWSA and coefficient of variation (CV) for dry, average, and wet months. These sample months are defined as: i) dry month: month

whose mean GRACE, GRACE-FO or GPS TWSA is minimum among all the months, ii) average month: whose mean GRACE, GRACE-FO or GPS TWSA is closest to the long-term mean of large-scale GRACE, GRACE-FO or GPS TWSA for the study period, and iii) wet month: month whose mean GRACE, GRACE-FO or GPS TWSA is maximum among all the original TWSA months. For California region, these sample months were taken from the common period of GRACE and GPS i.e., January 2006 to July 2021.

Table 3.1. Mean, minimum and maximum GRACE, GRACE-FO and GPS TWSA and transformed TWSA. Values in bracket shows mean, minimum and maximum transformed TWSA. Table also shows the standard deviation and coefficient of variation (CV) of transformed GRACE, GRACE-FO, and GPS TWSA

Region		**Dry Month**	**Average Month**	**Wet Month**
Amazon	Mean TWSA (mm)	-45.6 (35.2)	6.3 (16.2)	80.3 (114.1)
	Min. TWSA (mm)	-73.4 (7.4)	-9.2 (0.9)	30.7(64.5)
	Max. TWSA (mm)	-16.2 (64.6)	35.4 (45.5)	129.3 (163.1)
	St. Dev. (mm)	15.0	9.1	28.6
	CV	0.43	0.56	0.25
Sindh	Mean TWSA (mm)	-12.1 (10.6)	-1.3 (3.8)	8.2 (12.4)
	Min. TWSA (mm)	-20.5 (2.1)	-4.7 (0.5)	3.8 (8.1)
	Max. TWSA (mm)	-5.1 (17.6)	1.2 (6.3)	11.9 (16.2)
	St. Dev. (mm)	3.6	0.9	1.7
	CV	0.34	0.24	0.14
California	Mean TWSA (mm)	-23.7 (15.5)	-6.0 (10.8)	8.5 (12.8)
	Min. TWSA (mm)	-35.7 (3.6)	-15.3 (1.5)	3.9 (8.3)
	Max. TWSA (mm)	-10.8 (28.4)	1.6 (18.4)	16.3 (20.6)
	St. Dev. (mm)	7.2	4.8	3.8
	CV	0.46	0.44	0.29
California - GPS	Mean TWSA (mm)	-233.7 (588.3)	47.1 (246.4)	468.8 (663.6)
	Min. TWSA (mm)	-747.4 (74.7)	-181.2 (18.2)	-177.1 (17.7)
	Max. TWSA (mm)	319.6 (1417.5)	449.8 (649.3)	1224.4 (1419.2)
	St. Dev. (mm)	245.5	171.5	393.7
	CV	0.42	0.69	0.59

Table 3.1 shows that GRACE, GRACE-FO and GPS mean TWSA for sample dry months is negative whereas mean TWSA for sample wet months are positive. For the sample average months, mean may be negative or positive. GRACE and GRACE-FO minimum and maximum TWSA for sample dry months are all negative and for sample wet months all TWSA are positive. For GPS TWSA sample dry and wet months have minimum TWSA is negative and maximum TWSA is positive. For sample average months mean TWSA can be negative or positive, minimum TWSA is negative and maximum TWSA is positive. Transformed mean, minimum and maximum TWSA are always positive. Transformed mean TWSA for average months are always smaller than dry and wet months. Table 3.1 also shows that for a particular region the standard deviation of GRACE, GRACE-FO and GPS TWSA for the sample months are generally smallest for the average month. CV of transformed TWSA is largest for sample average months for Amazon and GPS TWSA of California, and for sample dry months for Sindh and GRACE TWSA for California. The CV of sample dry and average months of transformed GRACE and GRACE-FO TWSA for California are similar.

Figure 3.5 shows the dry, average, and wet months transformed TWSA for three study regions. Transformed TWSA for Amazon region (Figure 3.5a-3.5c) shows that average month has smaller TWSA values as compared to dry and wet month TWSA values. Therefore, transformed mean TWSA for average month is lower than those of dry and wet months (see Table 3.1). This resulted due to the transformation of original TWSA to nonnegative numbers. The transformation for a particular month is based on the minimum GRACE, GRACE-FO or GPS TWSA of that month. Figure 3.5(a-c) also shows that for Amazon region average month transformed TWSA has the smallest range (hence lowest standard deviation; see Table 1) and

wet month has the largest range (highest standard deviation; Table 3.1). Figure 3.5(d-f) shows that for Sindh region, range of transformed TWSA for dry month is largest and average month has the smallest range. Figure 3.5(g-i) shows that, for California, dry month transformed TWSA has the largest range, whereas average and wet month have similar ranges. Figure 3.5(j-l) shows wet month transformed GPS TWSA for California has the largest range, whereas range of TWSA for other two months are similar.

Figure 3.5(a-i) shows that among three regions transformed TWSA for Amazon has highest variability, whereas Sindh has least variability. Figure 3.5(g-l) shows that for California, transformed GPS TWSA has much more variability than the transformed GRACE and GRACE-FO TWSA. TWSA estimates from GRACE (and GRACE-FO) and GPS are based on different processes (i.e., gravitational changes and vertical movement of earth surface, respectively), and the time span for long-term mean to compute anomalies is different for GRACE and GRACE-FO TWSA and GPS TWSA. However, when compared on large scales for Sacramento and San Joaquin river basins in California, GRACE TWSA rescaled with observed water fluxes, showed similar trends and variability in time as of GPS TWSA (*Ukasha et al*., 2022b).

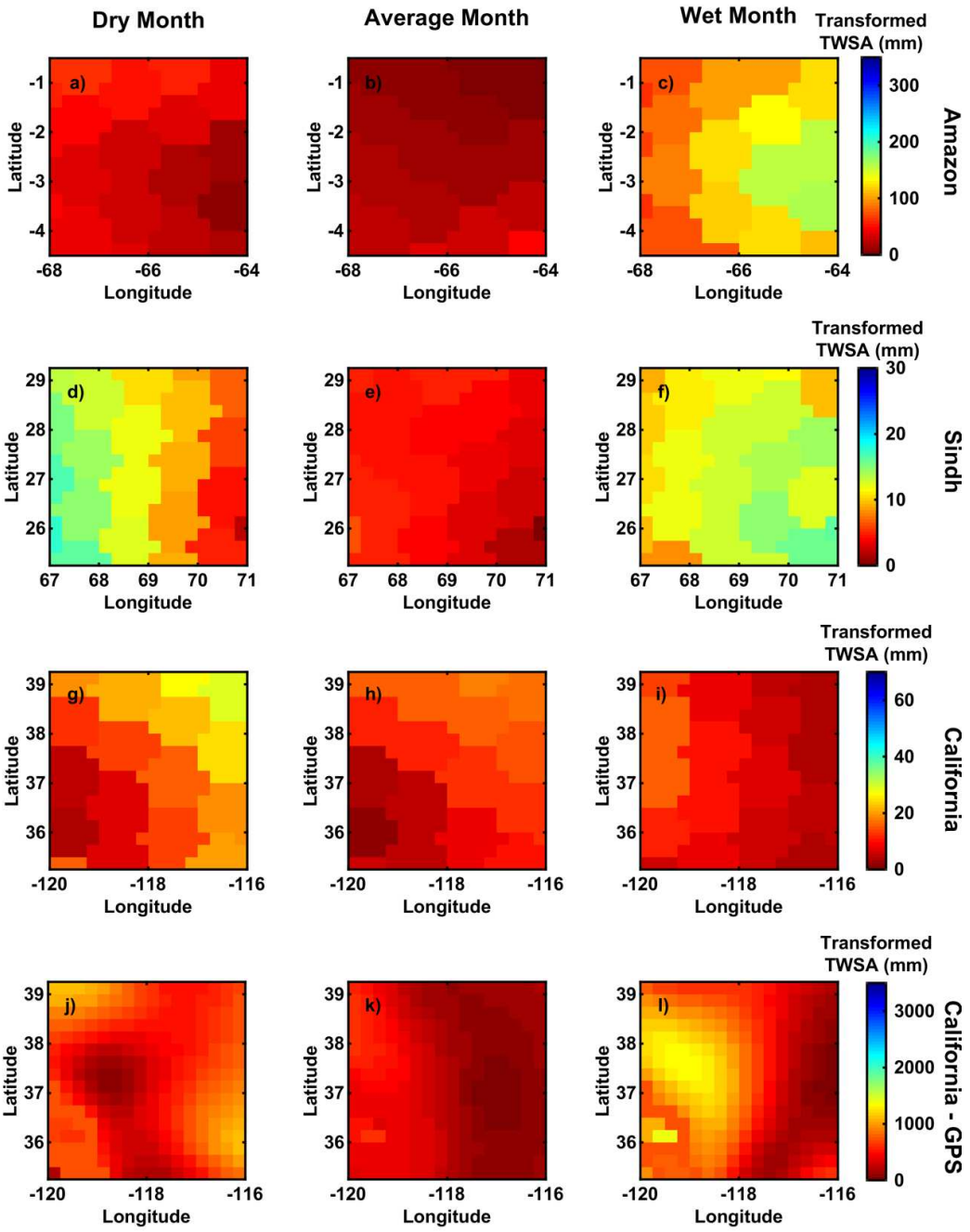

Figure 3.5. a, b, c) Gridded transformed GRACE TWSA for dry, average, and wet months of Amazon, respectively; d, e, f) gridded transformed GRACE TWSA for dry, average, and wet months of Sindh, respectively; g, h, i) gridded transformed GRACE TWSA for dry, average, and wet months of California, respectively; and j, k, l) gridded transformed GPS TWSA for dry, average, and wet months of California, respectively.

Figure 3.6 shows the log-log relationship of TWSA resolution and empirical moments of transformed TWSA estimated following Equation 3.3 for the sample months. Figure 3.6 shows

that for a particular region, the empirical moments from wet month TWSA are generally higher than those for dry and average months. Wet months have high value TWSA pixels as compared to dry and average months (see Figure 3.5) and therefore, resulted in higher empirical moments. Moreover, Figure 6 also shows that generally higher empirical moments are related to more spatial variability (also see Table 3.1 and Figure 3.5). For example, for Amazon wet month transformed TWSA has the highest standard deviation and empirical moments and average month has the smallest standard deviation and empirical moments. Similarly, when empirical moments of different regions are compared, empirical moments and standard deviation of California from GPS TWSA are highest, followed by Amazon region, California from GRACE and GRACE-FO TWSA, and finally Sindh region has the lowest standard deviation and empirical moments.

Figure 3.6 also shows that for the three months and across the regions, the log-log ensemble moments and TWSA resolution relationship is fairly linear. Table 3.2 shows the mean, maximum and minimum R^2 across all moment orders for the three regions. Table 3.2 also shows the maximum *p* value (this is associated with minimum R^2). The mean R^2 for these linear relationships is approximately 0.8 whereas minimum R^2 values are above 0.6 and maximum *p* values is slightly above 0.1. Lower R^2 values are generally associated with empirical moments at higher moment order (not shown here). This indicates that generally log-log linear relationships are statistically significant ($p < 0.1$). This suggests that for the study regions GRACE, GRACE-FO and GPS TWSA exhibits property of statistical scale-invariance as hypothesized.

Table 3.2. Mean, minimum and maximum R^2 and maximum p values of log-log linear relationships of empirical moments and TWSA resolutions. Maximum p value corresponds to minimum R^2 of the region.

Region	**Mean R^2**	**Maximum R^2**	**Minimum R^2**	**Maximum *p* value**
Amazon	0.79	0.99	0.64	0.11
Sindh	0.82	0.99	0.64	0.11
California	0.77	0.97	0.62	0.12
California - GPS	0.79	0.97	0.63	0.11

Figure 3.7 shows the empirical scaling exponents τ (negative of the slopes of log-log relationships in Figure 3.6) as the function of moment orders q as well as the theoretical form of $\tau - q$ relationship from lognormal MRCM (Equation 3.9). For the sample dry, average, and wet months; transformed TWSA have non-linear $\tau - q$ relationships suggesting that for all cases TWSA has multifractal behavior. The theoretical $\tau - q$ function of Equation 3.9 seems to capture the empirical multifractal behavior for all cases. This supports the use of lognormal MRCM for spatial downscaling of transformed TWSA.

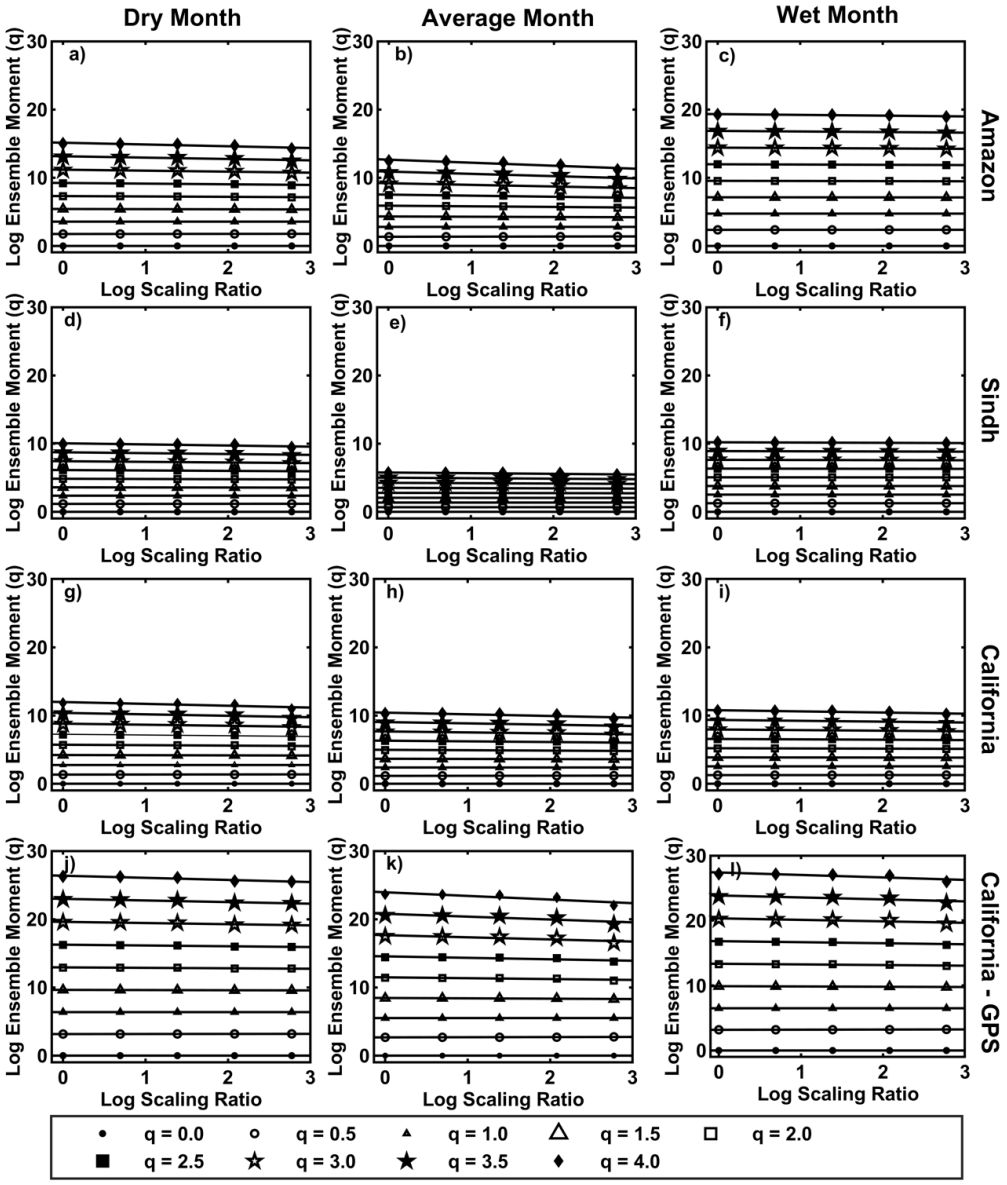

Figure 3.6. Log moment - log TWSA resolution plots for a, b, c) dry, average, and wet month transformed TWSA of Amazon from GRACE and GRACE-FO, respectively; d, e, f) dry, average, and wet month transformed TWSA of Sindh from GRACE and GRACE-FO, respectively; g, h, i) dry, average, and wet month transformed TWSA of California from GRACE and GRACE-FO, respectively; and j, k, l) dry, average, and wet month transformed TWSA of California from GPS, respectively.

Figure 3.7 shows that for a particular region, the parameter σ^2 is different for each sample month. For Amazon region (Figure 3.7a), average month has the highest and wet month has the lowest σ^2, which can be seen from higher values of scaling exponent and more

curvature of $\tau - q$ relationship during average month. This suggests that for Amazon, average month has higher degree of multifractality as compared to those for dry and wet months. Figure 3.7b shows that for Sindh, dry month has highest and wet month has lowest degree of multifractality. Figure 3.7c shows that for California region, dry and average months have somewhat similar and higher degree of multifractality than wet month. Figure 3.7d shows that transformed GPS TWSA for California showed highest and lowest degree of multifractality in average and dry months, respectively. When degree of multifractality or σ^2 of a particular region is compared to the CV of that region (see Table 3.1), higher σ^2 corresponds to higher CV and vice versa. However, same is not true when standard deviations are compared. This indicates that degree of multifractality of a particular month is function of both transformed mean TWSA and its standard deviation. Higher degree of multifractality results from higher rate of increase in scaling exponent (i.e., negative of the slope of log-log linear relationship of empirical moments and TWSA resolution) with respect to the moment order. Empirical moments at higher moment orders decreases at higher rates (i.e., large negative slope) when there is more variability in the transformed TWSA field (i.e., higher CV). Transformed TWSA at successive coarser resolutions have lower variability such that maximum transformed TWSA decreases and minimum transformed TWSA increases at every step of upscaling. At higher moment orders, empirical moments of large values of transformed TWSA decreases more rapidly with coarser resolution as compared to lower moment orders. And empirical moments of small values of transformed TWSA increases more rapidly with coarser resolution at lower moment orders. Therefore, in a highly variable transformed TWSA field large reductions in variability at successive coarser resolutions results in smaller values of scaling exponents at

lower moment orders and in larger values of scaling exponents at higher moment orders. This results in larger degree of multifractality.

Figure 3.7 also shows that, σ^2 is different for a particular sample month when different regions are compared. Region having larger CVs of transformed GRACE and GRACE-FO TWSA has higher degree of multifractality. For example, from Figure 3.5 and Table 3.1 Amazon which has largest variability, also showed highest degree of multifractality, whereas Sindh having smallest variability showed least degree of multifractality. Similarly, for California region, transformed GRACE and GRACE-FO TWSA having lower variability has lesser degree of multifractality than that from transformed GPS TWSA having larger variability. We argue that differences in degree of multifractality of regions occurs due to different climatic, geologic, and physiographic characteristics of the regions. Amazon region high recharge aquifer where surface that is seasonally flooded, the aquifer remains somewhat saturated throughout the year and therefore TWSA variations partially results due to flooding (*Pokhrel et al.,* 2013). This results in large variations specifically during sample wet month. Sindh region is essentially semi-arid to arid with little annual rainfall, it is poorly drained, waterlogged and saline (*Lytton et al.,* 2021). In addition, there is little usage of groundwater usage in the region. Therefore, large variations in TWSA is not expected and hence lower degree of multifractality. Region around California is generally semi-arid to arid, however, consists of varying climatic conditions. Moreover, part of the region is containing southern portion of highly pumped and depleting central valley aquifer (e.g., *Alam et al.,* 2021). Therefore, GRACE and GRACE-FO transformed TWSA showed more variations then Sindh region. However, GRACE and GRACE-FO transformed TWSA showed lesser variations then wetter Amazon region.

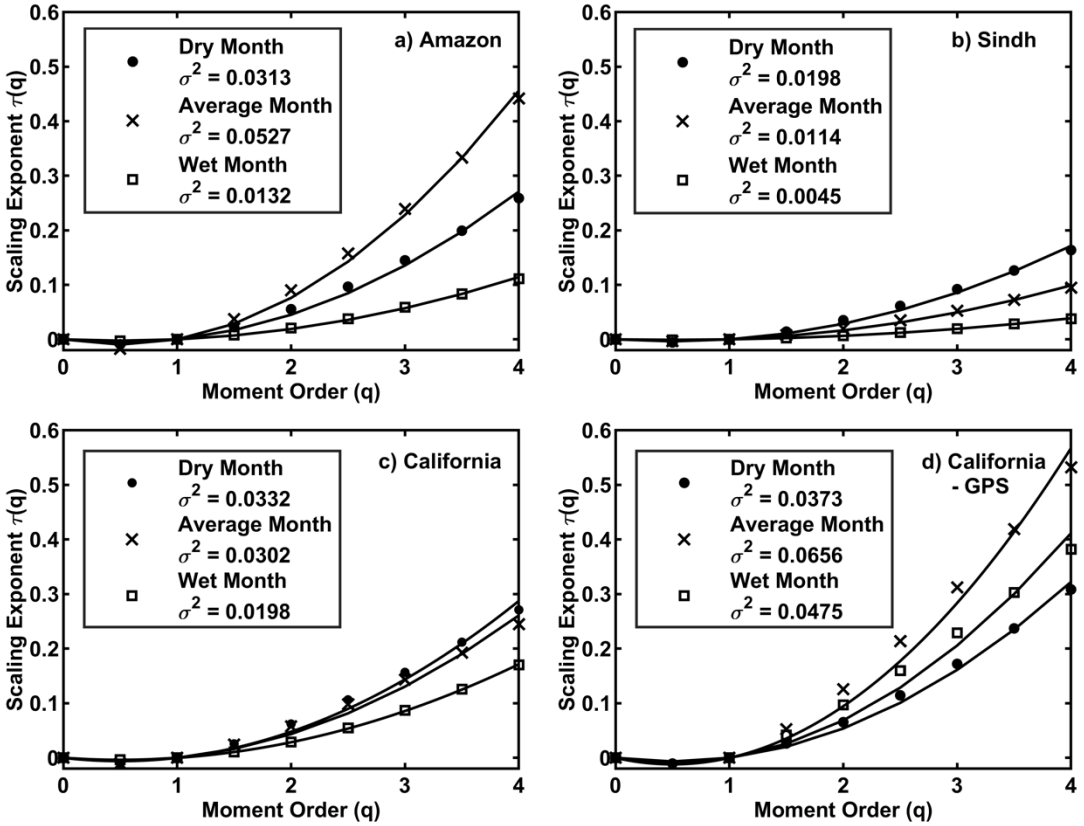

Figure 3.7. Scaling exponent and moment order relationships for dry, average, and wet months for a) Amazon; b) Sindh; c) California; and d) California from transformed GPS TWSA

Figure 3.8 shows the one of the realizations (out of one thousand) of fine resolution (0.0625^o) transformed TWSA for sample months produced by lognormal MRCM. Figure shows those fine resolution realizations which have σ^2 similar to those from GRACE, GRACE-FO and GPS transformed TWSA (at 0.25^o; Figure 3.7). When compared with the GRACE, GRACE-FO and GPS transformed TWSA (at 0.25^o; Figure 3.5), all of the sample months from all regions fine resolution transformed TWSA showed larger range of transformed TWSA values. This is expected and intended outcome of the stochastic downscaling. Furthermore, for a particular region, variability structure of the fine resolution transformed TWSA of sample month follows the standard deviation of transformed GRACE, GRACE-FO and GPS transformed TWSA. For example, GRACE and GRACE-FO transformed TWSA for Amazon has highest standard deviation

for wet month and lowest for average month (see Table 3.1 and Figure 3.5a-c). The fine resolution transformed TWSA for Amazon shows the same variability structure (Figure 3.8a-c).

Figure 3.8 also shows that some of the sample months have few pixels with significantly larger values of transformed TWSA when compared with the corresponding transformed GRACE, GRACE-FO and GPS TWSA (see Figure 3.5). For example, wet month of Amazon, dry and wet months of Sindh, dry month of California, and dry and wet months of California when considering fine resolution of transformed mean TWSA of GPS. These months have higher standard deviations (Table 3.1) and have produced larger range of fine resolution transformed TWSA values. Capturing such large transformed TWSA values may be of particular interest to some applications. For example, Sindh is a waterlogged region and fine resolution transformed TWSA have more and higher extremes in sample dry month as compared to wet month. This may indicate the probability of the presence of heavily waterlogged spaces in the region even during extreme dry months. Deterministic downscaling procedures may miss these features at finer resolutions.

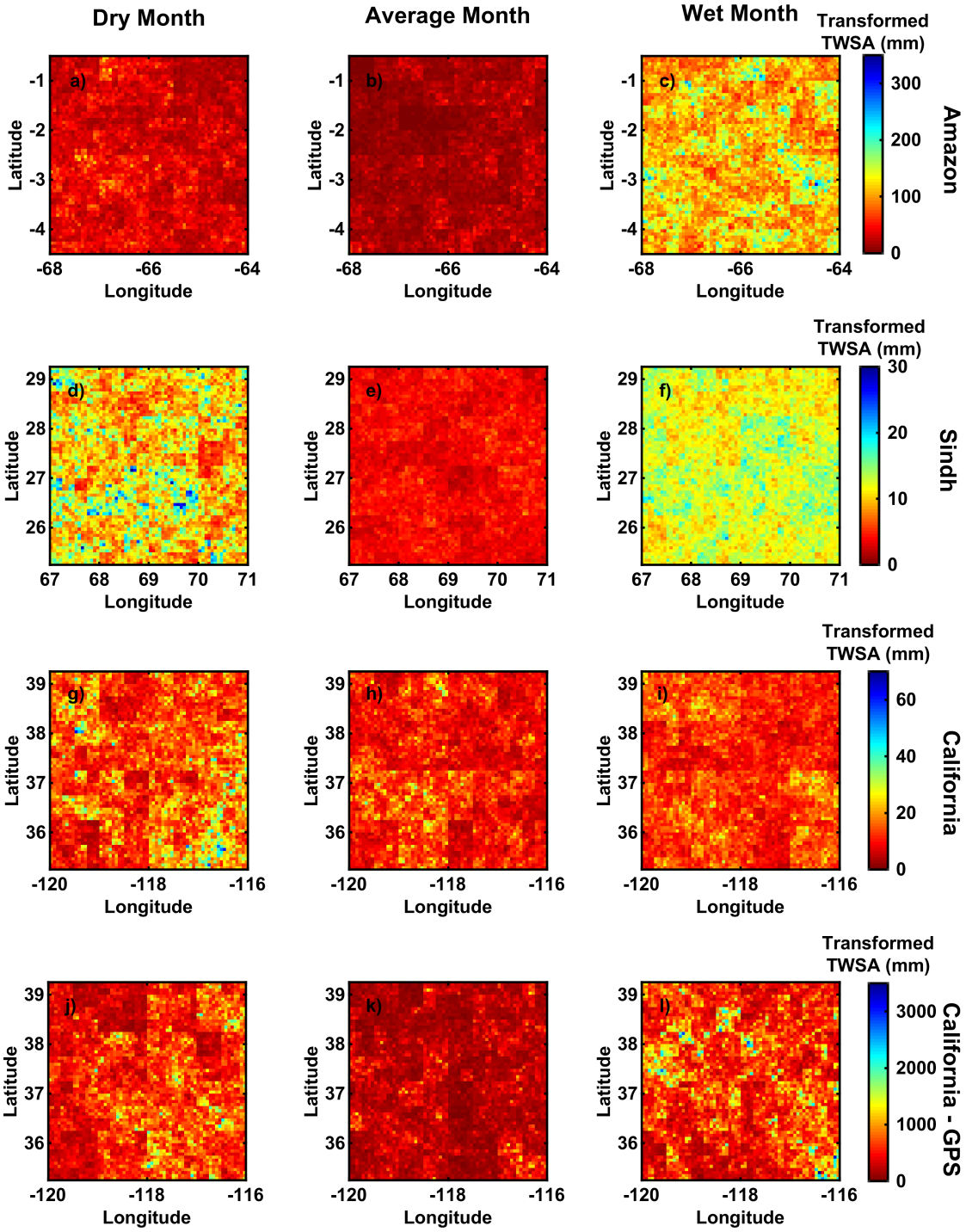

Figure 3.8. MRCM realization of fine resolution transformed TWSA; a-c) Amazon; d-f) Sindh; g-i) California; and j-l) California from transformed GPS TWSA

Figure 3.9 shows the $\tau - q$ relationships for fine resolution transformed TWSA produced by one thousand realizations of lognormal MRCM. Given the stochastic nature of downscaling procedure, each realization resulted in a different $\tau - q$ relationship. Due to the stochastic nature of MRCM, $\tau - q$ relationships from realizations of fine resolution transformed TWSA results in a large scatter. Small spatial extent of analysis and downscaling resulted in large scatter. Months with higher degree of multifractality (see Figure 3.7) has a wide scatter than those with lower degree of multifractality. This means that for highly variable (having large CV) TWSA fields, lognormal MRCM produces realizations with large range of spatial variabilities. Figure 3.9 also shows that for each sample month and all regions, the empirical $\tau - q$ relationships from GRACE, GRACE-FO and GPS transformed TWSA fall within the scatter of $\tau - q$ relationships from realizations of fine resolution transformed TWSA. However, in all cases, majority of realizations produced $\tau - q$ relationships having larger degree of multifractality, which is typical of lognormal cascade model (e.g., *Tchiguirinskaia et al.,* 2000).

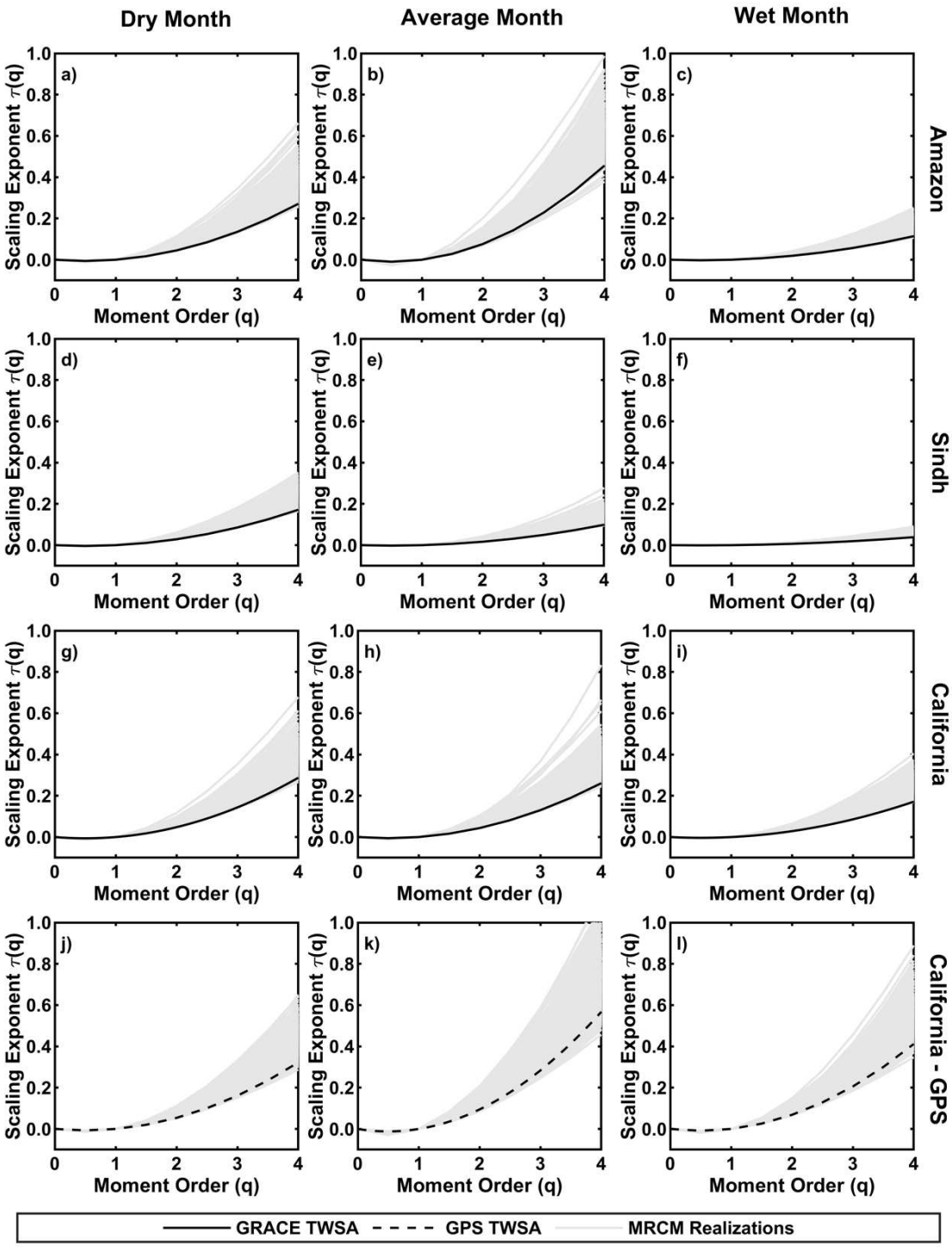

Figure 3.9. Comparison of empirical $\tau - q$ relationships of transformed GRACE, GRACE-FO and GPS TWSA (at 0.25°) with fine resolution (0.0625°) transformed TWSA produced by MRCM; a-c) Amazon; d-f) Sindh; g-i) California; and j-l) California from transformed GPS TWSA

Figure 3.10 compares the empirical cumulative distribution functions of the GRACE, GRACE-FO and GPS TWSA (at 0.25^o) with cumulative distribution functions of fine resolution TWSA (0.0625^o) produced by MRCM. For each sample month and all regions the empirical cumulative distribution functions of GRACE, GRACE-FO and GPS TWSA (at 0.25^o) generally falls within the scatter of realizations of fine resolution TWSA. However, Figure 3.10 shows that all realizations have much larger TWSA values at the end of the cumulative distribution functions. This indicates that fine resolution TWSA have larger range than those of GRACE, GRACE-FO and GPS TWSA at 0.25^o. These results suggest that GRACE, GRACE-FO and GPS TWSA may adequately capture very dry conditions, however, locally they may miss very wet conditions. This has important implications for assessing probability of waterlogging and local flood risks. Figure 3.8d has shown the same for Sindh region, where very wet pixels were present during the sample dry month.

Studies on the stochastic downscaling of hydroclimatic variables have shown that parameters of the random cascade generator depend on the large-scale (i.e., mean) value of hydroclimatic variable (e.g., *Over,* 1995). In this study, lognormal MRCM is characterized by two parameters; i) minimum TWSA at 0.25^o, and ii) σ^2. The left side of Figure 11 shows the relationship of large-scale monthly GRACE, GRACE-FO and GPS TWSA with monthly minimum GRACE, GRACE-FO and GPS TWSA and monthly σ^2. GRACE, GRACE-FO and GPS TWSA minimum TWSA showed an increasing relationship with the large-scale TWSA, which is expected. For Amazon the relationship is non-linear, whereas Sindh and California regions have a more of a linear relationship. For California, minimum and large-scale GPS TWSA has a non-linear correlation. Figure 3.11 also shows that for Amazon, the relationship of minimum and large-

scale TWSA in months when large-scale TWSA is around zero is somewhat parallel to 1:1 line and deviates from this pattern during drier and wetter months. Sindh has this pattern in average and wetter months. California shows this pattern almost across all months, however, relationship for GPS data of California has this pattern during dry months only. This implies that when minimum and large-scale TWSA relationships are parallel to 1:1 line, TWSA patterns generally remains the same and only shifted their means.

Figure 3.11 also shows the dependence of σ^2 for the three regions on the large-scale GRACE, GRACE-FO and GPS TWSA. All of the three regions have lower σ^2 during dry and wet months and higher σ^2 in the months having large-scale TWSA near the long-term mean TWSA. This implies that generally average months have higher degree of multifractality as compared to dry and wet months. For GPS data in California, σ^2 increases with large-scale TWSA.

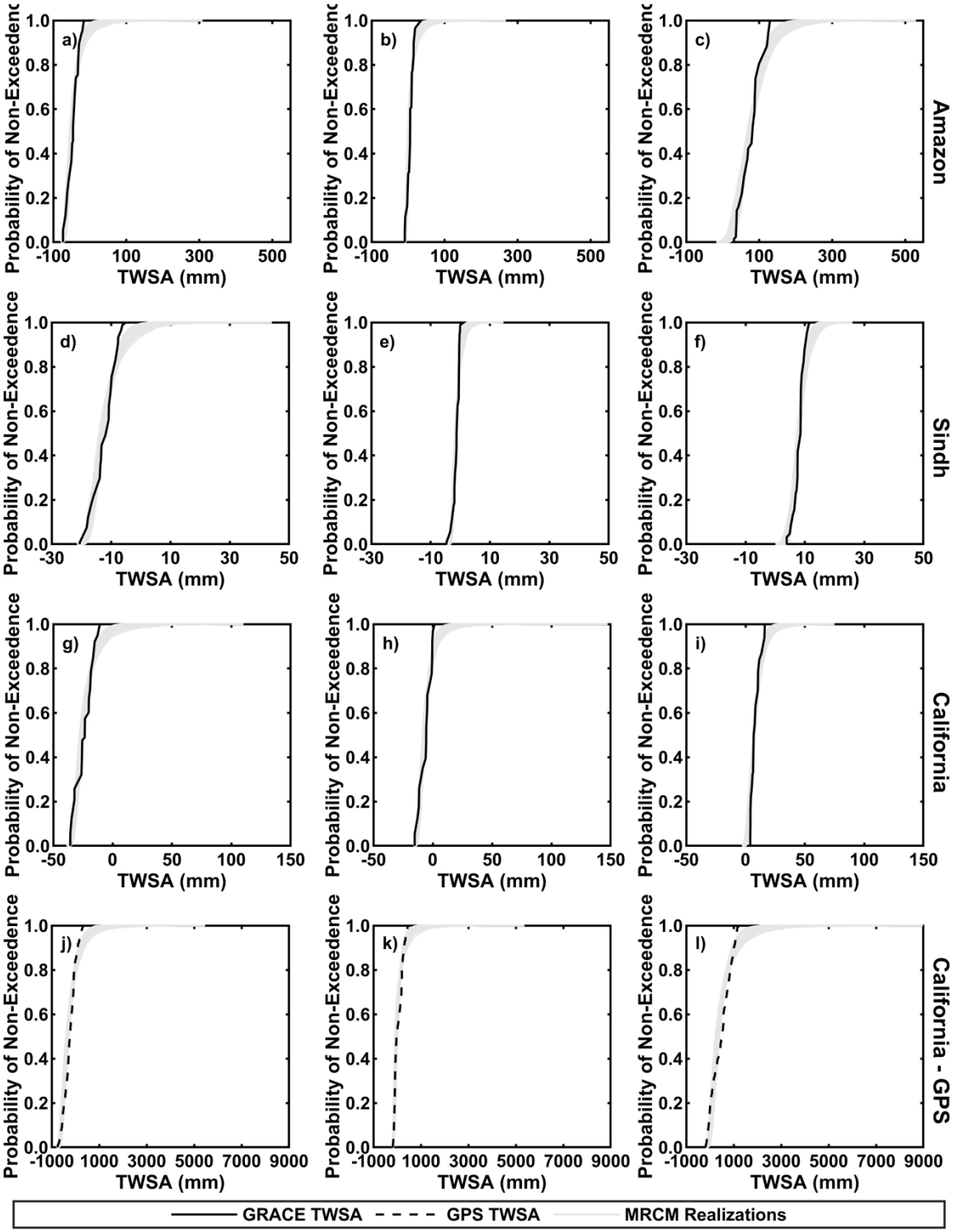

Figure 3.10. Comparison of empirical cumulative distribution functions of GRACE, GRACE-FO and GPS TWSA (at 0.25^{o}) with cumulative density functions of fine resolution TWSA (at 0.0625^{o}) produced by MRCM; a-c) Amazon; d-f) Sindh; g-i) California; and j-l) California from GPS TWSA

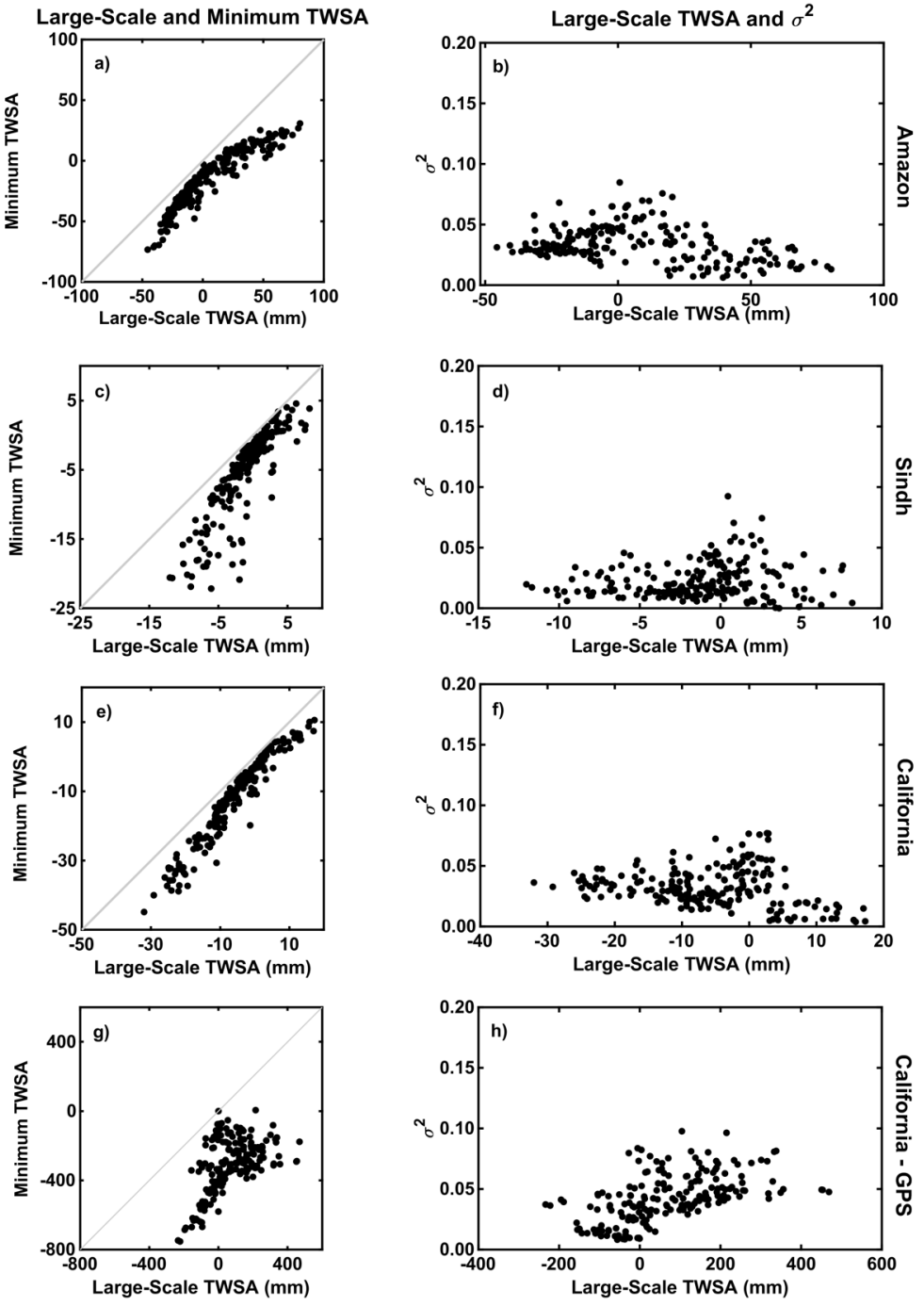

Figure 3.11. Dependence of MRCM parameters i) minimum TWSA (left panel), and ii) σ^2 (right panel) with large-scale GRACE, GRACE-FO and GPS TWSA

3.4 Discussion

Analysis of scale-invariance of GRACE, GRACE-FO and GPS TWSA for three regions shows that TWSA exhibit multifractal behavior in spatial domain. Hydroclimatic variables such as precipitation and soil moisture has also shown to be multifractal in nature. The degree of multifractality of TWSA is characterized by its spatial variability with respect to mean TWSA. In addition to spatial variability, intermittency of precipitation fields contributes to its multifractal behavior (e.g., *Over and Gupta,* 1996). Intermittency refers to the presence of simultaneous non-rainy and rainy pixels in a region. Therefore, stochastic downscaling of precipitation is generally carried out using a β-lognormal model which is a sophisticated version of lognormal MRCM. In this case an additional parameter β is introduced to capture intermittent behavior of precipitation. β-lognormal MRCM reproduces the non-rainy pixels and the scale-invariant statistical properties of precipitation (e.g., *Kang and Ramirez,* 2010; *Posadas et al.,* 2015). MRCM based on two parameter log-Poisson random cascade generator have also been used to characterize and stochastically downscale multifractal precipitation fields (e.g., *Deidda,* 2000). Log-Poisson model is unable to produce non-rainy pixels, however, can produce pixels with values near zero. Therefore, log-Poisson model is better suited to characterize and downscale multifractal soil moisture fields (*Mascaro et al.,* 2010). *Neuhauser et al.* (2019) and *Verrier* (2020) using remotely sensed and *in-situ* observations demonstrated the multifractal behavior of soil moisture. *Mascaro et al.* (2010; 2019) showed that the intermittent (very dry; residual soil moisture) and multifractal nature of soil moisture can be adequately reproduced by log-Poisson MRCM.

Previous studies on downscaling TWSA primarily focused on determining small scale variations in TWSA without considering the statistical properties at fine resolutions (e.g., *Arshad et al.,* 2022; *Sun et al.,* 2022; *Yin et al.,* 2022). These methods aim to estimate local TWSA with accuracy, however, are unable to estimate the extreme TWSA values at fine resolutions that may not be adequately captured by coarse resolution. Stochastic downscaling of coarse resolution (4^{o}) TWSA performed in this study produced large TWSA values while approximately conserving the scale-invariant statistics at fine resolution (0.0625^{o}). This model, however, is unable to accurately estimate local TWSA at a specific location. The stochastic downscaling is more suitable to estimate the likelihood of a region being very wet or very dry at fine resolutions. Therefore, the power of such models lies in their application for assessment of flood or drought risks at local scales. Furthermore, in contrast to deterministic procedures that require other information to downscale TWSA, the stochastic downscaling model only used TWSA field to infer scaling features and parameters of the model.

The scope of the study was limited to test the hypothesis that if TWSA exhibits scale-invariant behavior and consequently applying a simpler MRCM to stochastically downscale TWSA. The findings of the study can potentially be extended to improve stochastic downscaling method. For example, simple transformation of TWSA was carried out in the study, more ways to transform TWSA may be explored. One parameter lognormal MRCM was applied to downscale TWSA at finer resolutions. More sophisticated MRCMs such as β -lognormal and log-Poisson may better explain the factors controlling degree of multifractality. Lognormal MRCM has the tendency to overestimate the degree of multifractality, to constrain this either very large domain needs to be studied or the MRCM framework needs to be modified. Bounded

lognormal cascades (e.g., *Menabde,* 1998) in which the parameter σ^2 decreases with level of cascade may be explored. Coupling the stochastic MRCM with deterministic models (dynamical or statistical) of downscaling is another potential research question to explore. This will add value to both deterministic and stochastic downscaling and may help in determining the location of extreme conditions at fine resolutions with accuracy. TWSA (both GRACE and GPS), in addition to low spatial resolution, also has low temporal resolution (i.e., monthly). Development of a framework for spatio-temporal stochastic downscaling of TWSA is also an avenue to consider. Figure 3.11 shows the dependency of parameters of lognormal MRCM on large-scale TWSA. These dependencies can be modeled as relationships by fitting appropriate statistical models. Therefore, provides an opportunity to directly downscale TWSA for other months without carrying out complete process of analyzing scale-invariance and estimating parameters.

3.5 Conclusions

This study used 0.25^o GRACE, GRACE-FO and GPS data for three climatically, geologically, and physiographically different regions to answer if TWSA is scale-invariant and what type of scale-invariant TWSA exhibits. Furthermore, stochastic downscaling to fine resolution (0.0625^o) was performed where parameters of the model was derived from the scaling features of TWSA at coarse resolutions. Scaling analysis and downscaling of TWSA was carried out for Central Amazon basin in Brazil, Sindh province in Pakistan, and California, U.S.A.

Analysis of scale-invariance was carried out for TWSA resolutions from 0.25^o to 4^o. Log-log linear relationship of empirical moments and TWSA resolution suggested that GRACE, GRACE-FO and GPS TWSA exhibits scale-invariant behavior. Furthermore, the non-linear relationship of

scaling exponents (derived from the slopes of log-log linear relationships of empirical moments and TWSA resolutions) with moment orders showed that TWSA is multifractal. Degree of multifractality (or non-linearity of scaling exponents) that essentially defines the scaling features was found to differ with region and in dry, average and wet months in a certain region. In addition, degree of multifractality for a particular region during a particular month was shown to depend on the mean and standard deviation of that month's TWSA field i.e., degree of multifractality was found to increase with the coefficient of variation.

A lognormal multiplicative random cascade model was developed to stochastically downscale TWSA from coarse resolution (4^o) to fine resolution (0.25^o). For a particular month, the model was parameterized by minimum TWSA at 0.25^o and a parameter related to degree of multifractality for that month. One thousand realizations of fine resolution TWSA were generated for each month. The model produced much larger TWSA values at fine resolutions that were not captured by the coarse resolution TWSA. These extreme values produced by model are beneficial for assessing risk of region being very dry or very wet at local scales. Future research should consider whether the downscaled TWSA patterns can be conditioned to reproduce fine-scale TWSA values inferred from well and other local data.

Chapter 4 Temporal Variations of NDVI and LAI and Interactions with Hydroclimatic Variables in a Large and Agro-Ecologically Diverse Region

4.1 Introduction

Understanding the impacts of hydroclimatic variations on regional vegetation (*i.e.*, vegetation averaged over an ecosystem, state, or major watershed) is important for many applications. Seasonal and interannual changes in vegetation have consequences for a region's economy and food security because vegetation is a major source of energy and food (*Kogan,* 2019; *Trumbore et al.,* 2015). Changes in vegetation can also alter the partitioning of precipitation into interception, surface runoff, and evapotranspiration and therefore affect watershed management. Reductions in vegetation cover can destabilize soil and increase soil erosion (*Jiao et al.,* 2017; *Kumari et al.,* 2021; *Zhou et al.,* 2021). Vegetation is also a key source of CO_2 sequestration, so it mediates the effects of increasing greenhouse gas emissions (*Ahlstrom et al.,* 2015; *Trumbore et al.,* 2015). The relationship between hydroclimatic variations and vegetation dynamics also affects the sensitivity of a region to droughts and floods (*AghaKouchak et al.,* 2015; *Fiorillo et al.,* 2018; *Kogan and Sullivan,* 1993; *Zhang et al.,* 2004) and the vulnerability of an ecosystem to wildfires (*Ehsani et al.,* 2020).

At regional scales, vegetation is necessarily quantified using vegetation indices derived from satellite remote sensing (*Barbosa et al.,* 2015; *Fensholt et al.,* 2004; *Lhermitte et al.,* 2011; *Zhang et al.,* 2017; *Gessner et al.,* 2013). Many vegetation indices have been developed, but normalized difference vegetation index (NDVI) is the most widely used (*Glenn et al.*, 2008; *Rouse et al.,* 1974; *Tucker,* 1979; *Xue & Su,* 2017). It is calculated using the reflectances in the near infrared and red bands. NDVI is a measure of the greenness of the vegetated land surface and is

considered an indirect measure of vegetation health and density (*AghaKouchak et al.,* 2015; *Yang et al.,* 2014). Leaf area index (LAI) is also widely used. It is defined as the ratio of projected one-sided green leaf area to the ground area (*Gitelson et al.,* 2003). LAI is a biophysical property and an essential variable for monitoring, understanding, and modeling the land surface (*Baret et al.,* 2013; *Brown et al.,* 2017; *Kang et al.,* 2016; *Verger et al.,* 2016; *Wang et al.,* 2017; *Zoungrana et al.,* 2015). LAI can be estimated by inverting a radiative transfer model that is forced with canopy reflectances and land use data (*Kang et al.,* 2016; *Wang et al.,* 2017).

Studies examining the connections between hydroclimatic forcing and vegetation dynamics have been performed primarily using NDVI or similar indices (e.g., *A et al.,* 2015, 2017; *Chikoore and Jury,* 2010; *Eklundh,* 1998; *Gu et al.,* 2008; *Fan et al.,* 2016; *Kawabata et al.,* 2001; *Ichii et al.,* 2002; *Mao et al.,* 2012; *Martiny et al.,* 2005 & 2006; *McGrath et al.,* 2012; *Nicholson et al.,* 1990; *Nightingale and Phinn,* 2003; *Richard and Poccard,* 1998; *Xue et al.,* 2021; *Yang et al.,* 1997, 2009, 2014). Analyses using LAI are much more limited (*Bobee et al.,* 2012, *Zhang et al.,* 2004; *Zoungrana et al.,* 2015). The use of a single vegetation index implicitly assumes that the selected index adequately captures the vegetation's response to hydroclimatic variability. However, empirical relationships between the two indices are nonlinear at low LAI values and saturate at high LAI values (*Gitelson et al.,* 2003, 2007; *Myneni et al.,* 2002; *Reichenau et al.,* 2016). Also, within large regions, multiple plant functional types (PFTs) can occur, and the NDVI-LAI relationship can vary between PFTs (*Huete,* 2012; *Zhang et al.,* 2017). Therefore, NDVI and LAI might respond differently to hydroclimatic changes at large scales (such as 0.5^{o} degree or larger).

The objectives of this study are to compare the temporal variations of NDVI and LAI in a large and diverse region and to examine the hydroclimatic variables that most affect NDVI and LAI and the time lag at which those relationships are strongest. Understanding the differences between the responses of regional NDVI and LAI to hydroclimatic variability will help researchers select the index that best captures the vegetation's response to the hydroclimatic variables of interest. To accomplish these goals, the seasonal and interannual variations in regional hydroclimatic indicators are compared to variations in NDVI and LAI for a study region in California. Then, the hydroclimatic controls on NDVI and LAI are quantified using lagged cross-correlation analyses.

4.2 Materials and Methods

4.2.1 Study Region

The analysis is performed for the combined Sacramento River and San Joaquin River basins (~154,000 km^2). These basins are in one of the world's most climatically and biologically diverse regions (*Hayhoe et al.,* 2004; *Kauffman,* 2003; *Lenihan et al.,* 2007) (Figure 4.1). The Sierra Nevada mountains in the east have cold winters and dry summers, and the Central Valley in the west ranges from a Mediterranean climate in the north to a semiarid climate in the south (*Kauffman,* 2003; *Mooney and Zavaleta,* 2016). The climatic variation has resulted in vegetation diversification (*Mooney and Zavaleta,* 2016). The eastern side of the region is dominated by conifer forests with some shrublands, while the Central Valley primarily consists of cultivated croplands with grasslands at the periphery (*Huntsinger and Oviedo,* 2014; *Kauffman,* 2003; *Lenihan et al.,* 2003). Much of the region is water-limited, and the agriculture in the Central Valley is maintained through intensive irrigation from a combination of surface water storage and the

underlying aquifer (*Faunt et al.*, 2016). Irrigation activity peaks from June to August (*Yang et al.,* 2017). Based mainly on data availability, the study period was selected to be October 2002 to September 2015 (156 months), which spans 13 water years (water year 2003 begins October 1, 2002 and ends September 30, 2003).

4.2.2 Data Processing

4.2.2.1 Precipitation, Temperature and Vapor Pressure Deficit

The PRISM (Parameter-elevation Relationships on Independent Slopes Model) climate group at Oregon State University (http://www.prism.oregonstate.edu/) provides monthly precipitation, mean temperature, and maximum and minimum vapor pressure deficit from 1981 to the present at a spatial resolution of 4 km for the conterminous United States (*Daly et al.*, 2008; *Daly et al.*, 2015). PRISM is a knowledge-based climate-elevation regression model. It uses gridded elevation data, approximately 13,000 precipitation stations, 10,000 temperature stations, 3,500 surface weather stations and other spatial datasets to interpolate precipitation, temperature, and vapor pressure deficit in physiographically complex regions. For this study, the maximum and minimum vapor pressure deficits were averaged to estimate a mean vapor pressure deficit for each grid cell. Then, the monthly precipitation, mean temperature, and mean vapor pressure deficit data were spatially averaged over the study region. For consistency with the GRACE (Gravity Recovery And Climate Experiments) data, which is described later in the manuscript, the monthly precipitation, temperature, and vapor pressure deficit anomalies were calculated by subtracting the temporal averages from January 2004 to December 2009 (the exact period used to calculate the averages has little effect on the results).

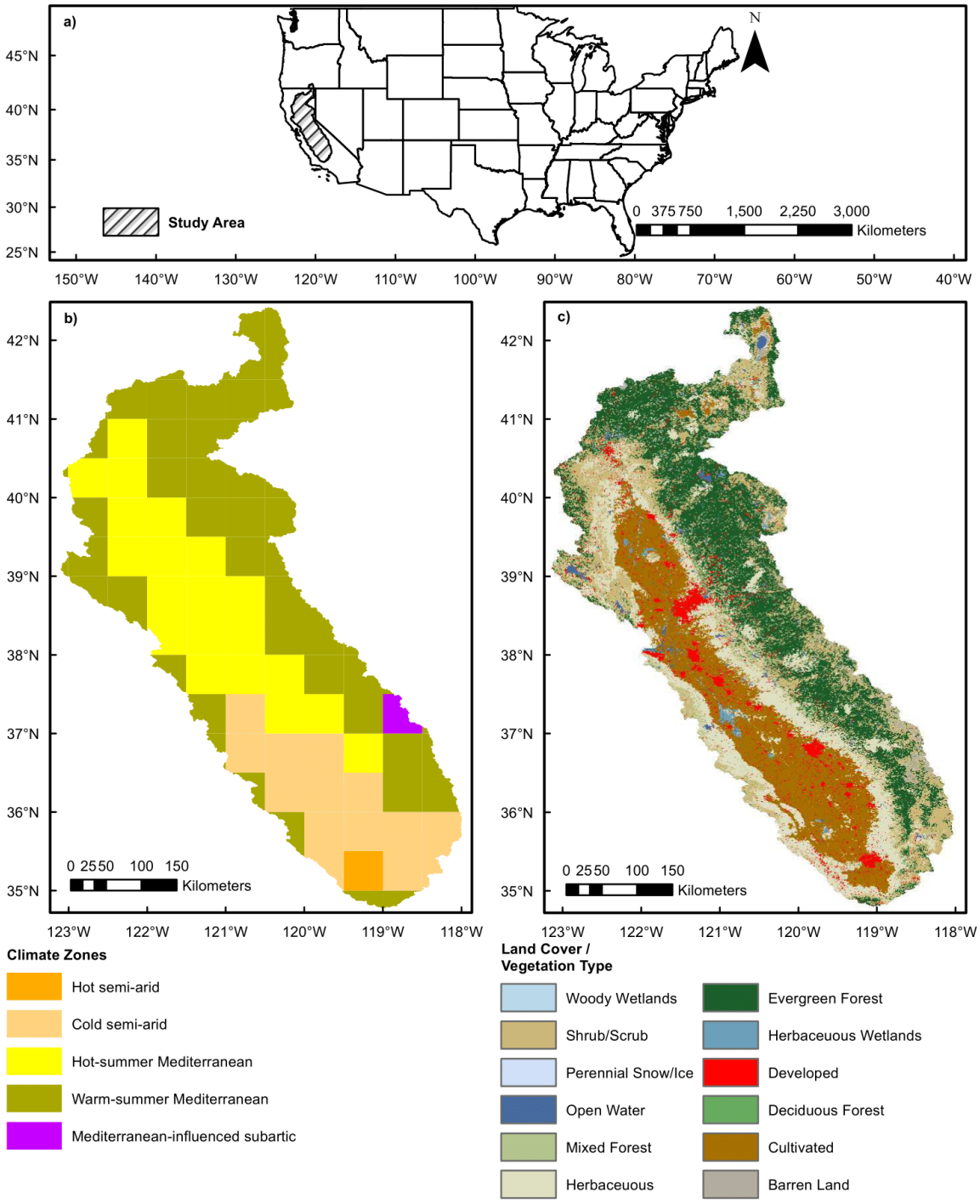

Figure 4.1. a) The combined Sacramento River and San Joaquin River basins (i.e., study region) in California, b) climatic zones within the study region from the Koppen-Geiger climate classification (*Kottek et al.,* 2006) and c) land cover for the study region derived from the National Land Cover Database 2016 (NLCD; *Yang et al.,* 2018)

4.2.2.2 Streamflow

Streamflow data were obtained from the National Water Information System of the United States Geological Survey (USGS) (http://waterdata.usgs.gov/nwis/). Streamflow from the study region was estimated by summing the streamflow volumes from the Sacramento River at Verona (USGS gauge 11425500) and the San Joaquin River at Vernalis (USGS gauge 11303500). The resulting streamflow volume was converted to a depth by dividing it by the combined basins' area. Streamflow anomalies were produced by subtracting average streamflow from January 2004 to December 2009.

4.2.2.3 Evapotranspiration

Ma and Szilagyi (2019) produced the estimates of monthly actual evapotranspiration (ET) over the conterminous United States for 1979-2015 at a spatial resolution of 4 km using a form of the complementary relation developed by *Szilagyi et al.* (2017). These estimates of ET do not require any information on vegetation and soil parameters and are entirely based on basic atmospheric data. The ET estimates of *Ma and Szilagyi* (2019) were extracted and spatially averaged over the study region and converted into anomalies by subtracting the average ET from January 2004 to December 2009.

4.2.2.4 Total Water Storage

GRACE measures the temporally variable gravity field, whose variations over land areas are mainly caused by redistribution of total water (*i.e.*, soil moisture, snowpack, groundwater, and surface waterbodies) (*Rodell et al.,* 2004). GRACE observations are available as monthly TWSAs, which are deviations from the long-term (2004-2009) mean. GRACE TWSA have been linked with vegetation activity to understand the ecohydrology of water-limited regions (e.g., *A et al.,*

2015, 2017; *McGrath et al.,* 2012; *Yang et al.,* 2014). We obtained TWSA data as equivalent water depths from the University of Colorado GRACE Data Analysis Website (http://geoid.colorado.edu/grace/). The web portal hosts TWSA's from GRACE data processed by the Center for Space Research (CSR), the German Research Center for Geosciences (GFZ) and the Jet Propulsion Laboratory (JPL). Following *Sakumura et al.* (2014), we used the arithmetic average of the three TWSA datasets. Separate regional averages are available for the Sacramento River and San Joaquin River basins. Because we are considering the combined river basins, the overall TWSA values were determined using an area-weighted average. We also obtained TWSA estimates from global positioning system (GPS) measurements within the study region (*Argus et al.*, 2014; *Fu et al.*, 2015). The results using the GPS estimates largely agreed with those using GRACE, so only the GRACE values are presented in this study.

The rate of change of TWSA, which is denoted $d(TWSA)/dt$, is also considered because it appears in the regional water balance equation. Monthly values of $d(TWSA)/dt$ were calculated using a simple backward difference approach,

$$\left(\frac{dTWSA}{dt}\right)_k = \frac{TWSA_k - TWSA_{k-1}}{\Delta t} \tag{4.1}$$

where $\left(\frac{dTWSA}{dt}\right)_k$ is the rate of change of TWSA for month k and Δt is the time step (1 month). The values of $d(TWSA)/dt$ are expected to indicate the extent to which both natural hydrologic processes and human activities are transporting water in or out of the study region.

4.2.2.5 Vegetation Indices

NDVI and LAI were obtained from the MODerate resolution Imaging Spectroradiometer (MODIS) satellite mission. The MODIS NDVI product (MOD13A3) is calculated using reflectances (MOD09 products) in the near infrared (ρ_{NIR}) and red (ρ_R) bands that are corrected for molecular scattering, ozone absorption and aerosols. NDVI is calculated as $(\rho_{NIR} - \rho_R) / (\rho_{NIR} + \rho_R)$ which standardizes the NDVI range from -1 to 1 (*Huete et al.,* 1999). MOD13A3 is available at http://e4ftl01.cr.usgs.gov/MOLT/. It is a monthly product at a resolution of 1 km (*Huete et al.,* 2002).

The MODIS LAI product (MOD15) is estimated using the MOD09 products, the land cover type product (MOD12) and ancillary information that describes six biomes and soil patterns (*Myneni et al.*, 2002). An inverse radiative transfer model in the form of a look-up table produces the LAI as an 8-day composite at a resolution of 1 km (*Myneni et al.*, 2002). The look-up table contains information on pre-modeled surface reflectances, vegetation structure characteristics, and land use/cover (*Fang and Liang,* 2014). An inversion process solves for the vegetation structural characteristics that match the MODIS surface reflectances. If the inversion procedure fails, a pre-determined relationship between NDVI and LAI is used (*Knyazikhin et al.,* 1999; *Myneni et al.,* 2002). For this study, the 8-day LAI composites were averaged to obtain monthly LAI values (*Zhao et al.,* 2016). NDVI and LAI were extracted and spatially averaged over the region and their anomalies were calculated by subtracting the average from January 2004 to December 2009. The rate of change in LAI, which is denoted $d(LAI)/dt$, is also considered. Because LAI is associated with the cumulative growth of leaves, $d(LAI)/dt$ is an indication of growth rate.

4.2.3 Analysis Methods

4.2.3.1 Seasonality and Interannual Variability

Vegetation is characterized by seasonal and interannual variations. Seasonal variations in vegetation can occur due to temperature seasonality, precipitation seasonality in water-limited ecosystems and cropping patterns in agricultural areas (*Bobee et al.,* 2012; *Davenport and Nicholson,* 1993; *Kramer,* 1999; *Liu et al.,* 2017; *Xu et al.,* 2013; *Zhang et al.,* 2005, 2006). Interannual variations in vegetation often correspond to climatic variations (*Fisher and Mustard,* 2007).

The seasonal variations in each variable were examined using the mean anomaly for each calendar month (*Yang et al.,* 2014; *Zhang et al.,* 2004). The mean anomaly for calendar month *i* is denoted $\overline{x}_i$ and calculated as,

$$\overline{x}_i = \frac{1}{N}\sum_{j=1}^{N} x_{i,j} \tag{4.2}$$

where *x* is the anomaly of interest, *j* is the year and *N* is the total number of years in the dataset. Interannual variations were examined using the mean value for each variable during each water year.

4.2.3.2 Cross-Correlation Analysis

Hydroclimatic variation is expected to precede the variation of the vegetation indices (*Yang et al.,* 2014; *Gessner et al.*, 2013; *Gu et al.*, 2018). Cross-correlation has been used by numerous researchers to investigate the time-lagged hydroclimatic controls on vegetation in different hydroclimatic and ecological settings (e.g., *Andrew et al.,* 2017; *Capodici et al.,* 2008; *Lin et al.,* 2017).

Seasonality in hydroclimatic and vegetation indicators produces serially correlated or autocorrelated time series, and autocorrelation can produce misleading estimates of cross-correlation (*Eklundh,* 1998; *Lhermitte et al.,* 2011; *Lin et al.,* 2015; *Olden and Ne,* 2001). In such cases, *Dean and Dunsmuir* (2016) indicated that the time series must be prewhitened to ensure that at least one of the series is free of autocorrelation. Following *Andrew et al.* (2017) and *Yang et al.* (2014), the hydroclimatic and vegetation indicators were prewhitened by removing their seasonal cycles. Specifically,

$$x_{prewhitened_{i,j}} = x_{i,j} - \overline{x}_i \quad (4.3)$$

where $x_{prewhitened_{i,j}}$ is the prewhitened value of variable *x* for month *i* and year *j*.

Furthermore, shared long-term trends in the time series can inflate cross-correlations, and a long-term trend in one time series can obscure the cross-correlation (*Probst et al.,* 2012). To avoid these issues, we detrended the prewhitened hydroclimatic and vegetation time series by removing any observed linear trends.

The cross-correlation analysis was performed at lags from 0 to 6 months by shifting the prewhitened-detrended vegetation time series backwards one month at a time and computing Pearson's correlation coefficient *r* between the prewhitened-detrended hydroclimatic and vegetation time series. The significance of each correlation was tested using the t-test, and the associated *p* values are reported (*Edgell and Noon,* 1984).

4.3 Results

4.3.1 Seasonality and Interannual Variability

Figure 4.2 shows the seasonal and interannual variability of the hydroclimatic and vegetation anomalies. We focus first on the seasonal cycles of the variables. The precipitation anomalies

reach their peak in December, and they reach their minimum during the summer months (Figure 4.2a&b). Among the hydroclimatic variables, precipitation reaches it seasonal peak earliest in the water year, which is expected because precipitation provides water to the other variables. The seasonal cycle of the streamflow anomalies resembles the seasonal cycle of precipitation but is lagged roughly 1 month (Figure 4.2d&e). This behavior is expected because streamflow is supplied in part by precipitation and responds relatively quickly to precipitation events. The total streamflow is 38% of the total precipitation of this region (for the study period, the average water year precipitation is 650 mm, and the average water year streamflow is 250 mm). The seasonal cycle of ET reaches its maximum in May and June when precipitation is approaching its minimum. Conversely, ET reaches its minimum in December when precipitation is at its maximum (Figure 4.2g&h). The seasonal cycle for ET is partly expected because the temperature and vapor pressure deficit both reach their maximums in summer (see Figure B1 in the Appendix B). Thus, the ET is large when the atmospheric demand for ET is also large. However, the large lag compared to precipitation suggests either that precipitated water remains in the region for a prolonged period before a portion exits as ET or that ET is derived from long-term stores of water such as groundwater rather than precipitated water. The seasonal cycle of the $d(TWSA)/dt$ (Figure 4.2j&k) largely resembles the seasonal cycle of precipitation. It also resembles the inverse of the ET cycle. During winter, almost all the precipitation occurs, and $d(TWSA)/dt$ increases in response to that precipitation. In summer, precipitation is very low, so $d(TWSA)/dt$ decreases in response to the high ET rates. The seasonal cycle of TWSA (Figure 4.2m&n) has high values between about February and May and reaches a peak in March. These high values roughly connect the period when precipitation adds water to the region and the period when ET removes

water from the region. The seasonal cycle of TWSA is also delayed by about two months relative to *d*(*TWSA*)/*dt.* This delay is expected because *d*(*TWSA*)*/dt* represents the rate of change of TWSA. Positive values of *d*(*TWSA*)*/dt* are needed before TWSA can increase to large values.

Figure 4.2p&q shows the seasonal cycle of NDVI. The rate of increase in NDVI is somewhat slower than the rate of increase in precipitation or *d*(*TWSA*)/*dt*. Precipitation reaches its peak in about December, while NDVI peaks during February through April (the mean NDVI peaks in April, but in years with above average NDVI, NDVI tends to peak earlier). The seasonal cycle of NDVI more closely resembles the seasonal cycle of TWSA, but it lags TWSA by about 1 month. This resemblance is expected because the vegetation greenness and photosynthetic capacity depend on water availability (*Kogan,* 2019). Figure 4.2s&t shows the seasonal cycle of *d*(*LAI*)/*dt*. The seasonality of *d*(*LAI*)/*dt* resembles the seasonality of TWSA. Both variables reach their maximums in March. Thus, the seasonal peak *d*(*LAI*)/*dt* also occurs near the peak in NDVI. This result suggests that the highest rate of growth in leaf area roughly coincides with the highest water availability and with the highest vegetation greenness. This result is consistent with plant physiology because the most abundant growth is expected when the vegetation is not water stressed (*Kogan,* 2019). It also suggests monthly variations in NDVI and *d*(*LAI*)/*dt* are associated with the current availability of water. Finally, the seasonal cycle of LAI is shown in Figure 4.2v&w. The LAI reaches its peak from June through August. This peak occurs later than the peak for TWSA, NDVI, and *d*(*LAI*)/*dt*. However, the seasonal cycle for LAI roughly resembles the seasonal cycle of ET (see Figure 4.2g&h). The asynchronicity of NDVI and LAI is novel and confirms the central hypothesis of this study. When water becomes available, the vegetation becomes greener (which implies that NDVI increases) and begins growing (which increases *d*(*LAI*)/*dt*) (*Kogan,*

2019). The result of the growth is increased biomass, which eventually results in greater LAI and ET. The early additions of biomass are visible in the NDVI while later additions are less visible due to increasing NDVI saturation (*Reichenau et al.,* 2016). The similarity of NDVI with TWSA and $d(LAI)/dt$ in this region suggests that NDVI emphasizes vegetation growth rate. In contrast, LAI better reflects the cumulative growth of leaf area and ET.

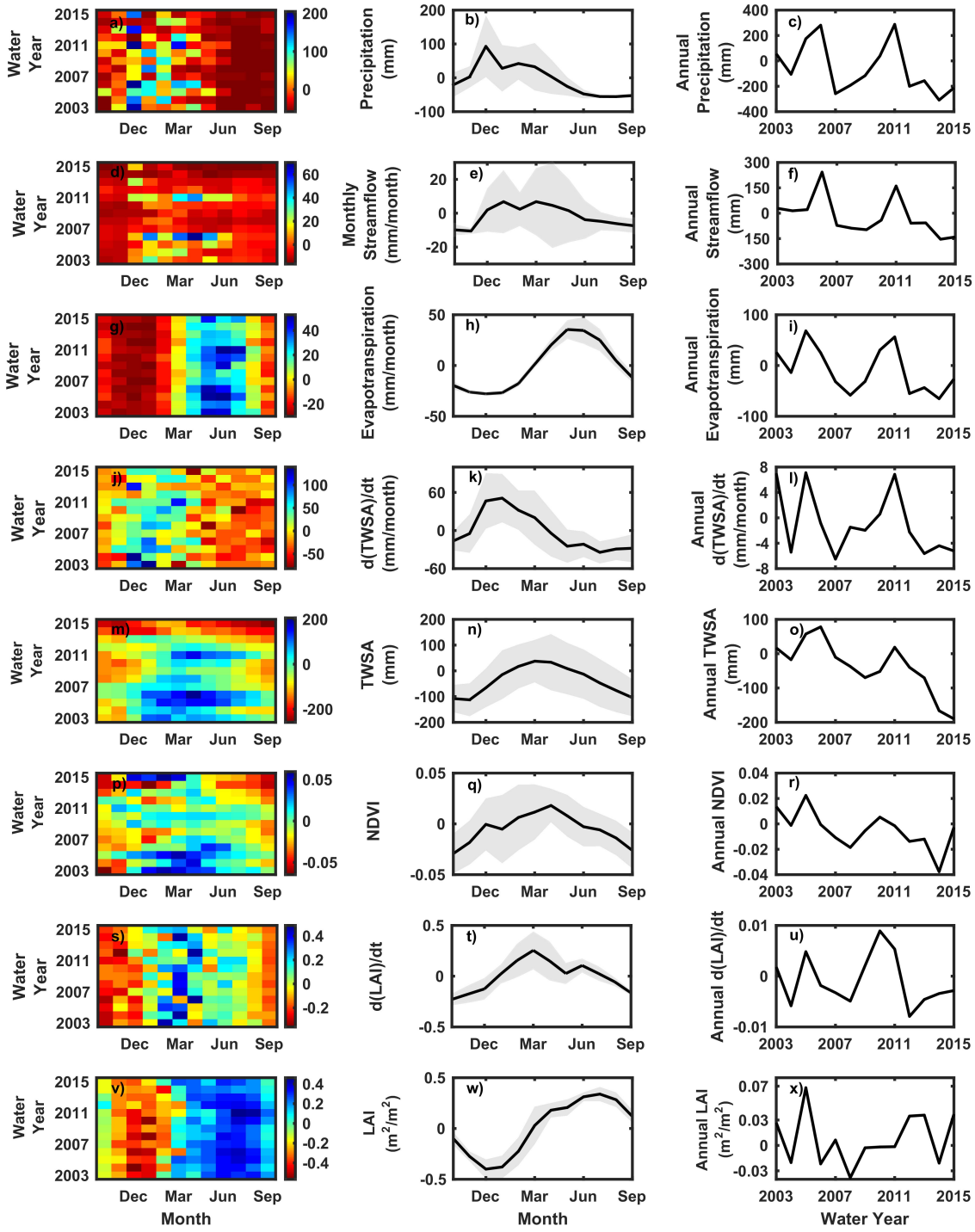

Figure 4.2. a) Hovmoller diagram of precipitation anomalies; b) seasonality of precipitation anomalies (in all plots, shaded region shows +/- one standard deviation); c) annual precipitation anomalies; d) Hovmoller diagram of streamflow anomalies; e) seasonality of streamflow anomalies; f) annual streamflow anomalies; g) Hovmoller diagram of ET anomalies; h) seasonality of ET anomalies; i) annual ET anomalies; j) Hovmoller diagram of d(TWSA)/dt anomalies; k) seasonality of d(TWSA)/dt anomalies; l) annual d(TWSA)/dt anomalies; m) Hovmoller diagram TWSA; n) seasonality of TWSA; o) annual TWSA; p) Hovmoller diagram of

NDVI anomalies; q) seasonality of NDVI anomalies; r) annual NDVI anomalies; s) Hovmoller diagram of d(LAI)/dt anomalies; t) seasonality of d(LAI)/dt anomalies; u) annual d(LAI)/dt anomalies; v) Hovmoller diagram of LAI anomalies; w) seasonality of LAI anomalies; x) annual LAI anomalies.

To better understand why the seasonal cycles of NDVI and LAI differ, the region was divided into its major PFTs according to the 2016 National Land Cover Database (*Yang et al.,* 2018). The region includes four PFTs: crops, evergreen forests, grasslands, and shrublands (Figure 4.1). For each PFT, the monthly NDVI and LAI values were spatially averaged and then converted into anomalies. The anomalies of each month were then used to determine the average seasonal cycle and the standard deviation in each month (Figure 4.3). For crops, the NDVI increases late in the summer because much of the water supply is obtained from irrigation rather than precipitation, and the seasonal cycles for NDVI and LAI are aligned. For evergreen forests, the NDVI remains relatively stable while the LAI has a clear seasonal cycle. The stability of NDVI means that the evergreen forests have little impact on the seasonal cycle of the regional-wide NDVI. The NDVI and LAI seasonal cycles are somewhat asynchronous for grasslands and clearly asynchronous for shrublands. Thus, the regional asynchronicity arises from these two PFTs. Figure 4.4 plots the monthly mean LAI against the monthly mean NDVI. The results show that a strong relationship exists between the two indices for croplands, a weak relationship exists for grasslands, and no relationship exists for evergreen forests or shrublands. For crops, the LAI is typically below 2 m^2/m^2, which is commonly cited as the LAI at which NDVI saturates (*i.e*., any additional leaves do not increase NDVI) (*Haboudane et al.*, 2004; *Gamon et al.*, 1995; *Tesfaye and Awoke,* 2021). Thus, a relationship is expected for crops. On the other hand, evergreen forests have large LAI values, so those LAI values are not expected to show a relationship with NDVI (see Figure 4.4b). Grasslands and shrublands tend to have intermediate LAIs between crops and evergreen forests. Based on examination of individual pixels, the asynchronous NDVI and LAI values for these PFTs primarily arise from grid cells with larger LAI values.

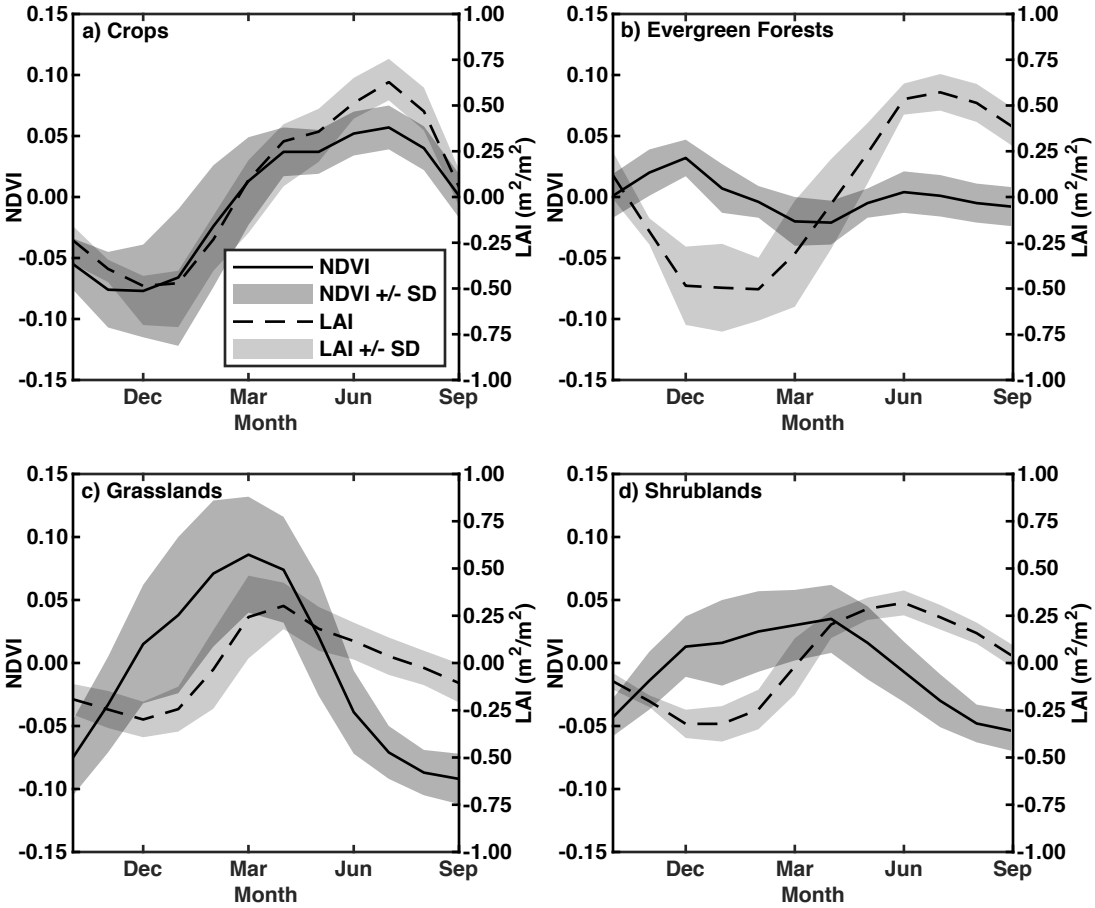

Figure 4.3. Seasonal variation in monthly mean NDVI and LAI anomalies for a) crops, b) evergreen forests, c) grasslands, and d) shrublands

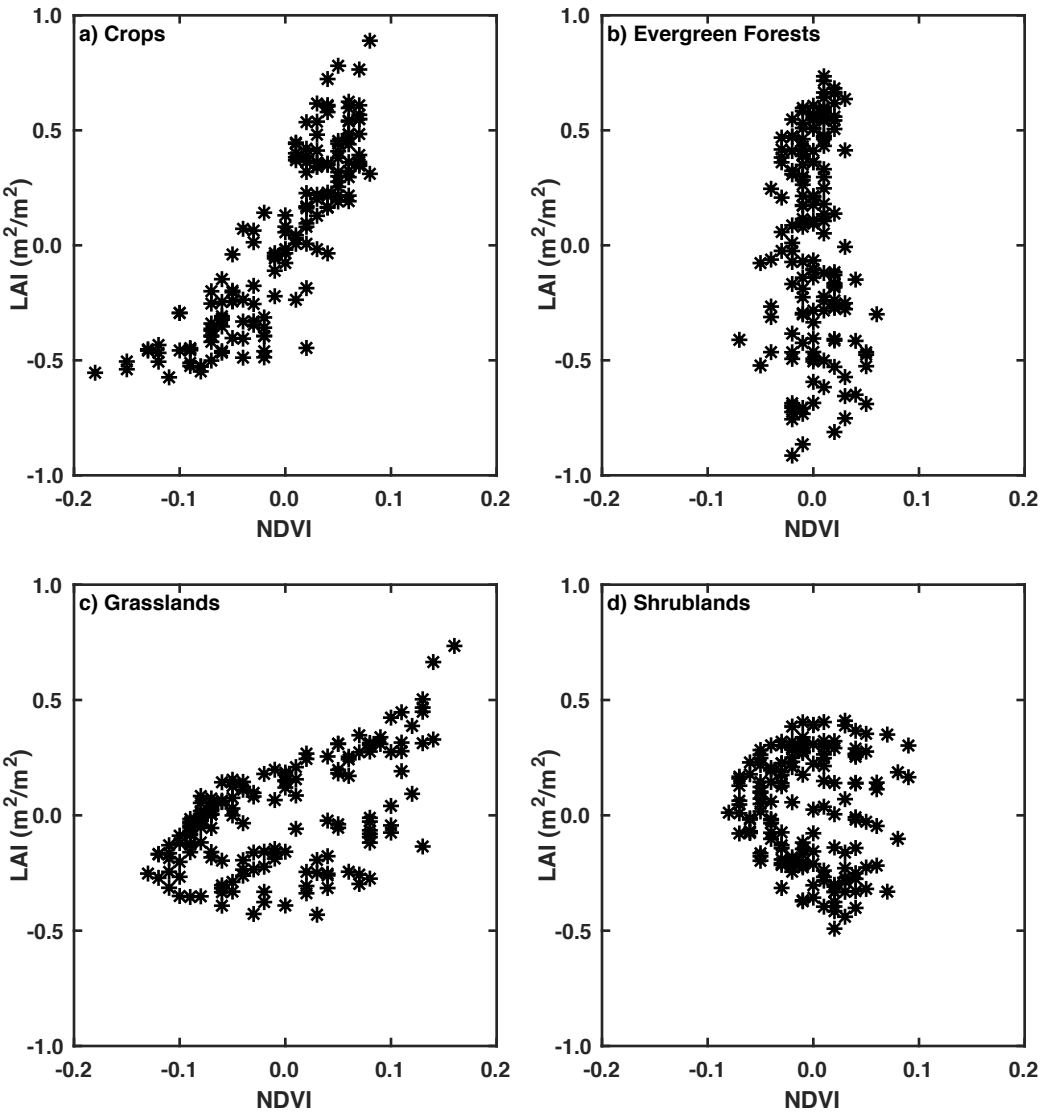

Figure 4.4. Relationship between monthly mean NDVI and LAI anomalies for a) crops, b) evergreen forests, c) grasslands, and d) shrublands

Figure 4.2 also shows the interannual variability of the hydroclimatic variables and vegetation indices. The annual $d(TWSA)/dt$ anomalies resemble the annual precipitation anomalies except for some differences in 2005 and 2006. Recall that the seasonal cycles for these two variables were also similar. The interannual variability of NDVI resembles that of TWSA (these variables also had similar seasonal cycles) and to a lesser extent precipitation and ET. NDVI tends to decrease during the study period likely due to less abundant natural vegetation due to drought-induced die off during this period (*Dong et al.,* 2019; *Herrmann et al.,* 2016). *McGrath et al.* (2012) made a similar argument for the response of NDVI to droughts in Australia. Interannual variability of $d(LAI)/dt$ resembles that of precipitation and $d(TWSA)/dt$. No clear pattern is observed in the interannual variability of LAI. Generally, LAI is lower during the drought period 2007-2009 compared to the drought period 2012-2015.

4.3.2 Cross-Correlation Analysis

Table 4.1 reports the lag at which the prewhitened-detrended hydroclimatic indicators are most strongly correlated to the prewhitened-detrended NDVI and LAI. It should be noted that the prewhitened-detrended time series of TWSA still has significant autocorrelation, so its cross-correlations might be misleading (*Eklundh,* 1998; *Lin et al.,* 2015; *Olden and Ne,* 2001).

Table 4.1 shows that NDVI anomalies are positively correlated with precipitation anomalies at a lag of one month. The positive correlation of 0.27 indicates that the variation of precipitation during a given month explains 7% of the variation in NDVI during the following month. The positive correlation between the precipitation and NDVI is similar to the relationship between these variables that was observed at the seasonal and interannual time

scales. This result is expected because an increase in precipitation provides more water to the vegetation. Thus, vegetation greenness is expected to increase with precipitation increases. In contrast, LAI is negatively correlated with precipitation at a lag of zero months, and the variation of precipitation during a given month explains 26% of the variation in LAI. The negative correlation indicates that lower precipitation is associated with higher LAI. This result is unexpected and likely occurs due to negative correlations between precipitation and other variables more directly associated vegetation abundance (*Herrmann et al.,* 2016). The dry season corresponds to the warmest part of the year when vegetation growth is enhanced by abundant solar radiation (due to clear skies). Also, some crops within the region are irrigated from groundwater during this time of the year. Furthermore, LAI represents the cumulative growth of the leaf area, which is expected to depend on the cumulative precipitation of past few months (*Tesemma et al.,* 2014) rather than the precipitation in a single month as considered in this analysis.

Table 4.1 shows that both NDVI and LAI are positively correlated with mean temperature at a lag of zero months. However, variation in mean temperature only explains 3% of the variation in NDVI compared to 22% of the variation in LAI. Positive correlation of mean temperature with the vegetation indicators at zero lag implies a greater mean temperature is associated with greater vegetation activity in the same month. Warm temperatures can make the environment more favorable for vegetation activity and thus promote higher NDVI and LAI, provided adequate water is available. NDVI is negatively correlated with mean vapor pressure deficit at a lag of one month, but LAI is positively correlated at a lag of zero months. The negative lagged correlation for NDVI is expected because anomalously high vapor pressure deficits can

introduce water stress and reduce vegetation greenness in the following month. The positive correlation for LAI at zero months is more difficult to interpret given the more cumulative nature of LAI. NDVI and LAI are both positively correlated with the ET at a lag of one month. Thus, larger ET values in a given month are associated with greater NDVI and LAI in the subsequent month. The result is expected because transpiration provides access to nutrients and drives vegetation growth (*Djaman et al.,* 2013). $d(TWSA)/dt$ has a much stronger correlation with LAI than NDVI. Variation in $d(TWSA)/dt$ explains less than 3% of the variation in NDVI, but variation in $d(TWSA)/dt$ explains 12% of the variation in LAI. The negative correlation between LAI and $d(TWSA)/dt$ at zero lag indicates that a negative $d(TWSA)/dt$ anomaly in a month is associated with in a positive LAI anomaly during the same month. $d(TWSA)/dt$ tends to be negative when ET is large, and greater ET is expected when LAI is large.

Table 4.1. Summary of the cross-correlation analysis between prewhitened-detrended hydroclimatic and vegetation indices. Lags are in months.

	NDVI			LAI		
	r	p	Lag	r	p	Lag
Precipitation	0.27	<0.01	1	-0.51	<0.01	0
Temperature	0.18	0.02	0	0.46	<0.01	0
Vapor Pressure Deficit	-0.26	<0.01	1	0.25	<0.01	0
ET	0.36	<0.01	1	0.28	<0.01	1
$d(TWSA)/dt$	0.15	0.07	6	-0.36	<0.01	0
TWSA	0.20	0.02	1	0.31	<0.01	2

Overall, Table 4.1 shows that most hydroclimatic forcing variables (*i.e.,* precipitation, mean temperature, $d(TWSA)/dt$, and TWSA) are more strongly and significantly correlated with LAI than NDVI. The notable exception to this tendency is ET, which is more strongly correlated with NDVI than LAI. Also, the strongest correlations of hydroclimatic variables with LAI tend to occur at zero lag. For NDVI, the lag with the strongest correlation differs more between the hydroclimatic indicators. Although not shown in Table 1, we also examined whether the lags with the strongest correlations exhibit seasonality. Specifically, the cross-correlation analysis was also performed separately for each month of the year. Overall, the results show that the correlations are strongest during the summer months, but clear seasonal variations in the lags were not observed.

4.4 Discussion

The results of this study show that NDVI and LAI exhibit asynchronous mean seasonal cycles. Specifically, the mean seasonal cycle of LAI lags the mean seasonal cycle of NDVI. One might expect NDVI and LAI to have similar seasonal cycles because NDVI and LAI have a well-documented association at a given time, and NDVI is often used to estimate LAI (e.g., *Reichenau et al.,* 2016). However, *Wang et al.* (2005) showed that the NDVI-LAI relationship can vary seasonally (and interannually) in response to temporal variations in environmental conditions including hydroclimatology and phenology. The NDVI-LAI relationship also depends on vegetation type and can vary in time depending on the phenological development of different vegetation types within a given PFT (*Gitelson et al.*, 2003). Furthermore, as LAI becomes large, the additional layers of green leaves are not captured by NDVI, which characterizes only the horizontal projection of the vegetation cover (*Gitelson 2004*; *Zhao et al.*, 2016). Finally,

differences could arise from errors associated with the estimation of NDVI and LAI.

Some differences in the observed behaviors of NDVI and LAI can be interpreted as differences between the true projected green vegetation (which is associated with NDVI) and the true LAI. Others either result from errors in the NDVI and LAI estimates or from unrecognized phenomena. The asynchronous seasonal cycles of NDVI and LAI are partially explainable from plant physiology. In the study region, NDVI is high in months when TWSA is high. This result is expected because leaf chlorophyll content increases with lower water stress (*Kogan,* 2019). $d(LAI)/dt$ is also high in months when TWSA is high. This result is also expected because plants grow when they are well watered (*Kogan,* 2019). For grasslands and shrublands, LAI reaches its seasonal peak after NDVI. Because LAI better represents multiple layers of leaves, it captures the cumulative growth of vegetation better than NDVI. The observation that NDVI decreases months before LAI might occur because NDVI emphasizes vegetation greenness (which might diminish with time) more than the leaf abundance (which remains high). In addition to leaf area, NDVI is affected by the presence of non-photosynthetic vegetation (*Huete et al.,* 1999; *Xu et al.,* 2020) and by leaf optical properties, which change with leaf age (*Samanta et al.,* 2012). The earlier decrease of NDVI could also occur if the species composition or spatial pattern of vegetation varies seasonally in response to environmental, hydroclimatic, and resource controls (*Wang et al.,* 2005).

At the interannual time scale, the results indicate that NDVI had a clear decreasing trend in its anomalies (Figure 4.2r). The trend in NDVI is consistent with a decrease in the annual TWSA values. This consistency is expected as NDVI assesses moisture-based vegetation health (*Kogan,* 2019). During the study period, NDVI decreased for all PFTs except evergreen forests, which tend

to be located at higher elevations (Figure B2a). *Dong et al.* (2019) and *Herrmann et al.* (2016) showed that NDVI decreased for low-elevation, water-limited locations and increased for high-elevation, temperature-limited locations during recent droughts in California and the Southwest U.S. At the interannual time scale, LAI did not exhibit a clear decreasing trend during the study period (Figure 4.2x). The LAI for grasslands decreased, while evergreen forests and crops increased (Figure B2b). The interannual variation of crop LAI is somewhat counter intuitive. Crops in the region are intensively irrigated from groundwater during summers (*Yang et al.,* 2017). Heavy groundwater usage in the Central Valley and shifts from alfalfa, cereals, and cotton to nuts and fruits resulted in increased agricultural revenue during the 2014-2016 California drought, which might support higher crop LAIs during that period (*Gebremichael et al.,* 2021; *Xiao et al.,* 2017). The increasing LAI of evergreen forests might have resulted from warmer temperatures at higher elevations and associated increases in vegetation amount (*Herrmann et al.,* 2016). The LAI of grasslands and shrublands likely declined due to stress induced by decreasing water availability (*Dong et al.,* 2019; *Herrmann et al.,* 2016).

The cross-correlation analysis indicates that the hydroclimatic variables typically have stronger correlations with LAI than NDVI. While NDVI is correlated with photosynthetic capacity and vegetation density, it also depends on the soil color, leaf morphology, leaf angle distribution, and the overall canopy structure (*Huete et al.,* 1999; *Samanta et al.,* 2012). These characteristics may be insensitive to monthly variations in the hydroclimatic variables. In contrast, the processed-based algorithm used to estimate MODIS LAI removes such extraneous factors to focus on the leaf area (*Samanta et al.,* 2012). As a result, MODIS LAI has larger variability and more information on the seasonal evolution and structure of vegetation than MODIS NDVI,

particularly for densely vegetated regions (*Zhang et al.,* 2004). Overall, our findings suggest that MODIS LAI is a more sensitive indicator of hydroclimatic variability than MODIS NDVI at regional scales. *Zhang et al.* (2004) developed a climate impact index based on MODIS NDVI and LAI climatology and concluded that NDVI variations underestimate climate related vegetation dynamics. Our study similarly demonstrates that hydroclimatic variations are better captured by LAI than NDVI.

4.5 Conclusions

This study examined whether NDVI and LAI can exhibit different temporal variations in a region due to different relationships with hydroclimatic variables. For the combined Sacramento River and San Joaquin River basins in California, seasonal and interannual variations of hydroclimatic variables and vegetation indices (MODIS NDVI and LAI) were examined. Furthermore, cross-correlations were calculated between the prewhitened-detrended hydroclimatic variables and vegetation indices. The results demonstrate that the regional NDVI and LAI have different mean seasonal cycles. In particular, the mean seasonal cycle for NDVI peaks in April, while the mean seasonal cycle of LAI peaks in July. To a certain extent, NDVI and LAI also exhibit different interannual variations. At the annual scale, NDVI exhibits a noteworthy decline during the study period, while LAI initially declines and then remains more constant. Such differences would be missed in studies that estimate LAI as a direct function of NDVI. The differences in regional NDVI and LAI tend to arise due to different behaviors for the PFTs within the region (evergreen forests, crops, grasslands, and shrublands) and different qualities of the two vegetation indices. Grasslands and shrublands were found to cause the different seasonal cycles of regional NDVI and LAI. Evergreen forests had no or little contribution to the seasonality of regional NDVI due to saturation of NDVI where LAI

is high. The mean seasonal cycle of regional NDVI is similar to the mean seasonal cycles of TWSA and $d(LAI)/dt$. Because TWSA indicates the regional water availability and $d(LAI)/dt$ indicates the regional leaf growth rate, NDVI is emphasizing the greenness and photosynthetic capacity of the vegetation. In contrast, the mean seasonal cycle of regional LAI is similar to the cycle of temperature, vapor pressure deficit, and ET. Because greater transpiration is expected from more abundant leaves, this similarity suggests that the LAI estimates are better describing the cumulative abundance of leaf area. Overall, the prewhitened-detrended NDVI and LAI exhibit distinct cross-correlations with the prewhitened-detrended hydroclimatic indicators. For example, precipitation and $d(TWSA)/dt$ are both positively correlated with NDVI but negatively correlated with LAI. In contrast, vapor pressure deficit is negatively correlated with NDVI and positively correlated with LAI. These results suggest that NDVI and LAI have distinct relationships with the hydroclimatic indicators and that using a single vegetation index to describe the vegetation's response to hydroclimatic variations may be inadequate in some situations.

Several limitations of this study should be recognized. The observation that NDVI and LAI have different temporal variations and different relationships to the hydroclimatic variables is empirical and thus could be region specific. Because the difference in behavior is associated with presence of grasslands and shrublands, the result is more likely to occur in other regions containing these PFTs. The study region also has seasonal cycles of precipitation and ET that are out of phase, and TWSA remains high for a prolonged period between when precipitation occurs and when ET occurs. The seasonal variation in NDVI is aligned with the seasonal variation of TWSA while the seasonal variation in LAI is aligned with the seasonal variation of ET. If those alignments hold in general, regions with more similar precipitation and ET cycles likely would have more

similar NDVI and LAI behaviors. Another limitation of this study arises from the prewhitening and detrending of the data. Such processing is needed to avoid misleading cross-correlations. However, it is also possible that some real relationships between the variables are discarded in this processing.

Two key implications of this study are as follows. First, studies that aim to consider the impacts of climate variations on regional vegetation should consider both NDVI and LAI because two indices may have different responses. If only one index is used, our results support using LAI because, at least for our study region, it contains more information about hydroclimatic variations than NDVI. Using LAI instead of NDVI might provide a clearer indication of vegetation's response to droughts and climate variations. It therefore might improve monitoring of droughts and climate changes, which could also be used to improve models of regional vegetation dynamics. It would be interesting to further the studies of *Ichii et al.* (2002) and *Kawabata et al.* (2001) and perform a global correlation analysis of NDVI and LAI with hydroclimatic variables at different spatial scales. Such a study would indicate regions and scales at which LAI should be used in addition to NDVI to better observe the impacts of hydroclimatic variations. Second, the similarity of $d(LAI)/dt$ and NDVI in this study prompts the hypothesis that LAI depends on the integral of NDVI through time. If confirmed, such a relationship might allow estimation of LAI based on the history of NDVI when a direct relationship between NDVI and LAI does not occur.

Chapter 5 Conclusions and Recommendations

5.1 Conclusions

This dissertation focused on improving GRACE-based TWSA for estimating groundwater depletion and performing ecohydrological analyses. Two improvements to GRACE TWSA were carried out: i) rescaling to capture the lost variability in filtered GRACE TWSA using a complete water budget based on regional precipitation, evapotranspiration, and streamflow and ii) stochastic downscaling of GRACE TWSA from 4^o to 0.625^o using MRCM. Also, large scale climate-water-vegetation interactions involving GRACE TWSA were investigated to understand the ecohydrological implications of a large-scale drought on a diverse agroecological region.

A new algorithm was developed to recapture the variability in GRACE TWSA that is lost during the pre-processing of gravity signals. The new algorithm improves the rescaling process by a) replacing the NSE maximization in the original algorithm with optimization of the relative variability, b) using a complete water budget instead of GLDAS TWSA, and c) unlike the original rescaling process which relies entirely on GLDAS TWSA, the new algorithm uses filtered GRACE TWSA. Optimizing the relative variability between the filtered GRACE TWSA and TWSA from the complete water budget resulted in a larger scale factor and more reliable estimates of rescaled GRACE TWSA when compared with the GPS TWSA for Sacramento and San Joaquin river basins. Furthermore, more severe estimates of groundwater depletion resulted from the rescaled GRACE TWSA based on the new algorithm for the study region.

For three regions with different climatology, geology, and physiography from different parts of the world, GRACE, GRACE-FO, and GPS-based TWSA were shown to exhibit multifractal behavior from spatial resolutions between 0.25^o and 4^o. The multifractal behavior is

characterized by two parameters that are related to the minimum TWSA value at 0.25^{o} and the spatial variance of TWSA. Stochastic downscaling of TWSA approximately reproduced the multifractal behavior between 0.25^{o} to 4^{o} and produced wider ranges in TWSA at the fine resolution (0.0625^{o}) than are observed at the original 0.25^{o} resolution.

NDVI and LAI represent different aspects of large-scale vegetation and have different seasonal cycles. In the large and agroecologically diverse Sacramento and San Joaquin river basins, NDVI is more related to the rate of growth of vegetation while LAI is more related to the total amount of vegetation. For the same study region, the seasonal cycle of NDVI resembles the seasonal cycle of TWSA, whereas seasonal cycle of LAI resembles the seasonal cycle of temperature and evapotranspiration. Generally, LAI was found to be more strongly correlated with hydroclimatic variables including TWSA as compared to NDVI.

5.2 Recommendations

The findings of this dissertation can be furthered as follows:

i) The new rescaling algorithm can be evaluated for longer study duration and other regions.

ii) A CWB approach similar to the improved rescaling algorithm can be used to downscale TWSA. In this case, fine resolution CWB and coarse resolution TWSA can be linked together to determine the downscaling factor for each CWB grid individually using the rescaling algorithm.

iii) The stochastic downscaling using MRCM reproduces the approximate statistics of TWSA at the 0.25^{o} resolution. Combining deterministic estimates of local TWSA (downscaled TWSA using deterministic modeling) with fine resolution stochastically downscaled

TWSA can also be considered. For example, a CWB-based method coupled with stochastic model can be developed to produce statistically conserved local TWSA patterns.

iv) Downscaled TWSA (either stochastically or deterministic or their combination) may contribute to the estimation of streamflow discharges of small ungauged basins. TWSA, climatic, geologic, and physiographic factors can be linked with streamflow of a large region using statistical relationships at the large scale. These statistical relationships might then be applied to smaller ungauged basins having similar climatology, geology, and physiography as the larger basins.

v) Storage-discharge relationships for a large region have been investigated using GRACE TWSA (*Sharma et al.,* 2020). Similarly, downscaled TWSA may contribute to improved understanding of storage-discharge relationships for smaller regions.

vi) As TWSA indicates the degree of wetness of a region, TWSA have been used to assess the flood and drought risks of large regions. Fine resolution TWSA that conserves the statistical properties of coarse resolution TWSA may thus help identify smaller regions prone to flood or drought and can also enhance our understanding on propagation of floods and droughts from small to large regions.

vii) GRACE TWSA also has a coarse temporal resolution (i.e., monthly). Scale-invariance in temporal domain can be hypothesized and tested. Following this spatio-temporal downscaling of TWSA can be performed using MRCM, that can approximately reproduce statistics at fine temporal and spatial resolutions.

References

A, D., Zhao, W., Qu, X., Jing, R., & Xiong, K. (2016). Spatio-temporal variation of vegetation coverage and its response to climate change in North China plain in the last 33 years. *International Journal of Applied Earth Observation and Geoinformation*, *53*, 103–117. https://doi.org/10.1016/j.jag.2016.08.008

A, G., I. Velicogna, J. S. Kimball, and & Y. Kim (2015). Impact of changes in GRACE derived terrestrial water storage on vegetation growth in Eurasia, *Environmental Research Letters*, *10*(12), 124,024. https://doi.org/10.1088/1748-9326/10/12/124024.

A, G., Velicogna, I., Kimball, J. S., Du, J., Kim, Y., Colliander, A., & Njoku, E. (2017). Satellite-observed changes in vegetation sensitivities to surface soil moisture and total water storage variations since the 2011 Texas drought. *Environmental Research Letters*, 12(5), 054006. https://doi.org/10.1088/1748-9326/aa6965

A, G., Wahr, J., and & Zhong, S. (2013). Computations of the viscoelastic response of a 3-d compressible earth to surface loading: an application to glacial isostatic adjustment in Antarctica and Canada. *Geophysical Journal International*, *192*(2), 557–572. https://doi.org/10.1093/gji/ggs030

AghaKouchak, A., Farahmand, A., Melton, F. S., Teixeira, J., Anderson, M. C., Wardlow, B. D., & Hain, C. R. (2015). Remote sensing of drought: Progress, challenges and opportunities. *Rev. Geophys.,* 53(2), 452–480, doi:10.1002/2014RG000456, 2014RG000456.

Ahi, G. O., & Cekim, H. O. (2021). Long-term temporal prediction of terrestrial water storage changes over global basins using GRACE and limited GRACE-FO data. *Acta Geodaetica et Geophysica*, *56*(2), 321-344. https://doi.org/10.1007/s40328-021-00338-4

Ahlström, A., Xia, J., Arneth, A., Luo, Y., & Smith, B. (2015). Importance of vegetation dynamics for future terrestrial carbon cycling. *Environmental Research Letters*, *10*(5), 054019. https://doi.org/ 10.1088/1748-9326/10/5/054019

Alam, S., Gebremichael, M., Ban, Z., Scanlon, B. R., Senay, G., & Lettenmaier, D. P. (2021). Post-Drought Groundwater Storage Recovery in California's Central Valley. *Water Resources Research*, *57*(10), e2021WR030352. https://doi.org/10.1029/2021WR030352

Ali, S., Wang, Q., Liu, D., Fu, Q., Rahaman, M. M., Faiz, M. A., & Cheema, M. J. M. (2022). Estimation of spatio-temporal groundwater storage variations in the Lower Transboundary Indus Basin using GRACE satellite. Journal of Hydrology, 605, 127315. https://doi.org/10.1016/j.jhydrol.2021.127315

Alley, W. M., Healy, R. W., LaBaugh, J. W., and & Reilly, T. E. (2002). Flow and storage in groundwater systems. *Science*, *296*(5575), 1985–1990. https://doi.org/10.1126/science.1067123

Amos, C. B., Audet, P., Hammond, W. C., Bürgmann, R., Johanson, I. A., & Blewitt, G. (2014). Uplift and seismicity driven by groundwater depletion in central California. *Nature, 509*(7501), 483-486. https://doi.org/10.1038/nature13275

Andrew, R. L., Guan, H., & Batelaan, O. (2017). Large-scale vegetation responses to terrestrial moisture storage changes. *Hydrology and Earth System Sciences*, *21*(9), 4469–4478. https://doi.org/10.5194/hess-21-4469-2017

Argus, D. F., Fu, Y., & Landerer, F. W. (2014). Seasonal variation in total water storage in California inferred from GPS observations of vertical land motion. *Geophysical Research Letters*, *41*(6), 1971-1980. https://doi.org/10.1002/2014GL059570

Argus, D. F., Landerer, F. W., Wiese, D. N., Martens, H. R., Fu, Y., Famiglietti, J. S., ... & Watkins, M. M. (2017). Sustained water loss in California's mountain ranges during severe drought from 2012 to 2015 inferred from GPS. *Journal of Geophysical Research: Solid Earth*, *122*(12), 10-559. https://doi.org/10.1002/2017JB014424

Arshad, A., Mirchi, A., Samimi, M., & Ahmad, B. (2022). Combining downscaled-GRACE data with SWAT to improve the estimation of groundwater storage and depletion variations in the irrigated Indus basin. *Science of the Total Environment*, 156044. https://doi.org/10.1016/j.scitotenv.2022.156044

Bacry, E., Kozhemyak, A., & Muzy, J. F. (2013). Log-normal continuous cascade model of asset returns: aggregation properties and estimation. *Quantitative Finance, 13*(5), 795-818. https://doi.org/10.1080/14697688.2011.647411

Barbosa, H. A., Kumar, T. V. L., & Silva, L. R. M. (2015). Recent trends in vegetation dynamics in the South America and their relationship to rainfall. *Natural Hazards*, *77*, 883–899. https://doi.org/10.1007/s11069-015-1635-8.

Baret, F., Weiss, M., Lacaze, R., Camacho, F., Makhmara, H., Pacholcyzk, P., & Smets, B. (2013). GEOV1: LAI and FAPAR essential climate variables and FCOVER global time series capitalizing over existing products. Part1: Principles of development and production. *Remote Sensing of Environment*, *137*, 299–309. https://doi.org/10.1016/j.rse.2012.12.027.

Bertoldi, G. L. (1989). Ground-water resources of the Central Valley of California. *Report no.,* Department of the Interior, US Geological Survey.

Bierkens, M. F., & Wada, Y. (2019). Non-renewable groundwater use and groundwater depletion: A review. *Environmental Research Letters*, *14*(6), 063002. https://doi.org/10.1088/1748-9326/ab1a5f

Bobée, C., Ottlé, C., Maignan, F., De Noblet-Ducoudré, N., Maugis, P., Lézine, A. M., & Ndiaye, M. (2012). Analysis of vegetation seasonality in Sahelian environments using MODIS LAI, in association with land cover and rainfall. *Journal of Arid Environments*, *84*, 38–50. https://doi.org/10.1016/j.jaridenv.2012.03.005.

Brown, L. A., Dash, J., Ogutu, B. O., & Richardson, A. D. (2017). On the relationship between continuous measures of canopy greenness derived using near-surface remote sensing and satellite-derived vegetation products. *Agricultural and Forest Meteorology*, *247*(January), 280–292. https://doi.org/10.1016/j.agrformet.2017.08.012

Buban, M. S., Lee, T. R., & Baker, C. B. (2020). A comparison of the US climate reference network precipitation data to the parameter-elevation regressions on independent slopes model (PRISM). *Journal of Hydrometeorology*, *21*(10), 2391-2400. https://doi.org/10.1175/JHM-D-19-0232.1

Capodici, F., Ciraolo, G., Loggia, G. La, Liuzzo, L., Noto, L. V, & Noto, M. T. (2008). Time Series Analysis of Climate and Vegetation Variables in the Oreto Watershed (Sicily, Italy). *European Water*, (2004), 133–145.

CDEC (2014). "Reservoir Data Summary, 1964 to 2014, Department of Water Resources California Data Exchange Center (CDEC)."

Chen, J. L., Wilson, C. R., Tapley, B. D., Save, H., & Cretaux, J. F. (2017). Long-term and seasonal Caspian Sea level change from satellite gravity and altimeter measurements. *Journal of*

Geophysical Research: Solid Earth, *122*(3), 2274-2290. https://doi.org/10.1002/2016JB013595

Chen, J., & Rodell, M. (2021). Applications of Gravity Recovery and Climate Experiment (GRACE) in global groundwater study. In *Global Groundwater* (pp. 531-543). Elsevier. https://doi.org/10.1016/B978-0-12-818172-0.00039-6

Chen, Z., Zheng, W., Yin, W., Li, X., Zhang, G., & Zhang, J. (2021). Improving the spatial resolution of GRACE-derived terrestrial water storage changes in small areas using the machine learning spatial downscaling method. *Remote Sensing*, *13*(23), 4760. https://doi.org/10.3390/rs13234760.

Cherry, J. (2022). Groundwater: The Missing Educational Curriculum. *Groundwater*. https://doi.org/ 10.1111/gwat.13232.

Chikoore, H., & Jury, M. R. (2010). Intraseasonal Variability of Satellite-Derived Rainfall and Vegetation over Southern Africa. *Earth Interactions*, *14*(3), 1-26. https://doi.org/10.1175/2010EI267.1

Ciruzzi, D. M., & Lowry, C. S. (2017). Impact of complex aquifer geometry on groundwater storage in high-elevation meadows of the Sierra Nevada Mountains, CA. *Hydrological Processes*, *31*(10), 1863-1875. https://doi.org/10.1002/hyp.11147

Cui, L., Zhang, C., Luo, Z., Wang, X., Li, Q., & Liu, L. (2021). Using the local drought data and GRACE/GRACE-FO data to characterize the drought events in Mainland China from 2002 to 2020. *Applied Sciences*, *11*(20), 9594. https://doi.org/10.3390/app11209594

Daly, C., Halbleib, M., Smith, J. I., Gibson, W. P., Doggett, M. K., Taylor, G. H., Curtis, J., and & Pasteris, P. P. (2008). Physiographically sensitive mapping of climatological temperature

and precipitation across the conterminous United States. *International Journal of Climatology*, *28*(15), 2031–2064. https://doi.org/10.1002/joc.1688

Daly, C., Smith, J. I., & Olson, K. V. (2015). Mapping atmospheric moisture climatologies across the conterminous United States. *PloS one*, *10*(10), e0141140. https://doi.org/10.1371/journal.pone.0141140

Davenport, M. L., & Nicholson, S. E. (1993). On the relation between rainfall and the Normalized Difference Vegetation Index for diverse vegetation types in East Africa. *International Journal of Remote Sensing*, *14*(12), 2369–2389. https://doi.org/10.1080/01431169308954042

Dean, R.T., & Dunsmuir, W.T.M. (2016). Dangers and uses of cross-correlation in analyzing time series in perception, performance, movement, and neuroscience: The importance of constructing transfer function autoregressive models. *Behavior Research Methods,* 48, 783–802. https://doi.org/10.3758/s13428-015-0611-2

Deems, J. S., S. R. Fassnacht, and & K. J. Elder (2006), Fractal distribution of snow depth from Lidar data, *Journal of Hydrometeorology*, *7*(2), 285–297, https://doi.org/10.1175/JHM487.1.

Deidda, R. (2000). Rainfall downscaling in a space-time multifractal framework. *Water Resources Research*, *36*(7), 1779-1794. https://doi.org/10.1029/2000WR900038

Deng, S., Liu, S., & Mo, X. (2021). Assessment and attribution of China's droughts using an integrated drought index derived from GRACE and GRACE-FO data. *Journal of Hydrology*, *603*, 127170. https://doi.org/10.1016/j.jhydrol.2021.127170

Djaman, K., Irmak, S., Martin, D. L., Ferguson, R. B., & Bernards, M. L. (2013). Plant nutrient uptake and soil nutrient dynamics under full and limited irrigation and rainfed maize production. *Agronomy Journal, 105*(2), 527-538. https://doi.org/10.2134/agronj2012.0269

Dong, C., MacDonald, G. M., Willis, K., Gillespie, T. W., Okin, G. S., & Williams, A. P. (2019). Vegetation responses to 2012–2016 drought in Northern and Southern California. *Geophysical Research Letters*, *46*(7), 3810-3821. https://doi.org/10.1029/2019GL082137

Edgell, S. E., & Noon, S. M. (1984). Effect of violation of normality on the t test of the correlation coefficient. *Psychological bulletin*, *95*(3), 576. https://doi.org/10.1037/0033-2909.95.3.576

Ehsani, M. R., Arevalo, J., Risanto, C. B., Javadian, M., Devine, C. J., Arabzadeh, A., ... & Behrangi, A. (2020). 2019–2020 Australia fire and its relationship to hydroclimatological and vegetation variabilities. *Water*, *12*(11), 3067. https://doi.org/10.3390/w12113067

Eklundh, L. (1998). Estimating relations between AVHRR NDVI and rainfall in East Africa at 10-day and monthly time scales. *International Journal of Remote Sensing*, *19*(3), 563–570. https://doi.org/10.1080/014311698216198

Escriva-Bou, A., Hui, R., Maples, S., Medellín-Azuara, J., Harter, T., & Lund, J. R. (2020). Planning for groundwater sustainability accounting for uncertainty and costs: An application to California's Central Valley. *Journal of Environmental Management, 264,* 110426. https://doi.org/10.1016/j.jenvman.2020.110426

Famiglietti, J. S., Lo, M., Ho, S. L., Bethune, J., Anderson, K. J., Syed, T. H., Swenson, S. C., de Linage, C. R., and & Rodell, M. (2011). Satellites measure recent rates of groundwater depletion in California's Central Valley. *Geophysical Research Letters*, *38*(3) L03403. https://doi.org/10.1029/2010GL046442

Fan, Y., Li, X., Wu, X., Li, L., Li, W., & Huang, Y. (2016). Divergent responses of vegetation aboveground net primary productivity to rainfall pulses in the Inner Mongolian Plateau, China. *Journal of Arid Environments*, *129*, 1–8. https://doi.org/10.1016/j.jaridenv.2016.02.002

Fang, H., & Liang, S. (2014). Leaf Area Index Models. In *Encyclopedia of Ecology*. https://doi.org/10.1016/B978-0-12-409548-9.09076-X

Fatolazadeh, F., & Goïta, K. (2021). Mapping terrestrial water storage changes in Canada using GRACE and GRACE-FO. *Science of The Total Environment*, *779*, 146435. https://doi.org/10.1016/j.scitotenv.2021.146435

Faunt, C. C. (Ed.) (2009), Groundwater availability of the Central Valley Aquifer, California, U.S. Geol. Surv. Prof. Pap., 1766, 225 pp.

Faunt, C. C., Sneed, M., Traum, J., & Brandt, J. T. (2016). Water availability and land subsidence in the Central Valley, California, USA. *Hydrogeology Journal*, *24*(3), 675-684. https://doi.org/ 10.1007/s10040-015-1339-x

Feng, W., Zhong, M., Lemoine, J. M., Biancale, R., Hsu, H. T., & Xia, J. (2013). Evaluation of groundwater depletion in North China using the Gravity Recovery and Climate Experiment (GRACE) data and ground-based measurements. *Water Resources Research*, *49*(4), 2110-2118. https://doi.org/10.1002/wrcr.20192

Fensholt, R., Sandholt, I., & Rasmussen, M. S. (2004). Evaluation of MODIS LAI, fAPAR and the relation between fAPAR and NDVI in a semiarid environment using in situ measurements. *Remote Sensing of Environment*, *91*, 490–507. https://doi.org/10.1016/j.rse.2004.04.009

Fiorillo, E., Crisci, A., Issa, H., Maracchi, G., Morabito, M., & Tarchiani, V. (2018). Recent changes of floods and related impacts in Niger based on the ANADIA Niger flood database. *Climate*, *6*(3), 59. https://doi.org/10.3390/cli6030059

Fisher, J. I., & Mustard, J. F. (2007). Cross-scalar satellite phenology from ground, Landsat, and MODIS data. *Remote Sensing of Environment*, *109*(3), 261–273. https://doi.org/10.1016/j.rse.2007.01.004

Fu, Y., Argus, D. F., & Landerer, F. W. (2015). GPS as an independent measurement to estimate terrestrial water storage variations in Washington and Oregon. *Journal of Geophysical Research: Solid Earth*, *120*(1), 552-566. https://doi.org/10.1002/2014JB011415

Gamon, J. A., Field, C. B., Goulden, M. L., Griffin, K. L., Hartley, A. E., Joel, G., ... & Valentini, R. (1995). Relationships between NDVI, canopy structure, and photosynthesis in three Californian vegetation types. *Ecological Applications*, *5*(1), 28-41. https://doi.org/10.2307/1942049

Gao, H., Tang, Q., Ferguson, C. R., Wood, E. F., & Lettenmaier, D. P. (2010). Estimating the water budget of major US river basins via remote sensing. *International Journal of Remote Sensing*, *31*(14), 3955-3978. https://doi.org/10.1080/01431161.2010.483488

Gebremichael, M., Krishnamurthy, P. K., Ghebremichael, L. T., & Alam, S. (2021). What Drives Crop Land Use Change during Multi-Year Droughts in California's Central Valley? Prices or Concern for Water? *Remote Sensing, 13*(4), 650. https://doi.org/10.3390/rs13040650

Gemitzi, A., Koutsias, N., & Lakshmi, V. (2021). A spatial downscaling methodology for GRACE Total water storage anomalies using GPM IMERG precipitation estimates. *Remote Sensing*, *13*(24), 5149. https://doi.org/10.3390/rs13245149

Gessner, U., Naeimi, V., Klein, I., Kuenzer, C., Klein, D., & Dech, S. (2013). The relationship between precipitation anomalies and satellite-derived vegetation activity in Central Asia. *Global and Planetary Change*, *110*, 74–87. https://doi.org/10.1016/j.gloplacha.2012.09.007

Ghasemizade, M., Asante, K. O., Petersen, C., Kocis, T., Dahlke, H. E., & Harter, T. (2019). An integrated approach toward sustainability via groundwater banking in the southern Central Valley, California. *Water Resources Research*, *55*(4), 2742-2759. https://doi.org/10.1029/2018WR024069

Gilbert, J. M., & Maxwell, R. M. (2018). Contrasting warming and drought in snowmelt-dominated agricultural basins: revealing the role of elevation gradients in regional response to temperature change. Environmental Research Letters, 13(7), 074023. https://doi.org/10.1088/1748-9326/aacb38

Girotto, M., G. J. M. De Lannoy, R. H. Reichle, & M. Rodell (2016). Assimilation of gridded terrestrial water storage observations from GRACE into a land surface model, *Water Resources Research*, *52*(5), 4164–4183. https://doi.org/10.1002/2015WR018417.

Gitelson, A. A. (2004). Wide dynamic range vegetation index for remote quantification of biophysical characteristics of vegetation. *Journal of plant physiology*, *161*(2), 165-173. https://doi.org/10.1078/0176-1617-01176

Gitelson, A. A., Viña, A., Arkebauer, T. J., Rundquist, D. C., Keydan, G., & Leavitt, B. (2003). Remote estimation of leaf area index and green leaf biomass in maize canopies. *Geophysical Research Letter*, 30(5), 1248. https://doi.org/10.1029/2002GL016450

Gitelson, A. A., Wardlow, B. D., Keydan, G. P., & Leavitt, B. (2007). An evaluation of MODIS 250-m data for green LAI estimation in crops. *Geophysical Research Letters*, *34*(20). https://doi.org/10.1029/2007GL031620

Gleeson, T., VanderSteen, J., Sophocleous, M. A., Taniguchi, M., Alley, W. M., Allen, D. M., & Zhou, Y. (2010). Commentary: Groundwater sustainability strategies. *Nature Geoscience*, *3*(6), 378. https://doi.org/10.1038/ngeo881

Gleick, P. H. (1993). World in crisis: A guide to the world's freshwater resources. New York: Oxford University Press.

Glenn, E. P., Huete, A. R., Nagler, P. L., & Nelson, S. G. (2008). Relationship between remotely sensed vegetation indices, canopy attributes & plant physiological processes: What vegetation indices can and cannot tell us about the landscape. *Sensors*, 8(4), 2136–2160. https://doi.org/10.3390/s8042136

Griebler, C., & Avramov, M. (2015). Groundwater ecosystem services: A review. *Freshwater Science*, *34*(1), 355-367. https://doi.org/10.1086/679903

Gu, Y., Hunt, E., Wardlow, B., Basara, J. B., Brown, J. F., & Verdin, J. P. (2008). Evaluation of MODIS NDVI and NDWI for vegetation drought monitoring using Oklahoma Mesonet soil

moisture data. *Geophysical Research Letters*, *35*(22), 1–5. https://doi.org/10.1029/2008GL035772

Gu, Z., Duan, X., Shi, Y., Li, Y., & Pan, X. (2018). Spatiotemporal variation in vegetation coverage and its response to climatic factors in the Red River Basin, China. *Ecological Indicators*, *93*(November 2017), 54–64. https://doi.org/10.1016/j.ecolind.2018.04.033

Guo, Y., Gan, F., Yan, B., Bai, J., Wang, F., Jiang, R., ... & Liu, Q. (2022). Evaluation of Groundwater Storage Depletion Using GRACE/GRACE Follow-On Data with Land Surface Models and Its Driving Factors in Haihe River Basin, China. *Sustainability*, *14*(3), 1108. https://doi.org/10.3390/su14031108

Gupta, H. V., Kling, H., Yilmaz, K. K., & Martinez, G. F. (2009). Decomposition of the mean squared error and NSE performance criteria: Implications for improving hydrological modelling. *Journal of hydrology*, *377*(1-2), 80-91. https://doi.org/10.1016/j.jhydrol.2009.08.003

Haboudane, D., Miller, J. R., Pattey, E., Zarco-Tejada, P. J., & Strachan, I. B. (2004). Hyperspectral vegetation indices and novel algorithms for predicting green LAI of crop canopies: Modeling and validation in the context of precision agriculture. *Remote sensing of environment*, *90*(3), 337-352. https://doi.org/10.1016/j.rse.2003.12.013

Hasan, E., Tarhule, A., & Kirstetter, P. E. (2021). Twentieth and twenty-first century water storage changes in the Nile river basin from grace/grace-fo and modeling. *Remote Sensing*, *13*(5), 953. https://doi.org/10.3390/rs13050953

Hayhoe, K., Cayan, D., Field, C. B., Frumhoff, P. C., Maurer, E. P., Miller, N. L., … Verville, J. H. (2004). Emissions pathways, climate change, and impacts on California. *Proceedings of*

the National Academy of Sciences of the United States of America, *101*(34), 12422–12427. https://doi.org/10.1073/pnas.0404500101

Henn, B., Newman, A. J., Livneh, B., Daly, C., & Lundquist, J. D. (2018). An assessment of differences in gridded precipitation datasets in complex terrain. *Journal of hydrology*, *556*, 1205-1219. https://doi.org/10.1016/j.jhydrol.2017.03.008

Herrmann, S. M., Didan, K., Barreto-Munoz, A., & Crimmins, M. A. (2016). Divergent responses of vegetation cover in Southwestern US ecosystems to dry and wet years at different elevations. *Environmental Research Letters*, *11*(12), 124005. https://doi.org/10.1088/1748-9326/11/12/124005.

Hoekstra, J. M., Molnar, J. L., Jennings, M., Revenga, C., Spalding, M. D., Boucher, T. M., ... & Ellison, K. (2010). *The atlas of global conservation: changes, challenges, and opportunities to make a difference* (pp. 1-272). Berkeley: University of California Press.

Hosseini, M., R. Magagi, & K. Goita (2013). Evaluation of random cascade hierarchical and statistical arrangement model in disaggregation of SMOS soil moisture, *AGU Fall Meeting Abstracts*.

Houborg, R., M. Rodell, B. Li, R. Reichle, & B. F. Zaitchik (2012). Drought indicators based on model-assimilated Gravity Recovery and Climate Experiment (GRACE) terrestrial water storage observations, *Water Resources Research*, *48*(7), https://doi.org/10.1029/2011WR011291, w07525.

Hu, Z., Zhou, Q., Chen, X., Chen, D., Li, J., Guo, M., ... & Duan, Z. (2019). Groundwater depletion estimated from GRACE: A challenge of sustainable development in an arid region of Central Asia. *Remote Sensing*, *11*(16), 1908. https://doi.org/10.3390/rs11161908

Huete, A. R. (2012). Vegetation indices, remote sensing and forest monitoring. *Geography Compass*, *6*(9), 513-532. https://doi.org/10.1111/j.1749-8198.2012.00507.x

Huete, A., Didan, K., Miura, T., & Rodriguez, E. (2002). Overview of the radiometric and biophysical performance of the MODIS vegetation indices. *Remote Sensing of Environment*, *83*, 195–213. https://doi.org/10.1016/S0034-4257(02)00096-2

Huete, A., Justice, C., & Van Leeuwen, W. (1999). MODIS vegetation index (MOD13). Algorithm theoretical basis document. *University of Arizona*. (Available online at *https://modis.gsfc.nasa.gov/data/atbd/atbd_mod13.pdf*)

Huntsinger, L., & Oviedo, J. L. (2014). Ecosystem services are social-ecological services in a traditional pastoral system: The case of California's mediterranean rangelands. *Ecology and Society*, *19*(1). https://doi.org/10.5751/ES-06143-190108

Ichii, K., Kawabata, A., & Yamaguchi, Y. (2002). Global correlation analysis for NDVI and climatic variables and NDVI trends: 1982-1990. *International Journal of Remote Sensing*, *23*(18), 3873–3878. https://doi.org/10.1080/01431160110119416

Jeong, H. G., Ahn, J. B., Lee, J., Shim, K. M., & Jung, M. P. (2020). Improvement of daily precipitation estimations using PRISM with inverse-distance weighting. *Theoretical and Applied Climatology*, *139*(3), 923-934. https://doi.org/10.1007/s00704-019-03012-6

Ji, W., M. Lin, A. Biswas, B. C. Si, H. W. Chau, and & H. P. Cresswell (2016). Fractal behavior of soil water storage at multiple depths, *Nonlinear Processes in Geophysics*, *23*, 269–284.

Jiao, Y., Lei, H., Yang, D., Huang, M., Liu, D., & Yuan, X. (2017). Impact of vegetation dynamics on hydrological processes in a semi-arid basin by using a land surface-hydrology coupled

model. *Journal of Hydrology, 551*, 116-131. https://doi.org/10.1016/j.jhydrol.2017.05.060

Kang, B., and & J. A. Ramirez (2010). A coupled stochastic space-time intermittent random cascade model for rainfall downscaling, *Water Resources Research*, *46*(10). https://doi.org/10.1029/2008WR007692, w10534.

Kang, Y., Özdoğan, M., Zipper, S. C., Román, M. O., Walker, J., Hong, S. Y., … Loheide, S. P. (2016). How universal is the relationship between remotely sensed vegetation indices and crop leaf area index? A global assessment. *Remote Sensing*, *8*(7). https://doi.org/10.3390/rs8070597

Kauffman, E. (2003). Climate and Topography. In *Atlas of Biodiversity of California* (pp. 12–15). Retrieved from https://www.coastal.ca.gov/coastalvoices/resources/Biodiversity_Atlas_Climate_and_Topography.pdf

Kaur, L., Rishi, M. S., & Chaudhary, B. S. (2022). Assessment of meteorological and agricultural droughts using remote sensing and their impact on groundwater in an agriculturally productive part of Northwest India. *Agricultural Water Management*, *274*, 107956. https://doi.org/10.1016/j.agwat.2022.107956

Kawabata, A., Ichii, K., & Yamaguchi, Y. (2001). Global monitoring of interannual changes in vegetation activities using NDVI and its relationships to temperature and precipitation. *International Journal of Remote Sensing*, *22*(7), 1377–1382. https://doi.org/10.1080/01431160119381

Kimura, S. D., Hatano, R., & Okazaki, M. (2009). Characteristics and issues related to regional-scale modeling of nitrogen flows. *Soil science and plant nutrition*, *55*(1), 1-12. https://doi.org/10.1111/j.1747-0765.2008.00353.x

Knyazikhin, Y., Glassy, J., Privette, J., Tian, Y., Lotsch, A., Zhang, Y., Wang, Y., Morisette, J., Votava, P., … Myneni, R. (1999). MODIS leaf area index (LAI) and fraction of photosynthetically active radiation absorbed by vegetation (Fpar) product (MOD15) algorithm theoretical basis document. *Theoretical Basis Document, NASA Goddard Space Flight Center*, Greenbelt, MD, 20771.

Kogan F. (2019) Vegetation Health Method. In: *Remote Sensing for Food Security. Sustainable Development Goals Series* (pp. 51-73). Springer, Cham. https://doi.org/10.1007/978-3-319-96256-6_4

Kogan, F., & Sullivan, J. (1993). Development of global drought-watch system using NOAA/AVHRR data. *Advances in Space Research*, *13*(5), 219-222. https://doi.org/10.1016/0273-1177(93)90548-P

Konikow, L. F. (2015). Long-term groundwater depletion in the United States. *Groundwater*, *53*(1), 2-9. https://doi.org/10.1111/gwat.12306

Konikow, L. F., and & E. Kendy (2005). Groundwater depletion: A global problem, *Hydrogeol J., 13*:317-320. https://doi.org/10.1007/s10040-004-0411-8.

Kottek, M., Grieser, J., Beck, C., Rudolf, B., & Rubel, F. (2006). World map of the Köppen-Geiger climate classification updated. *Meteorologische Zeitschrift*, *15*(3), 259–263. https://doi.org/10.1127/0941-2948/2006/0130

Kramer, K. (1999). The role of phenology for impact assessments of climate change on growth in boreal, temperate and Mediterranean forest ecosystems. *Management of Mixed-Species Forest: Silviculture and Economics.*, *IBN Scient*, 278–291.

Krogh, P. E., Andersen, O. B., Michailovsky, C. I., Bauer-Gottwein, P., Rowlands, D. D., Luthcke, S. B., & Chinn, D. S. (2010). Evaluating terrestrial water storage variations from regionally constrained GRACE mascon data and hydrological models over Southern Africa–preliminary results. *International Journal of Remote Sensing*, *31*(14), 3899-3912. https://doi.org/10.1080/01431161.2010.483483

Kuchment, L. S., and & A. N. Gelfan (2001), Statistical self-similarity of spatial variations of snow cover: verification of the hypothesis and application in the snowmelt runoff generation models, *Hydrological Processes*, *15*(18), 3343–3355. https://doi.org/10.1002/hyp.1032.

Kumar, S. V., B. F. Zaitchik, C. D. Peters-Lidard, M. Rodell, R. Reichle, B. Li, M. Jasinski, D. Mocko, A. Getirana, G. D. Lannoy, M. H. Cosh, C. R. Hain, M. Anderson, K. R. Arsenault, Y. Xia, and & M. Ek (2016), Assimilation of Gridded GRACE Terrestrial Water Storage Estimates in the North American Land Data Assimilation System, *Journal of Hydrometeorology*, *17*(7), 1951–1972. https://doi.org/10.1175/JHM-D-15-0157.1.

Kumari, N., Srivastava, A., & Dumka, U. C. (2021). A long-term spatiotemporal analysis of vegetation greenness over the Himalayan Region using Google Earth Engine. *Climate*, *9*(7), 109. https://doi.org/10.3390/cli9070109

Kuss, A. J., M. Newcomer, W.-C. Hsu, A. Bourai, A. Puranam, F. Landerer, and & C. Schmidt (2012). Downscaling GRACE Satellite Data for Small-scale Groundwater Storage Estimates in California's Central Valley, in *AGU Fall Meeting*, ED11A-0717.

Landerer, F. W., and & S. C. Swenson (2012). Accuracy of scaled GRACE terrestrial water storage estimates, *Water Resour. Res., 48*, W04531. https://doi.org/10.1029/2011WR011453.

Latinovic, M., Güntner, A., Flechtner, F., Murböck, M., and Kwas, A. (2021). Global flood monitoring with GRACE/GRACE-FO, *EGU General Assembly 2021*, online, 19–30 Apr 2021, EGU21-2683, https://doi.org/10.5194/egusphere-egu21-2683

Lenihan, J. M., Bachelet, D., Neilson, R. P., & Drapek, R. (2007). Response of vegetation distribution, ecosystem productivity, and fire to climate change scenarios for California. *Climatic Change*, *87*(1 SUPPL), 215–230. https://doi.org/10.1007/s10584-007-9362-0

Lenihan, J. M., Drapek, R., Bachelet, D., & Neilson, R. P. (2003). Climate change effects on vegetation distribution, carbon, and fire in California. *Ecological Applications*, *13*(6), 1667–1681. https://doi.org/10.1890/025295

Lhermitte, S., Verbesselt, J., Verstraeten, W. W., & Coppin, P. (2011). A comparison of time series similarity measures for classification and change detection of ecosystem dynamics. *Remote Sensing of Environment*, *115*(12), 3129–3152. https://doi.org/10.1016/j.rse.2011.06.020

Li, B., & Rodell, M. (2021). Groundwater drought: environmental controls and monitoring. In *Global Groundwater* (pp. 145-162). Elsevier. https://doi.org/10.1016/B978-0-12-818172-0.00011-6

Li, B., M. Rodell, B. F. Zaitchik, R. H. Reichle, R. D. Koster, and & T. M. van Dam (2012). Assimilation of GRACE terrestrial water storage into a land surface model: Evaluation and potential value for drought monitoring in western and central Europe, *Journal of*

Hydrology, *446-447*(Supplement C), 103 – 115. https://doi.org/10.1016/j.jhydrol.2012.04.035.

Li, D., Wrzesien, M. L., Durand, M., Adam, J., & Lettenmaier, D. P. (2017). How much runoff originates as snow in the western United States, and how will that change in the future?. *Geophysical Research Letters*, *44*(12), 6163-6172. https://doi.org/10.1002/2017GL073551

Lin, D., Gao, Y., Wu, Y., Shi, P., Yang, H., & Wang, J. (2017). A conversion method to determine the regional vegetation cover factor from standard plots based on large sample theory and TM images: A case study in the eastern farming-pasture ecotone of northern China. *Remote Sensing*, *9*(10), 1-20. https://doi.org/10.3390/rs9101035

Lin, Y., Xin, X., Zhang, H., & Wang, X. (2015). The implications of serial correlation and time-lag effects for the impact study of climate change on vegetation dynamics – a case study with Hulunber meadow steppe, Inner Mongolia. *International Journal of Remote Sensing*, *36*(19–20), 5031–5044. https://doi.org/10.1080/01431161.2015.1093196

Liu, F., Kang, P., Zhu, H., Han, J., & Huang, Y. (2021). Analysis of Spatiotemporal Groundwater-Storage Variations in China from GRACE. *Water*, *13*(17), 2378. https://doi.org/10.3390/w13172378

Liu, H., Yuan, X., & Zhang, M. (2022). Unraveling human influence on evapotranspiration over East Asian monsoon river basins by using GRACE/GRACE-FO data and land surface models. *Journal of Hydrology*, *605*, 127349. https://doi.org/10.1016/j.jhydrol.2021.127349

Liu, Y., Hill, M. J., Zhang, X., Wang, Z., Richardson, A. D., Hufkens, K., … Schaaf, C. B. (2017). Using data from Landsat, MODIS, VIIRS and PhenoCams to monitor the phenology of California oak/grass savanna and open grassland across spatial scales. *Agricultural and Forest Meteorology*, *237–238*, 311–325. https://doi.org/10.1016/j.agrformet.2017.02.026

Livingston, M. L., and & A. Garrido (2004). Entering the policy debate: An economic evaluation of groundwater policy in flux, *Water Resour. Res., 40*, W12S02. https://doi.org/10.1029/2003WR002737.

Longuevergne, L., Scanlon, B. R., and & Wilson, C. R. (2010). GRACE Hydrological estimates for small basins: Evaluating processing approaches on the high plains aquifer, USA. *Water Resources Research*, *46*(11), W11517. https://doi.org/10.1029/2009WR008564

Lytton, L., Ali, A., Garthwaite, B., Punthakey, J. F., & Saeed, B. (2021). Groundwater in Pakistan's Indus Basin.

Ma, N., & Szilagyi, J. (2019). The CR of evaporation: A calibration-free diagnostic and benchmarking tool for large-scale terrestrial evapotranspiration modeling. *Water Resources Research, 55(8)*, 7246-7274. https://doi.org/10.1029/2019WR024867

Maeda, E. E., H. Kim, L. E. O. C. AragÃčo, J. S. Famiglietti, and & T. Oki (2015), Disruption of hydroecological equilibrium in southwest Amazon mediated by drought, *Geophys. Res. Lett.*, *42*(18), 7546–7553, https://doi.org/10.1002/2015GL065252, 2015GL065252.

Mao, D., Wang, Z., Luo, L., & Ren, C. (2012). Integrating AVHRR and MODIS data to monitor NDVI changes and their: Relationships with climatic parameters in Northeast China.

International Journal of Applied Earth Observation and Geoinformation, *18*(1), 528–536. https://doi.org/10.1016/j.jag.2011.10.007

Martiny, N., Camberlin, P., Richard, Y., & Philippon, N. (2006). Compared regimes of NDVI and rainfall in semiarid regions of Africa. *International Journal of Remote Sensing*, *27*(23), 5201–5223. https://doi.org/10.1080/01431160600567787

Martiny, N., Richard, Y., & Camberlin, P. (2005). Interannual persistence effects in vegetation dynamics of semiarid Africa. *Geophysical Research Letters*, *32*(24), 1–4. https://doi.org/10.1029/2005GL024634

Mascaro, G., E. R. Vivoni, and & R. Deidda (2010). Downscaling soil moisture in the southern great plains through a calibrated multifractal model for land surface modeling applications, *Water Resources Research*, *46*(8). https://doi.org/10.1029/2009WR008855,w08546.

Mascaro, G., Ko, A., & Vivoni, E. R. (2019). Closing the loop of satellite soil moisture estimation via scale invariance of hydrologic simulations. *Scientific reports*, *9*(1), 1-8. https://doi.org/10.1038/s41598-019-52650-3

McGrath, G. S., Sadler, R., Fleming, K., Tregoning, P., Hinz, C., & Veneklaas, E. J. (2012). Tropical cyclones and the ecohydrology of Australia's recent continental-scale drought. *Geophysical Research Letter,* 39(3), 1-6. https://doi.org/10.1029/2011GL050263, l03404

Menabde, M. (1998). Bounded lognormal cascades as quasi-multiaffine random processes. *Non-linear processes in geophysics, 5*(2). 63-68. https://doi.org/10.5194/npg-5-63-1998.

Miguez-Macho, G., & Fan, Y. (2012). The role of groundwater in the Amazon water cycle: 1. Influence on seasonal streamflow, flooding and wetlands. *Journal of Geophysical Research: Atmospheres*, *117*(D15). https://doi.org/10.1029/2012JD017539

Mo, S., Zhong, Y., Forootan, E., Shi, X., Feng, W., Yin, X., & Wu, J. (2022). Hydrological droughts of 2017-2018 explained by the Bayesian reconstruction of GRACE (-FO) fields. *Water Resources Research*, e2022WR031997. https://doi.org/10.1029/2022WR031997

Mohamad, N., Ahmad, A., & Din, A. H. M. (2020). Monitoring Groundwater Depletion Due to Drought using Satellite Gravimetry: A Review. In *IOP Conference Series: Earth and Environmental Science* (Vol. 540, No. 1, p. 012054). IOP Publishing. http://dx.doi.org/10.1088/1755-1315/540/1/012054

Molnar, P., and & P. Burlando (2005), Preservation of rainfall properties in stochastic disaggregation by a simple random cascade model, *Atmospheric Research*, *77*(1), 137 – 151. https://doi.org/10.1016/j.atmosres.2004.10.024, precipitation in Urban Areas.

Mooney, H., & Zavaleta, E. (Eds.). (2016). Ecosystems of California. In *Ecosystems of California*.

Moore, N., Arima, E., Walker, R., & Ramos da Silva, R. (2007). Uncertainty and the changing hydroclimatology of the Amazon. *Geophysical Research Letters*, *34*(14). https://doi.org/10.1029/2007GL030157

Mu, Q., Zhao, M., and & Running, S. W. (2011). Improvements to a MODIS global terrestrial evapotranspiration algorithm. *Remote Sensing of Environment*, *115*(8), 1781 – 1800. https://doi.org/10.1016/j.rse.2011.02.019

Myneni, R., Hoffman, S., Knyazikhin, Y., Privette, J., Glassy, J., Tian, Y., Wang, Y., Song, X., Zhang, Y., Smith, G., Lotsch, A., Friedl, M., Morisette, J., Votava, P., Nemani, R., & Running, S.

(2002). Global products of vegetation leaf area and fraction absorbed par from year one of MODIS data. *Remote Sensing of Environment*, 83(1), 214 – 231, doi: https://dx.doi.org/10.1016/S0034-4257(02)00074-3

Nair, A. S., & Indu, J. (2020). Changing groundwater storage trend of India after severe drought. *International Journal of Remote Sensing*, *41*(19), 7565-7584. https://doi.org/10.1080/01431161.2020.1763503

Nash, J. and & Sutcliffe, J. (1970). River flow forecasting through conceptual models part I – A discussion of principles. *Journal of Hydrology, 10*(3), 282 – 290. https://doi.org/10.1016/0022-1694(70)90255-6

Neuhauser, M., Verrier, S., Merlin, O., Molero, B., Suere, C., & Mangiarotti, S. (2019). Multi-scale statistical properties of disaggregated SMOS soil moisture products in Australia. *Advances in Water Resources*, *134*, 103426. https://doi.org/10.1016/j.advwatres.2019.103426

Nicholson, Sharon, Davenport, Michael, and & Malo, A. (1990). A Comparison of the Vegetation Response to Rainfall in the Sahel and East Africa, Using Normalized Difference Vegetation Index from NOAA AVHRR. *Climatic Change*, *17,* 209–241. https://doi.org/10.1007/BF00138369

Nigatu, Z. M., Fan, D., You, W., & Melesse, A. M. (2021). Hydroclimatic extremes evaluation using GRACE/GRACE-FO and multidecadal climatic variables over the Nile river basin. *Remote Sensing*, *13*(4), 651. https://doi.org/10.3390/rs13040651

Nightingale, J. M., & Phinn, S. R. (2003). Assessment of Relationships between Precipitation Environments of South Australia. *Australian Geographical Studies*, *41*(July), 180–195. https://doi.org/10.1111/1467-8470.00204

Ning, S., H. Ishidaira, and & J. Wang (2014). Statistical downscaling of GRACE-derived terrestrial water storage using satellite and GLDAS products, *Journal of Japan Society of Civil Engineers, Ser. B1 (Hydraulic Engineering)*, *70*(4).

Olden, J. D., & Ne, B. D. (2001). Cross-correlation bias in lag analysis of aquatic time series. *Marine Biology*, *138*(December 2000), 1063–1070. https://doi.org/10.1007/s002270000517

Ouma, Y. O., Aballa, D. O., Marinda, D. O., Tateishi, R., & Hahn, M. (2015). Use of GRACE time-variable data and GLDAS-LSM for estimating groundwater storage variability at small basin scales: a case study of the Nzoia River Basin. *International Journal of Remote Sensing*, *36*(22), 5707-5736. https://doi.org/10.1080/01431161.2015.1104743

Over, T. M. (1995). Modeling space-time rainfall at the mesoscale using random cascades. Ph.D. Dissertation. University of Colorado at Boulder.

Over, T. M., and & V. K. Gupta (1996). A space-time theory of mesoscale rainfall using random cascades, *Journal of Geophysical Research: Atmospheres*, *101*(D21), 26,319–26,331. https://doi.org/10.1029/96JD02033.

Owor, M. (2010). Groundwater – surface water interactions on deeply weathered surfaces on low relief in the Upper Nile Basin of Uganda, PhD Dissertation, University College London.

Paiva, R. C., Collischonn, W., & Buarque, D. C. (2013). Validation of a full hydrodynamic model for large-scale hydrologic modelling in the Amazon. *Hydrological Processes*, *27*(3), 333-346. https://doi.org/10.1002/hyp.8425

Pascolini-Campbell, M., Fisher, J. B., & Reager, J. T. (2021). GRACE-FO and ECOSTRESS Synergies Constrain Fine-Scale Impacts on the Water Balance. *Geophysical Research Letters*, *48*(15), e2021GL093984. https://doi.org/10.1029/2021GL093984

Pokhrel, Y. N., Fan, Y., Miguez-Macho, G., Yeh, P. J. F., & Han, S. C. (2013). The role of groundwater in the Amazon water cycle: 3. Influence on terrestrial water storage computations and comparison with GRACE. *Journal of Geophysical Research: Atmospheres*, *118*(8), 3233-3244. https://doi.org/10.1002/jgrd.50335

Pons, V., Benestad, R., Sivertsen, E., Muthanna, T. M., & Bertrand-Krajewski, J. L. (2022). Forecasting green roof detention performance by temporal downscaling of precipitation time-series projections. *Hydrology and Earth System Sciences*, *26*(11), 2855-2874. https://doi.org/10.5194/hess-26-2855-2022, 2022

Posadas, A., Duffaut Espinosa, L. A., Yarlequé, C., Carbajal, M., Heidinger, H., Carvalho, L., ... & Quiroz, R. (2015). Spatial random downscaling of rainfall signals in Andean heterogeneous terrain. *Nonlinear Processes in Geophysics*, *22*(4), 383-402. https://doi.org/10.5194/npg-22-383-2015

Probst, W. N., Stelzenmuller, V., & Fock, H. O. (2012). Using cross-correlations to assess the relationship between time-lagged pressure and state indicators: an exemplary analysis of North Sea fish population indicators Wolfgang. *ICES Journal of Marine Science*, *69*(4), 670–681. https://doi.org/10.4135/9781412953924.n678

Pu, L., Fan, D., You, W., Yang, X., Nigatu, Z. M., & Jiang, Z. (2022). Extracting terrestrial water storage signals from GRACE solutions in the Amazon Basin using an iterative filtering approach. *Remote Sensing Letters*, *13*(1), 14-23. https://doi.org/10.1080/2150704X.2021.1981557

Qiao, L., R. B. Herrmann, and & Z. Pan (2013). Parameter uncertainty reduction for SWAT using GRACE, streamflow, and groundwater table data for lower Missouri River Basin, *JAWRA Journal of the American Water Resources Association*, *49*(2), 343–358. https://doi.org/10.1111/jawr.12021.

Reager, J. T., and & J. S. Famiglietti (2009). Global terrestrial water storage capacity and flood potential using GRACE, *Geophysical Research Letters*, *36*(23). https://doi.org/10.1029/2009GL040826, l23402.

Reager, J., B. Thomas, and & J. Famiglietti (2014). River basin flood potential inferred using GRACE gravity observations at several months lead time, *Nature Geoscience*, pp. 588–592. https://doi.org/10.1038/ngeo2203

Reichenau, T. G., Korres, W., Montzka, C., & Fiener, P. (2016). Spatial Heterogeneity of Leaf Area Index (LAI) and Its Temporal Course on Arable Land: Combining Field Measurements, Remote Sensing and Simulation in a Comprehensive Data Analysis Approach (CDAA). *PLOS One*, 1–24. https://doi.org/10.1371/journal.pone.0158451

Richard, Y., & Poccard, I. (1998). A statistical study of NDVI sensitivity to seasonal and interannual rainfall variations in Southern Africa. *International Journal of Remote Sensing*, *19*(15), 2907–2920. https://doi.org/10.1080/014311698214343

Richey, A. S., B. F. Thomas, M.-H. Lo, J. S. Famiglietti, S. Swenson, and & M. Rodell (2015a). Uncertainty in global groundwater storage estimates in a Total Groundwater Stress framework, *Water Resources Research*, *51*(7), 5198–5216. https://doi.org/10.1002/2015WR017351.

Richey, A. S., B. F. Thomas, M.-H. Lo, J. T. Reager, J. S. Famiglietti, K. Voss, S. Swenson, and M. Rodell (2015b). Quantifying renewable groundwater stress with GRACE, *Water Resources Research*, *51*(7), 5217–5238. https://doi.org/10.1002/2015WR017349.

Rodell, M., Chen, J., Kato, H., Famiglietti, J. S., Nigro, J., & Wilson, C. R. (2007). Estimating groundwater storage changes in the Mississippi River basin (USA) using GRACE. *Hydrogeology Journal*, *15*(1), 159-166. https://doi.org/10.1007/s10040-006-0103-7

Rodell, M., Famiglietti, J. S., Chen, J., Seneviratne, S. I., Viterbo, P., Holl, S., & Wilson, C. R. (2004). Basin scale estimates of evapotranspiration using GRACE and other observations. *Geophysical Research Letters*, *31*(20). https://doi.org/10.1029/2004GL020873

Rodell, M., Houser, P. R., Jambor, U., Gottschalck, J., Mitchell, K., Meng, C.-J., Arsenault, K., Cosgrove, B., Radakovich, J., Bosilovich, M., Entin*, J. K., Walker, J. P., Lohmann, D., and & Toll, D. (2004). The Global Land Data Assimilation System. *Bulletin of the American Meteorological Society*, *85*(3), 381–394. https://doi.org/10.1175/BAMS-85-3-381

Rodell, M., I. Velicogna, and & J. S. Famiglietti (2009). Satellite‐based estimates of groundwater depletion in India, *Nature, 460*, 999–1002. https://doi.org/10.1038/nature08238.

Rouse, J. W., Haas, R. H., Schell, J. A., & Deering, D. W. (1974). Monitoring vegetation systems in the great plains with ERTS, *3rd ERTS-1 Symposium*, vol. 1, pp. 309–317, NASA, Washington, D. C.

Rupp, D. E., P. Licznar, W. Adamowski, and & M. Leśniewski (2012). Multiplicative cascade models for fine spatial downscaling of rainfall: parameterization with rain gauge data, *Hydrology and Earth System Sciences*, *16*(3), 671–684. https://doi.org/10.5194/hess-16-671-2012.

Russo, T., Lall, U.,Wen, H., and& Williams,M. (2014). Assessment of trends in groundwater levels across the United States. *Columbia Water Center*.

Sakumura, C., Bettadpur, S., and & Bruinsma, S. (2014). Ensemble prediction and intercomparison analysis of GRACE time-variable gravity field models. *Geophysical Research Letters, 41*(5), 1389–1397. https://doi.org/10.1002/2013GL058632

Samanta, A., Knyazikhin, Y., Xu, L., Dickinson, R. E., Fu, R., Costa, M. H., ... & Myneni, R. B. (2012). Seasonal changes in leaf area of Amazon forests from leaf flushing and abscission. *Journal of Geophysical Research: Biogeosciences, 117*(G1). https://doi.org/10.1029/2011JG001818

Save, H., Bettadpur, S., & Tapley, B. D. (2016). High-resolution CSR GRACE RL05 mascons. *Journal of Geophysical Research: Solid Earth*, *121*(10), 7547-7569. https://doi.org/10.1002/2016JB013007

Scanlon, B. R., Faunt, C. C., Longuevergne, L., Reedy, R. C., Alley, W. M., McGuire, V. L., & McMahon, P. B. (2012). Groundwater depletion and sustainability of irrigation in the US

High Plains and Central Valley. *Proceedings of the national academy of sciences*, *109*(24), 9320-9325. https://doi.org/10.1073/pnas.1200311109

Scanlon, B. R., L. Longuevergne, and & D. Long (2012). Ground referencing GRACE satellite estimates of groundwater storage changes in the California Central Valley, USA, *Water Resour. Res., 48*, W04520. https://doi.org/10.1029/2011WR011312.

Scanlon, B. R., Zhang, Z., Save, H., Wiese, D. N., Landerer, F. W., Long, D., Longuevergne, L., and & Chen, J. (2016). Global evaluation of new GRACE mascon products for hydrologic applications. *Water Resources Research, 52*, 9412– 9429. https://doi.org/10.1002/2016WR019494.

Schertzer, D., & Lovejoy, S. (1987). Physical modeling and analysis of rain and clouds by anisotropic scaling multiplicative processes. *Journal of Geophysical Research: Atmospheres*, *92*(D8), 9693-9714. https://doi.org/10.1029/JD092iD08p09693

Seo, J. Y., & Lee, S. I. (2016). Integration of GRACE, ground observation, and land-surface models for groundwater storage variations in South Korea. *International Journal of Remote Sensing*, *37*(24), 5786-5801. https://doi.org/10.1080/01431161.2016.1249301

Seyoum, W. M., Kwon, D., & Milewski, A. M. (2019). Downscaling GRACE TWSA data into high-resolution groundwater level anomaly using machine learning-based models in a glacial aquifer system. *Remote Sensing*, *11*(7), 824. https://doi.org/10.3390/rs11070824

Shah T, Molden D, Sakthivadivel R, & Seckler D (2000). The global groundwater situation: overview of opportunities and challenges. International Water Management Institute.

Sharifi, E., Güntner, A., Haas, J., Dorigo, W., Jäggi, A., Ruz Vargas, C., ... & Zemp, M. (2022). A Global Gravity-based Groundwater Product (G3P). In *Living Planet Symposium 2022-European Space Agency (ESA)*.

Sharma, D., Patnaik, S., Biswal, B., & Reager, J. T. (2020). Characterization of basin-scale dynamic storage–discharge relationship using daily GRACE based storage anomaly data. *Geosciences*, *10*(10), 404. https://doi.org/10.3390/geosciences10100404

Somers, L. D., & McKenzie, J. M. (2020). A review of groundwater in high mountain environments. *Wiley Interdisciplinary Reviews: Water*, *7*(6), e1475. https://doi.org/10.1002/wat2.1475

Strassberg, G., B. R. Scanlon, and & M. Rodell (2007). Comparison of seasonal terrestrial water storage variations from GRACE with groundwater-level measurements from the High Plains Aquifer (USA), *Geophys. Res. Lett., 34*, L14402. https://doi.org/10.1029/2007GL030139.

Sun, A. Y. (2013). Predicting groundwater level changes using GRACE data, *Water Resour. Res., 49*. https://doi.org/10.1002/wrcr.20421.

Sun, A. Y., R. Green, M. Rodell, and & S. Swenson (2010). Inferring aquifer storage parameters using satellite and in situ measurements: Estimation under uncertainty, *Geophysical Research Letters*, *37*(10). https://doi.org/10.1029/2010GL043231, l10401.

Sun, A. Y., R. Green, S. Swenson, and & M. Rodell (2012). Toward calibration of regional groundwater models using GRACE data, *Journal of Hydrology*, *422-423* (Supplement C), 1 – 9. https://doi.org/10.1016/j.jhydrol.2011.10.025.

Sun, J., Hu, L., Liu, X., & Sun, K. (2022). Enhanced Understanding of Groundwater Storage Changes under the Influence of River Basin Governance Using GRACE Data and Downscaling Model. *Remote Sensing*, *14*(19), 4719. https://doi.org/10.3390/rs14194719

Swenson, S. and & Wahr, J. (2002). Methods for inferring regional surface-mass anomalies from gravity recovery and climate experiment (GRACE) measurements of time-variable gravity. *Journal of Geophysical Research: Solid Earth*, *107*(B9), ETG 3–1–ETG 3–13 2193. https://doi.org/10.1029/2001JB000576

Swenson, S. C. (2012). GRACE monthly land water mass grids NETCDF RELEASE 5.0. Ver. 5.0. PO.DAAC, CA, USA. Dataset accessed [2013-08-15] at http://dx.doi.org/10.5067/TELND-NC005.

Swenson, S. C., & Wahr, J. M. (2011). Estimating signal loss in regularized GRACE gravity field solutions. *Geophysical Journal International*, *185*(2), 693-702. https://doi.org/10.1111/j.1365-246X.2011.04977.x

Swenson, S. and& Wahr, J. (2006). Post-processing removal of correlated errors in GRACE data. *Geophysical Research Letters*, *33*(8), L08402. https://doi.org/10.1029/2005GL025285

Syed, T. H., J. S. Famiglietti, M. Rodell, J. Chen, and & C. R. Wilson (2008). Analysis of terrestrial water storage changes from GRACE and GLDAS, *Water Resources Research*, *44*(2). https://doi.org/10.1029/2006WR005779, w02433.

Szilagyi, J., Crago, R., & Qualls, R. (2017). A calibration-free formulation of the complementary relationship of evaporation for continental-scale hydrology. *Journal of Geophysical Research: Atmospheres, 122(1)*, 264-278. http:// doi:10.1002/2016JD025611

Talib, M. A., Tang, Z., Shahab, A., Siddique, J., Faheem, M., & Fatima, M. (2019). Hydrogeochemical characterization and suitability assessment of groundwater: a case study in Central Sindh, Pakistan. *International journal of environmental research and public health*, *16*(5), 886. https://doi.org/10.3390/ijerph16050886

Tangdamrongsub, N., & Šprlák, M. (2021). The assessment of hydrologic-and flood-induced land deformation in data-sparse regions using GRACE/GRACE-FO data assimilation. *Remote Sensing*, *13*(2), 235. https://doi.org/10.3390/rs13020235

Tangdamrongsub, N., Hwang, C., Borak, J. S., Prabnakorn, S., & Han, J. (2021). Optimizing GRACE/GRACE-FO data and a priori hydrological knowledge for improved global terrestial water storage component estimates. *Journal of Hydrology*, *598*, 126463. https://doi.org/10.1016/j.jhydrol.2021.126463

Tapley, B. D., S. Bettadpur, J. C. Ries, P. F. Thompson, and & M. M. Watkins (2004a). GRACE Measurements of Mass Variability in the Earth System, *Science*, *305*(5683), 503–505. https://doi.org/10.1126/science.1099192.

Tapley, B. D., S. Bettadpur, M. Watkins, and & C. Reigber (2004b). The gravity recovery and climate experiment: Mission overview and early results, *Geophysical Research Letters*, *31*(9). https://doi.org/10.1029/2004GL019920, l09607.

Tardy, Y., Mortatti, J., Victoria, R., Martinelli, L., Ribeiro, A., Cerri, C., ... & Volkoff, B. (1993). Hydroclimatology and biogeochemistry of the Amazon: 1. Erosion. *Chemical geology*, *107*(3-4), 333-336. https://doi.org/10.1016/0009-2541(93)90203-U

Tchiguirinskaia, I., Lu, S., Molz, F. J., Williams, T. M., & Lavallee, D. (2000). Multifractal versus monofractal analysis of wetland topography. *Stochastic Environmental Research and Risk Assessment, 14*(1), 8-32. https://doi.org/10.1007/s004770050002

Tesemma, Z. K., Wei, Y., Western, A. W., & Peel, M. C. (2014). Leaf area index variation for crop, pasture, and tree in response to climatic variation in the Goulburn–Broken catchment, Australia. Journal of Hydrometeorology, 15(4), 1592-1606. https://doi.org/10.1175/JHM-D-13-0108.1

Tesfaye, A. A., & Awoke, B. G. (2021). Evaluation of the saturation property of vegetation indices derived from sentinel-2 in mixed crop-forest ecosystem. *Spatial Information Research, 29*(1), 109-121. https://doi.org/10.1007/s41324-020-00339-5.

Thomas, A. C., J. T. Reager, J. S. Famiglietti, and M. Rodell (2014). A GRACE-based water storage deficit approach for hydrological drought characterization, *Geophysical Research Letters*, *41*(5), 1537–1545. https://doi.org/10.1002/2014GL059323, 2014GL059323.

Trumbore, S., Brando, P., & Hartmann, H. (2015). Forest health and global change. *Science*, *349*(6250), 814-818. https://doi.org/10.1126/science.aac6759

Tucker, C. J. (1979). Red and photographic infrared linear combinations for monitoring vegetation. *Remote sensing of Environment*, *8*(2), 127-150. https://doi.org/10.1016/0034-4257(79)90013-0

Ukasha, M., Ramirez, J. A., & Niemann, J. D. (2022). An improved rescaling algorithm for estimating groundwater depletion rates using the GRACE satellite. Article submitted to *International Journal of Remote Sensing*.

Ukasha, M., Ramirez, J. A., & Niemann, J. D. (2022). Temporal Variations of NDVI and LAI and Interactions with Hydroclimatic Variables in a Large and Agro-Ecologically Diverse Region. Journal of Geophysical Research: Biogeosciences, 127(4), e2021JG006395. https://doi.org/10.1029/2021JG006395

Urióstegui, S. H., Bibby, R. K., Esser, B. K., & Clark, J. F. (2017). Quantifying annual groundwater recharge and storage in the central Sierra Nevada using naturally occurring 35S. *Hydrological Processes*, *31*(6), 1382-1397. https://doi.org/10.1002/hyp.11112

USGS (2014). Real-Time Water Data for the Nation: Daily Streamflow Conditions, National Water Information System (NWIS), <http://waterdata.usgs.gov/nwis/rt>.

Velicogna, I., & Wahr, J. (2006). Measurements of time-variable gravity show mass loss in Antarctica. Science, 311(5768), 1754-1756. https://doi.org/ 10.1126/science.1123785

Veneziano, D., Bras, R. L., & Niemann, J. D. (1996). Nonlinearity and self-similarity of rainfall in time and a stochastic model. *Journal of Geophysical Research: Atmospheres*, *101*(D21), 26371-26392. https://doi.org/10.1029/96JD01658

Verger, A., Filella, I., Baret, F., & Peñuelas, J. (2016). Vegetation baseline phenology from kilometric global LAI satellite products. *Remote Sensing of Environment*, *178*, 1–14. https://doi.org/10.1016/j.rse.2016.02.057. https://doi.org/10.1016/j.rse.2011.08.010

Verrier, S. (2020). Multifractal and multiscale entropy scaling of in-situ soil moisture time series: Study of SMOSMANIA network data, southwestern France. *Journal of Hydrology*, *585*, 124821. https://doi.org/10.1016/j.jhydrol.2020.124821

Wada, Y., L. P. H. van Beek, C. M. van Kempen, J. W. T. M. Reckman, S. Vasak, and M. F. P. Bierkens (2010). Global depletion of groundwater resources, *Geophys. Res. Lett., 37*, L20402. https://doi.org/10.1029/2010GL044571.

Wahr, J., M. Molenaar, and F. Bryan (1998). Time variability of the Earth's gravity field: Hydrological and oceanic effects and their possible detection using GRACE, *J. Geophys. Res., 103*, 30,205-30,229. https://doi.org/10.1029/98JB02844

Wang, Q., Adiku, S., Tenhunen, J., & Granier, A. (2005). On the relationship of NDVI with leaf area index in a deciduous forest site. *Remote Sensing of Environment*, 94(2), 244 – 255, https://doi.org/10.1016/j.rse.2004.10.006.

Wang, T., Xiao, Z., & Liu, Z. (2017). Performance Evaluation of Machine Learning Methods for Leaf Area Index Retrieval from Time-Series MODIS Reflectance Data. *Sensors*, *17(1)*, 81. https://doi.org/10.3390/s17010081

Xanke, J., & Liesch, T. (2022). Quantification and possible causes of declining groundwater resources in the Euro-Mediterranean region from 2003 to 2020. *Hydrogeology Journal*, *30*(2), 379-400. https://doi.org/10.1007/s10040-021-02448-3

Xiao, M., Koppa, A., Mekonnen, Z., Pagán, B. R., Zhan, S., Cao, Q., ... & Lettenmaier, D. P. (2017). How much groundwater did California's Central Valley lose during the 2012–2016 drought? *Geophysical Research Letters, 44*(10), 4872-4879. https://doi.org/10.1002/2017GL073333w

Xiong, J., Yin, J., Guo, S., Yin, W., Rao, W., & Chao, N. (2022). Using GRACE to detect groundwater variation in North China Plain after south-north water diversion. *Groundwater*. https://doi.org/10.1111/gwat.13253

Xu, D., An, D., & Guo, X. (2020). The impact of non-photosynthetic vegetation on LAI estimation by NDVI in mixed grassland. *Remote Sensing, 12*(12), 1979. https://doi.org/10.3390/rs12121979

Xu, L., Myneni, R. B., Chapin, F. S., Callaghan, T. V., Pinzon, J. E., Tucker, C. J., Stroeve, J. C. (2013). Temperature and vegetation seasonality diminishment over northern lands. *Nature Climate Change*, *3*(6), 581–586. https://doi.org/10.1038/nclimate1836

Xue, J., & Su, B. (2017). Significant Remote Sensing Vegetation Indices: A Review of Developments and Applications. *Journal of Sensors*, *2017*. https://doi.org/10.1155/2017/1353691

Xue, J., Wang, Y., Teng, H., Wang, N., Li, D., Peng, J., ... & Shi, Z. (2021). Dynamics of Vegetation Greenness and Its Response to Climate Change in Xinjiang over the Past Two Decades. *Remote Sensing*, *13*(20), 4063. https://doi.org/10.3390/rs13204063

Yang, D., Shao, W., Yeh, P. J. F., Yang, H., Kanae, S., & Oki, T. (2009). Impact of vegetation coverage on regional water balance in the non humid regions of China. *Water Resources Research*, *45*(7), 1–13. https://doi.org/10.1029/2008WR006948

Yang, L., Jin, S., Danielson, P., Homer, C., Gass, L., Bender, S. M., Xian, G. (2018). A new generation of the United States National Land Cover Database: Requirements, research priorities, design, and implementation strategies. *ISPRS Journal of Photogrammetry and Remote Sensing*, *146*(September), 108–123. https://doi.org/10.1016/j.isprsjprs.2018.09.006

Yang, P., Zhan, C., Xia, J., Han, J., & Hu, S. (2018). Analysis of the spatiotemporal changes in terrestrial water storage anomaly and impacting factors over the typical mountains in

China. *International Journal of Remote Sensing*, *39*(2), 505-524. https://doi.org/10.1080/01431161.2017.1388939

Yang, W., Yang, L., & Merchant, J. W. (1997). An assessment of AVHRR/NDVI-ecoclimatological relations in Nebraska, U.S.A. *International Journal of Remote Sensing*, *18*(10), 2161–2180. https://doi.org/10.1080/014311697217819

Yang, Y., D. Long, H. Guan, B. R. Scanlon, C. T. Simmons, L. Jiang, and X. Xu (2014). GRACE satellite observed hydrological controls on interannual and seasonal variability in surface greenness over mainland Australia, J. *Geophys. Res. Biogeosci., 119*, 2245–2260. https://doi.org/10.1002/2014JG002670.

Yang, Z., Dominguez, F., Zeng, X., Hu, H., Gupta, H., & Yang, B. (2017). Impact of irrigation over the California Central Valley on regional climate. *Journal of Hydrometeorology*, *18*(5), 1341–1357. https://doi.org/10.1175/JHM-D-16-0158.1

Yeh, P. J.-F., Swenson, S. C., Famiglietti, J. S., and Rodell, M. (2006). Remote sensing of groundwater storage changes in Illinois using the gravity recovery and climate experiment (GRACE). *Water Resources Research, 42*(12) W12203. https://doi.org/10.1029/2006WR005374

Yi, S., Wang, Q., & Sun, W. (2016). Basin mass dynamic changes in China from GRACE based on a multi basin inversion method. *Journal of Geophysical Research: Solid Earth*, *121*(5), 3782-3803. https://doi.org/10.1002/2015JB012608

Yin, W., Zhang, G., Han, S. C., Yeo, I. Y., & Zhang, M. (2022). Improving the resolution of GRACE-based water storage estimates based on machine learning downscaling schemes. *Journal of Hydrology*, 128447. https://doi.org/10.1016/j.jhydrol.2022.128447

Yin, W., Zhang, G., Han, S. C., Yeo, I. Y., & Zhang, M. (2022). Improving the resolution of GRACE-based water storage estimates based on machine learning downscaling schemes. *Journal of Hydrology*, 128447. https://doi.org/10.1016/j.jhydrol.2022.128447

Yirdaw, S. Z., and K. R. Snelgrove (2011). Regional Groundwater Storage from GRACE over the Assiniboine Delta Aquifer (ADA) of Manitoba, *Atmosphere-Ocean*, *49*(4), 396–407. https://doi.org/10.1080/07055900.2011.623915.

Zaitchik, B. F., M. Rodell, and R. H. Reichle (2008). Assimilation of GRACE terrestrial water storage data into a land surface model: Results for the Mississippi River Basin, *J Hydrometeorology, 9*, 535-548. https://doi.org/10.1175/2007JHM951.1.

Zhang, P., Anderson, B., Barlow, M., Tan, B., & Myneni, R. B. (2004). Climate-related vegetation characteristics derived from Moderate Resolution Imaging Spectroradiometer (MODIS) leaf area index and normalized difference vegetation index. *Journal of Geophysical Research*, *109*(D20105). https://doi.org/10.1029/2004JD004720

Zhang, X., Friedl, M. A., & Schaaf, C. B. (2006). Global vegetation phenology from Moderate Resolution Imaging Spectroradiometer (MODIS): Evaluation of global patterns and comparison with in-situ measurements. *Journal of Geophysical Research: Biogeosciences*, *111*(4), 1–14. https://doi.org/10.1029/2006JG000217

Zhang, X., Friedl, M. A., Schaaf, C. B., Strahler, A. H., & Liu, Z. (2005). Monitoring the response of vegetation phenology to precipitation in Africa by coupling MODIS and TRMM instruments. *Journal of Geophysical Research D: Atmospheres*, *110*(12), 1–14. https://doi.org/10.1029/2004JD005263

Zhang, X., Wang, J., Gao, F., Liu, Y., Schaaf, C., Friedl, M., Henebry, G. M. (2017). Exploration of scaling effects on coarse resolution land surface phenology. *Remote Sensing of Environment*, *190*, 318–330. https://doi.org/10.1016/j.rse.2017.01.001

Zhao, J., Wang, Y., Zhang, H., Zhang, Z., Guo, X., Yu, S., & Du, W. (2016). Spatially and temporally continuous LAI datasets based on the mixed pixel decomposition method. *SpringerPlus*, *5*(1), 1-13. https://doi.org/10.1186/s40064-016-2166-9

Zhou, R., Wang, H., Duan, K., & Liu, B. (2021). Diverse responses of vegetation to hydroclimate across temporal scales in a humid subtropical region. *Journal of Hydrology: Regional Studies, 33*, 100775. https://doi.org/10.1016/j.ejrh.2021.100775.

Zhu, Y., Liu, S., Yi, Y., Xie, F., Grünwald, R., Miao, W., ... & Singh, D. (2021). Overview of terrestrial water storage changes over the Indus River Basin based on GRACE/GRACE-FO solutions. *Science of The Total Environment*, *799*, 149366. https://doi.org/10.1016/j.scitotenv.2021.149366

Zoungrana, B. J., Conrad, C., Amekudzi, L. K., Thiel, M., & Da, E. D. (2015). Land Use/Cover Response to Rainfall Variability: A Comparing Analysis between NDVI and EVI in the Southwest of Burkina Faso*. Climate, 3(1),* 63–77. https://doi.org/10.3390/cli3010063

Appendix A

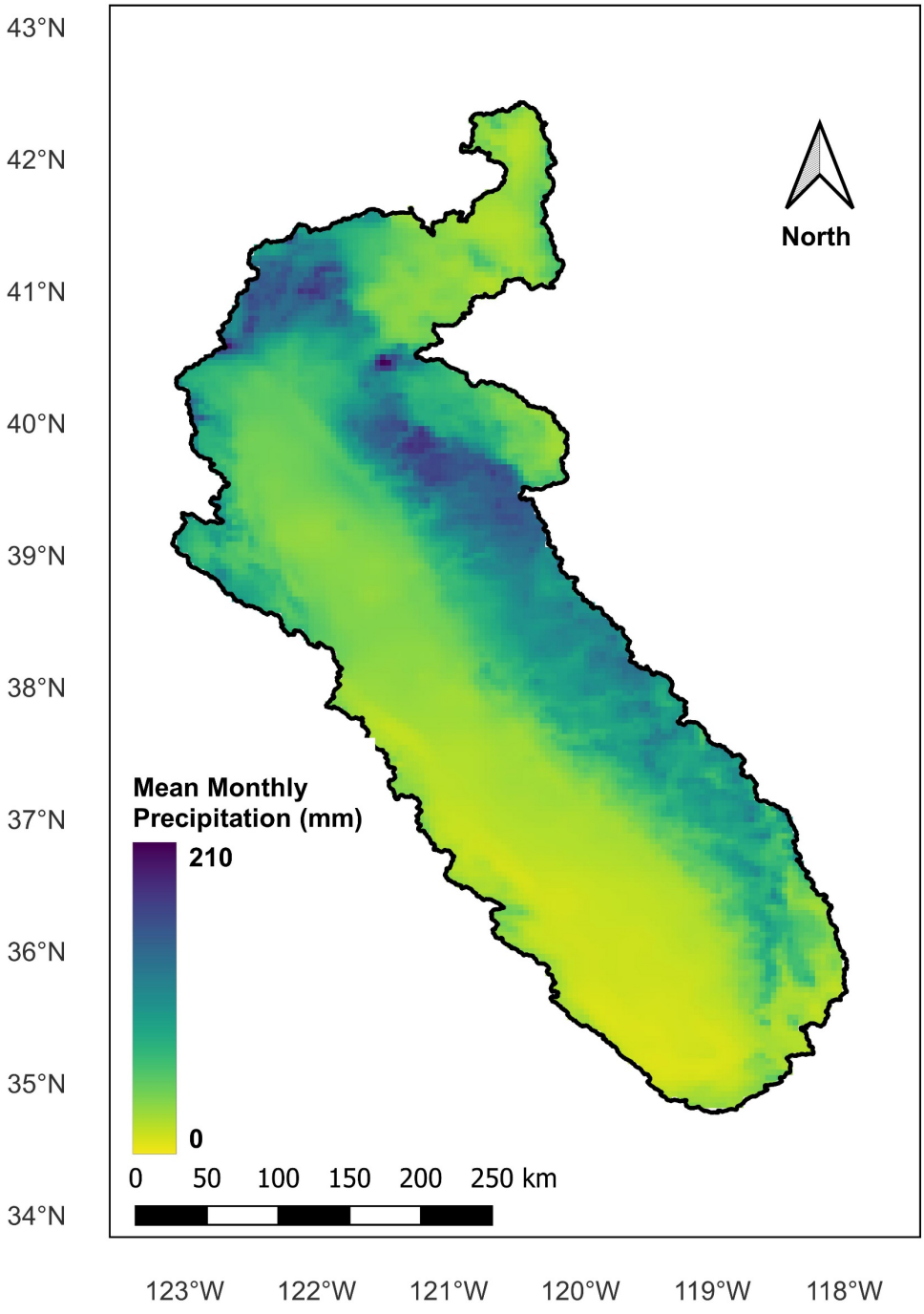

Figure A1. Mean monthly precipitation (2004-2010) of Sacramento and San Joaquin river basins

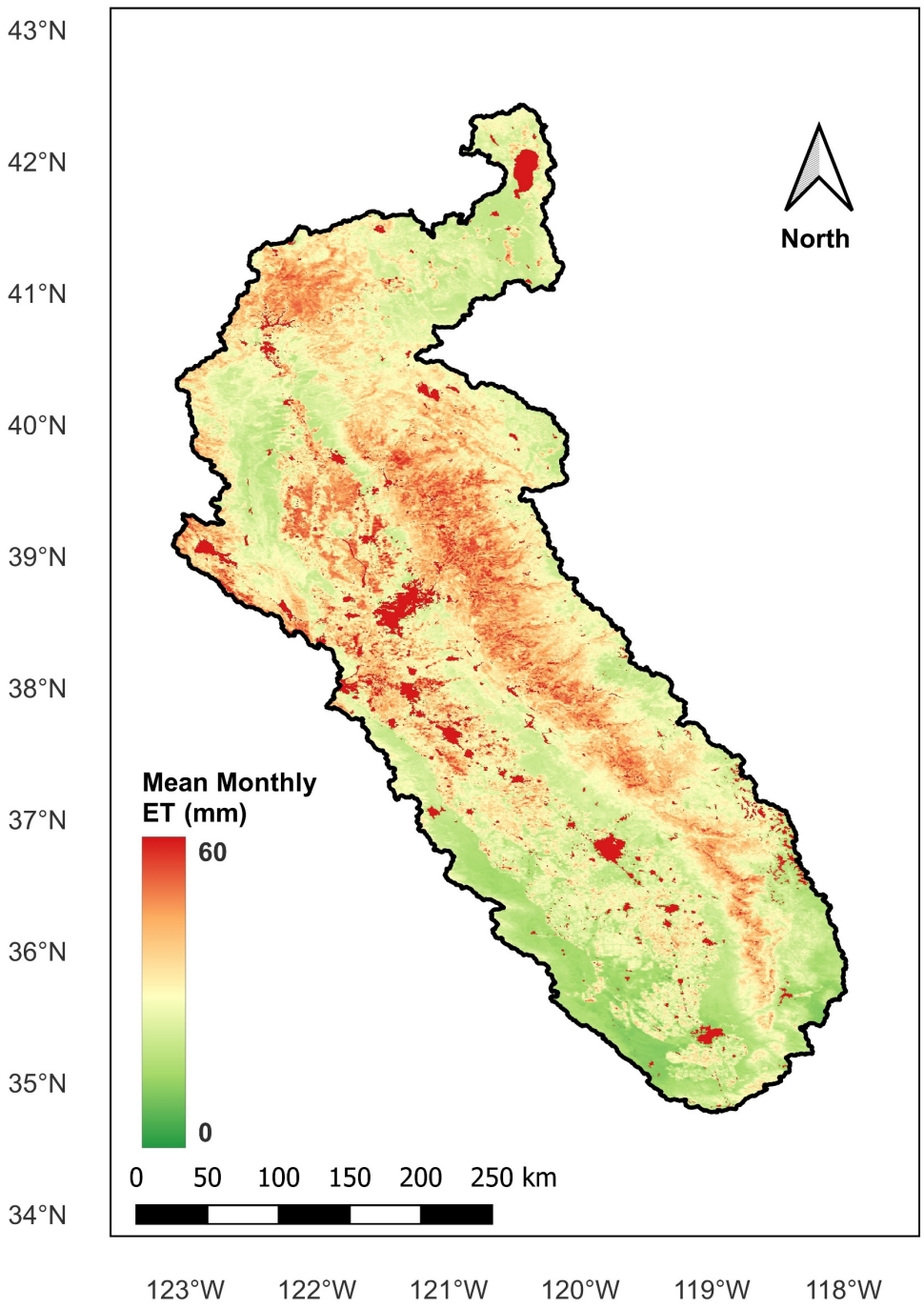

Figure A2. Mean monthly evapotranspiration (2004-2010) of Sacramento and San Joaquin river basins

Appendix B

Introduction

This appendix information contains figures to supplement the findings of the chapter 4. Figure B1 illustrates the seasonal and interannual variation of mean temperature and vapor pressure deficit. Figure B2 illustrates the interannual variations of normalized difference vegetation index (NDVI) and leaf area index (LAI) anomalies for crops, evergreen forests, grasslands, and shrublands.

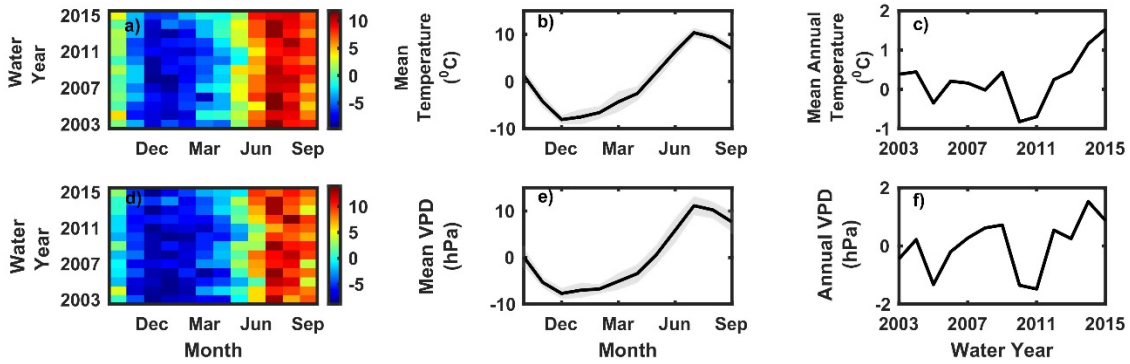

Figure B1. a) Rasterized time series of mean temperature anomalies; b) seasonality of mean temperature anomalies (in all plots, shaded region shows +/- one standard deviation); c) annual mean temperature anomalies; d) rasterized time series of vapor pressure deficit anomalies; e) seasonality of vapor pressure deficit anomalies; f) annual vapor pressure deficit anomalies.

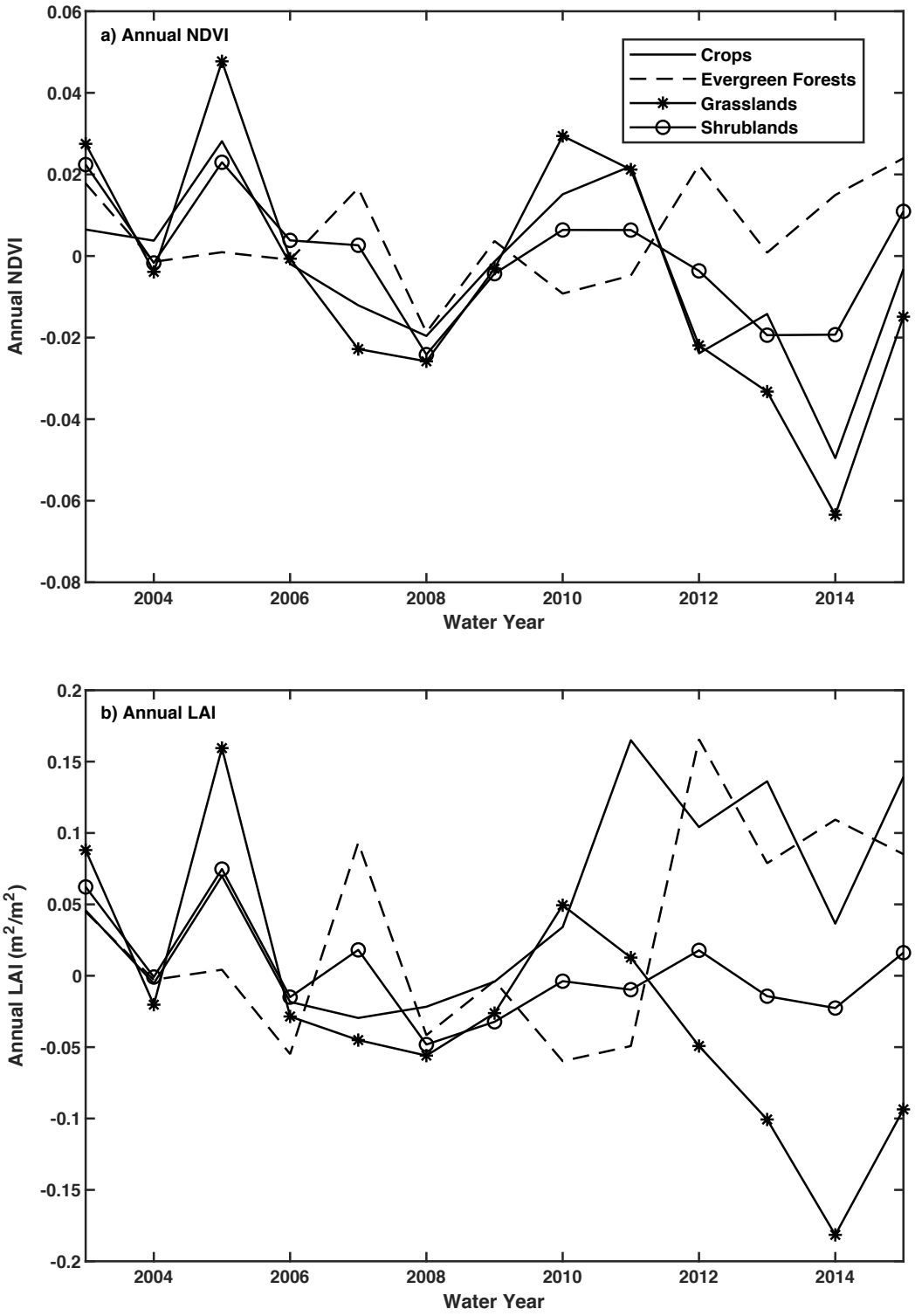

Figure B2. Interannual variations of a) NDVI anomalies and b) LAI anomalies for different plant function types.